# GPR METHODS FOR THE DETECTION AND CHARACTERIZATION OF FRACTURES AND KARST FEATURES: POLARIMETRY, ATTRIBUTE EXTRACTION, INVERSE MODELING AND DATA MINING TECHNIQUES

A Dissertation

by

DOUGLAS SPENCER SASSEN

Submitted to the Office of Graduate Studies of
Texas A&M University
in partial fulfillment of the requirements for the degree of

DOCTOR OF PHILOSOPHY

December 2009

Major Subject: Geophysics

# GPR METHODS FOR THE DETECTION AND CHARACTERIZATION OF FRACTURES AND KARST FEATURES: POLARIMETRY, ATTRIBUTE EXTRACTION, INVERSE MODELING AND DATA MINING TECHNIQUES

A Dissertation

by

DOUGLAS SPENCER SASSEN

Submitted to the Office of Graduate Studies of
Texas A&M University
in partial fulfillment of the requirements for the degree of

DOCTOR OF PHILOSOPHY

Approved by:

| | |
|---|---|
| Chair of Committee, | Mark E. Everett |
| Committee Members, | Christopher C Mathewson |
| | Jean-Louis Briaud |
| | Hongbin Zhan |
| | Luc Ikelle |
| Head of Department, | Andreas Kronenberg |

December 2009

Major Subject: Geophysics

# ABSTRACT

GPR Methods for the Detection and Characterization of Fractures and Karst Features: Polarimetry, Attribute Extraction, Inverse Modeling and Data Mining Techniques.
Douglas Spencer Sassen, B.S., University of Texas; M.S., Texas A&M University
Chair of Advisory Committee: Dr. Mark E. Everett

The presence of fractures, joints and karst features within rock strongly influence the hydraulic and mechanical behavior of a rock mass, and there is a strong desire to characterize these features in a noninvasive manner, such as by using ground penetrating radar (GPR). These features can alter the incident waveform and polarization of the GPR signal depending on the aperture, fill and orientation of the features. The GPR methods developed here focus on changes in waveform, polarization or texture that can improve the detection and discrimination of these features within rock bodies. These new methods are utilized to better understand the interaction of an invasive shrub, *Juniperus ashei*, with subsurface flow conduits at an ecohydrologic experimentation plot situated on the limestone of the Edwards Aquifer, central Texas.

First, a coherency algorithm is developed for polarimetric GPR that uses the largest eigenvalue of a scattering matrix in the calculation of coherence. This coherency is sensitive to waveshape and unbiased by the polarization of the GPR antennas, and it shows improvement over scalar coherency in detection of possible conduits in the plot data. Second, a method is described for full-waveform inversion of transmission data to quantitatively determine fracture aperture and electromagnetic properties of the fill, based on a thin-layer model. This inversion method is validated on synthetic data, and the results from field data at the experimentation plot show consistency with the reflection data. Finally, growing hierarchical self-organizing maps (GHSOM) are applied to the GPR data to discover new patterns indicative of subsurface features,

without representative examples. The GHSOMs are able to distinguish patterns indicating soil filled cavities within the limestone.

Using these methods, locations of soil filled cavities and the dominant flow conduits were indentified. This information helps to reconcile previous hydrologic experiments conducted at the site. Additionally, the GPR and hydrologic experiments suggests that *Juniperus ashei* significantly impacts infiltration by redirecting flow towards its roots occupying conduits and soil bodies within the rock. This research demonstrates that GPR provides a noninvasive tool that can improve future subsurface experimentation.

# DEDICATION

To Sharon and Thomas

# ACKNOWLEDGEMENTS

I would like to thank Clyde Munster, Phillip Taucer, Brad Wilcox and Binayak Mohanty for inviting me to participate in this research opportunity. Without the enthusiasm and dedication to this project from Dax Soule and Josh Gowan the data acquisition would not have been possible. The Texas Water Research Institute Mill's scholarship program provided funding for travel to the Honey Creek Natural Area.

Additionally, I would like to thank my advisor, Mark Everett, committee members, Christopher Mathewson, Hongbin Zhan, Luc Ikelle, and Jean-Louis Briaud, and the journal reviewers from SEG and EAGE for the constructive critique of the dissertation. Mark Everett in particular has put in considerable effort to edit this work.

# NOMENCLATURE

| | |
|---|---|
| DM/KDD | Data Mining and Knowledge Discovery Database |
| EM | Electromagnetic |
| GHSOM | Growing Hierarchical Self-Organizing Map |
| GPR | Ground-penetrating Radar |
| TE | Transverse Electric |
| TM | Transverse Magnetic |
| pdf | Probability Density Function |

TABLE OF CONTENTS

CHAPTER Page

# LIST OF FIGURES

FIGURE Page

FIGURE Page

FIGURE Page

FIGURE Page

# LIST OF TABLES

# CHAPTER I

# INTRODUCTION TO THE PROBLEM

## INTRODUCTION

The detection of fractures and karst features and identification of their size and fill materials are important areas of near-surface geophysical research, with potential applications in hydrology and rock mass studies for civil and mining engineering. The presence of fractures and voids within rock can alter the hydraulic and mechanical properties of the rock mass significantly, and these bulk properties often differ considerably from laboratory measurements on rock samples. In the relatively new multidisciplinary field of ecohydrology the problems of understanding subsurface process as they interact with ecological communities are especially complex for fractured rock or karst landscapes. The lack of adequate subsurface characterization has led to an underestimation of the influence of subsurface processes on ecosystems (Huxman et al., 2005). There is a need for non-destructive methods, such as ground-penetrating radar (GPR) to investigate shallow (<10 m) subsurface ecological interactions in these challenging environments.

The acquisition and processing of scalar GPR reflection data has been successfully applied by previous workers to the characterization of fractured rock and karst environments. Early GPR studies of fractured rock utilized 2-D scalar data (e.g. Stevens et al., 1995). More recently, Van Gestel and Stoffa (2001) and Seol *et al.* (2001) demonstrated with Alford rotations the use of 2-D multicomponent GPR to determine the strike direction of fractures. Tsoflias et al. (2004) demonstrated the use of

---

This dissertation follows the style of Geophysics.

the polarization properties of GPR to detect vertical fractures. Tsoflias and Hoch (2006) investigated multi-polarization GPR for the characterization of thin vertical fracture properties. Grasmueck et al. (2005) showed the benefits of single-component GPR acquired in 3-D with high spatial sampling for imaging fractures. A 4-D GPR survey, i.e. repeated 3-D surveys in time, was used to track saline tracer flow in a sub-horizontal fracture (Talley et al., 2005). Jeannin et al. (2006) used the face of a vertical cliff to acquire vertical and horizontal reflection profiles and horizontal transmission profiles to delineate fractures for a rock-mass stability study. Also the efficacy of GPR for the detection of karst features has been demonstrated numerous times (e.g. Kruse et al., 2006; Tallini et al., 2006) There is still significant scope for development of methods that enhance the detection of fractures by utilizing the vectorial nature of GPR waves and allow for quantitative descriptions of the fracture aperture and fill materials through geophysical inversion and data mining techniques.

The received EM signal depends strongly on the polarization of the transmitting and receiving antennas, and on the geometry and electromagnetic properties of any target scatterer. Traditional GPR systems utilize bistatic dipole or bowtie antennas that produce nearly linearly polarized EM waves. Subsurface diffracting bodies generally change the polarization of these incident waves. It has been demonstrated, for example, that a low impedance cylinder, such as a clay-filled karst pipe, is best imaged with the long axis of the antennas oriented parallel to the cylinder, while a high impedance cylinder, such as an air-filled karst pipe, is best imaged with antennas oriented perpendicular to the axis of the cylinder (Radzevicius and Daniels, 2000). Traditional GPR surveys however utilize a single antenna polarization and, as the orientation and properties of subsurface targets are generally unknown, there is a great potential for interpretation bias. An example of the relationship between antenna orientation and the GPR response of a diffracting body is illustrated in Figure 1.1.

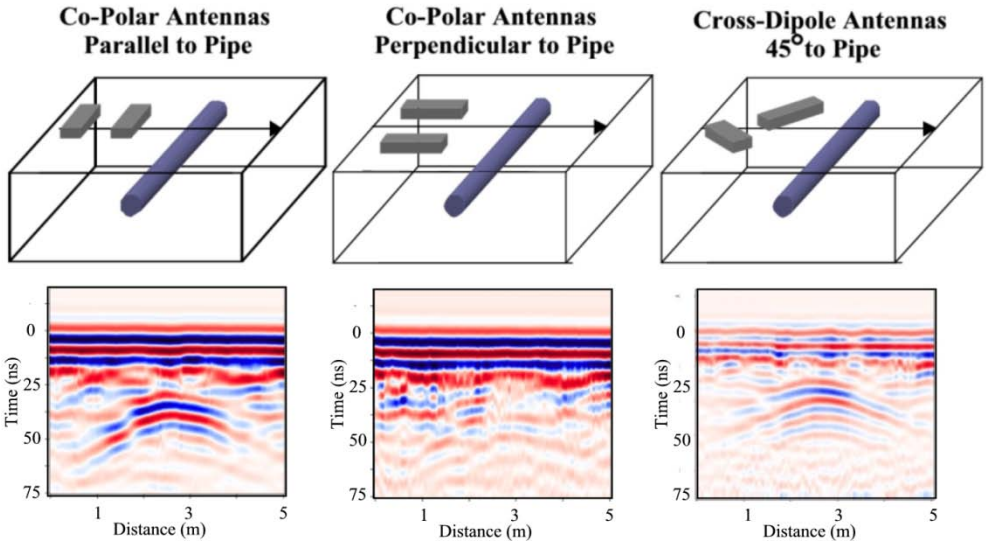


Figure 1.1. A GPR survey showing the effect of the antenna orientation relative to that of a buried pipe. The PVC pipe is partially filled with water, and buried ~1.5 m in a natural, moist silty-sand soil. Arrows in upper panel indicate the direction of transect (After Sassen, 2008).

To take advantage of the vector nature of EM waves and to minimize imaging bias, polarimetric GPR data utilizing multiple EM components should be acquired. Previous research that focused on extracting polarization dependent information include the works Van Gestel and Stoffa (2001) and Seol et al. (2001), who used Alford rotations (Alford, 1986) for GPR to determine the strike of elongate targets such as cylinders and fractures. Also, Tsoflias et al. (2004) used the polarization properties of GPR waves to detect vertical fractures in limestone. Recently, Streich and van der Kruk (2007) have developed a GPR imaging technique based on an analytic solution of the total field for a dipole over a half space that minimizes the effects of the antenna radiation pattern on GPR data. This imaging method provides the means to extract polarization dependent information by removing the bias caused by variations in antenna patterns for the different antenna configurations. These methods provide important detection and discrimination insights that are not available with traditional single component GPR techniques.

Other authors have utilized the distortion of the transmitted electromagnetic wavelet caused by subsurface scattering to provide detection and discrimination capability. The GPR wavelet is distorted due to the constructive and destructive interference resulting from multiple internal reflections within a fracture, karst feature or thin layer (Figure 1.2), as well as pulse distortions caused by wave propagation in dispersive earth materials.

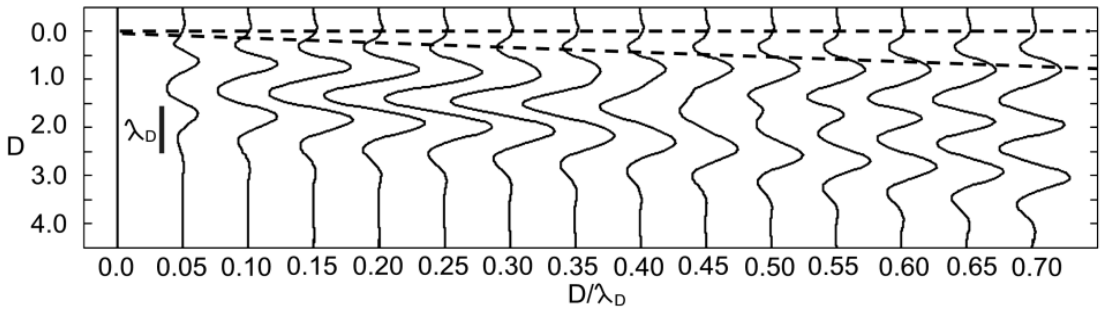


Figure 1.2. Response of an EM wavelet to a thin-layer-wedge. Change in GPR waveform from reflections off of a thin-layer as a function of the ratio of the thin-layer thickness to the dominant wavelength of the wavelet in the thin-layer (after Widess, 1973, and Sassen and Everett, 2009a). The dashed lines show the nondimensionalized thickness (D) of the thin-layer. The background media is $\varepsilon_r$ = 12, $\mu_r$ = 1, and $\sigma$ = 0, the thin layer is $\varepsilon_r$ =20, $\mu_r$ = 1, and $\sigma$ = 0.01 S/m, and the angle of incidence is 15˚.

Kofman et al., (2006) has interpreted reverberation phenomena, resulting from constructive interference, to identify air-filled cavities similar to karst pipes. Gregoire and Hollender (2004) utilized the changes in the amplitude spectrum of GPR reflection data, caused by constructive and destructive interference, as the basis for an inversion to determine the aperture and electromagnetic properties of the fill of a thin layer. Bradford and Deeds (2006) proposed amplitude-variation-with-offset (AVO) to determine the dielectric properties of thin beds. Deparis and Garambois (2007) inverted both amplitude and phase variation-with offset (APVO) data acquired from a cliff face to determine fracture properties. Lambot et al. (2004) utilized a thin-layer recursion

formula to estimate 1-D soil geoelectrical properties from stepped frequency GPR data. McClymont et al. (2008) demonstrated the efficacy of coherency attributes, which respond to changes in wavelet shape, as an aid in the interpretation of GPR data from a fault zone. These authors have demonstrated the potential advantages of GPR techniques and that utilize changes in wavelet shape and amplitude spectra to improve upon detection and characterization of subsurface features.

While the response of GPR signals to a cylinder or thin-layer are well understood, only a few subsurface features have the idealized geometry or material properties that allow for deterministic estimation of properties using analytic inversion models. Also, a single measure of polarization or waveform is often insufficient to constrain a target's properties from noisy data. Complicating the issue further is the lack of direct access to subsurface features for calibration of empirical models or supervised pattern recognition techniques. Unsupervised learning techniques fill the niche where deterministic methods are inadequate and prior information on the subsurface is insufficient for empirical modeling. Unsupervised learning techniques group features exhibiting similar attributes together into clusters while distancing features exhibiting very different attributes. This is markedly different from typical pattern recognition or classification methods, in which the objective is to find common attributes of previously labeled features and the groupings, or classes, are defined by the label itself.

One of the most popular unsupervised learning techniques in geophysics is the self-organizing map (SOM) (Kohonen, 1990). SOMs have the advantage of expressing data of high dimensionality onto a low dimension map, where nodes representing similar data are topographically close and the map reflect the probability density function of the data (Kohonen, 1990). In the comparison of several unsupervised learning techniques for seismic facies analysis, Marriquin *et al*. (2009) preferred SOMs for identifying data clusters. Castro de Matos et al. (2007) used SOMs in their process of seismic facies analysis. Klose, 2006, used SOMs to analyze patterns from 6 seismic properties to interpret tomographic seismic data. Bauer et al. (2008) used the SOM to find clusters from the attributes of P-wave velocity, attenuation and anisotropy in tomographic data.

Benavides et al. (2009) used SOMs to identify clusters separating UXOs from fragments in time-domain EM data. Essenreiter et al. (2001) used the SOM to find patterns useful for identifying reflection multiples in seismic data. These authors have shown the effectiveness of SOM to geophysical problem. More recent SOM adaptations of the traditional SOM's treat several shortcomings by combining automatic map growth with hierarchal growth (Herrero, et al., 2001, and Dittenbach at al., 2002). This development has provided a tool with the advantages and computational efficiency of the SOM with the intuitive organization of hierarchical clustering methods.

I build on the advantages of polarimetric GPR techniques and utilize changes in wavelet shape and amplitude spectra to improve upon detection and characterization of subsurface fractures and karst features. I introduce a new coherency algorithm that enhances the detection of subsurface discontinuities from GPR data by utilizing changes in waveshape. Plus, I introduce a full-waveform nonlinear inversion technique that is used to estimate fracture aperture and electromagnetic fill properties from GPR transmission profiles. In addition, I explore the use of the recent growing hierarchical SOM to cluster multiple measures of waveform, polarimetry and texture to identify patterns that can distinguish subsurface features. These methods are applied to study the ecohydrology of an experimentation plot situated within the Edwards Aquifer region of central Texas

## BACKGROUND OF THE ECOHYDROLOGY OF THE EDWARDS AQUIFER REGION

In the semiarid region of the southwest United States, human settlement over the past 150 years has altered the natural environment of grassland and savannah into shrubland through the suppression of natural fires and intense grazing (Van Auken, 2000). The consequent proliferation of *Juniperus ashei*, a deep rooted evergreen shrub, within the central Texas rangeland is hypothesized to reduce recharge into local streams and the Edwards aquifer (Wilcox, 2002; Olenick et al., 2004). Careful management of

the Edwards Aquifer of central Texas, USA, is important since it is the primary source of water for 1.7 million people including the residents of San Antonio (EAA, 2006). The water of the karst Edwards aquifer is under intense demand, with aquifer discharge exceeding annual recharge rates during the 1990's (Dugas et al., 1998). The demand will become even greater with continued population growth. There is a great deal of interest in restoring the natural ecology through brush control with hopes that it will increase rangeland productivity, and increase stream flow and aquifer recharge (Olenick, et al. 2004). The state government of Texas subsidizes brush removal from the contributing areas that provide recharge to the Edwards Aquifer in hopes of enhancing recharge volumes.

However, some empirical studies on brush invasion and control seem to indicate that brush removal is not an effective means of enhancing groundwater volumes in the Edwards aquifer region. One previous field study (Dugas et al., 1998) on the change in evapotranspiration and surface runoff following shrub removal within the Edwards Aquifer recharge zone indicates only temporary (3 years) gains in water yields. Wilcox *et al*. (2008) showed that in a similar karst environment brush encroachment actually increases groundwater yields. It was suggested that brush enhances infiltration and allows a larger portion of water to bypass evapotranspiration. Additionally, *Juniperus ashei* roots may enhance subsurface flow through the enlargement of joints within shallow limestone and by providing preferential pathways (Dasgupta et al., 2006). The effect of *Juniperus ashei* on subsurface flow through fractures and karst features remains uncertain.

The subsurface hydrology in fractured rock and karst environments is typically characterized by the occurrence of discrete flow conduits (Bear *et al*., 1993). The 3-D geometry of fractures and karst features, along with the type and distribution of the fill material, substantially impacts plant and animal access to water and soil nutrients. Isolated cores, sampled at a few discrete points, are largely inadequate for a complete ecohydrologic characterization. Consequently, geophysical techniques such as ground penetrating radar (GPR), which provide spatially continuous subsurface information, can

enhance fractured rock description.

The recharge zone for the Edwards aquifer is a ~0.4 Mha region of central Texas (Olenick el al., 2004). The recharge zone is delineated by surface exposures of the Cretaceous Edwards formation lying within the Balcones Fault Zone (Figure 1.3). The contributing zone is defined as the surrounding areas that feed surface water and groundwater into the recharge zone.

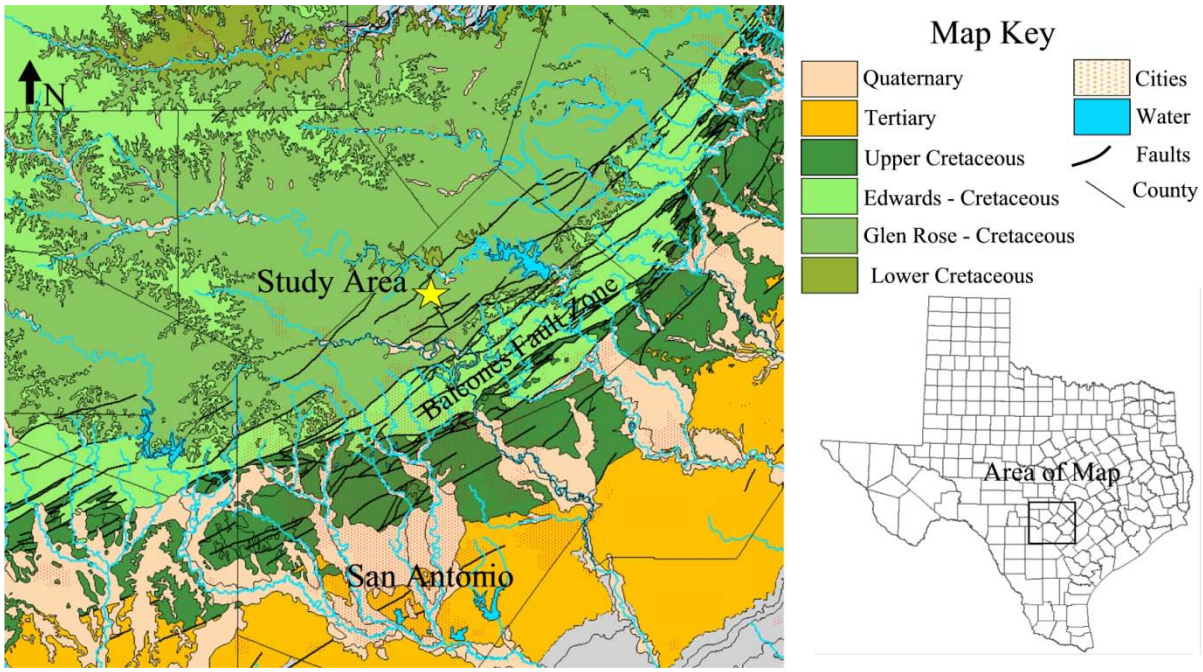


Figure 1.3. Geologic map of the Edwards Aquifer region and the research site. The Edwards Aquifer recharge zones are the areas of surface exposure of the Edwards formation. The contributing zones are demarked by the Glen Rose formation.

The main geologic unit of the Edwards Aquifer contributing zone is the Cretaceous-aged Glen Rose formation. The Glen Rose formation alternates between regionally continuous layers of marl and limestone reflecting cycles of rising and falling sea level throughout the Cretaceous (Mancini and Scott, 2006). The limestone strata

contain vertical conduits that enhance lateral subsurface flow while the relatively impermeable layers of marl act to baffle vertical flow (Figure 1.4).

Figure 1.4. Picture of a section of the Glen Rose formation at the Canyon Lake spillway, Canyon Lake, TX. The Glen Rose has series of continuous layers of clay rich marl (gray) and limestone (tan). Some karst features (small caves) can be seen on the interface between the limestone and marl.

The faulting and jointing of the limestone allows acidic groundwater to flow through the relatively low permeability rock matrix, dissolving carbonate minerals and forming the karst features (Ferrill et al., 2004). Structurally, the study site is associated with the Balcones fault zone whose strike of main faulting is ~NE-SW (Collins, 1995). The more pervasive smaller-scale faults and joints (Figure 1.5) generally trend both parallel and at an acute angle to the main strike of faulting, with increasing density and

interconnectivity in the vicinity of the larger faults (Collins, 1987; 1995). However, under similar mechanical conditions, the pattern of joint density, orientation and aperture varies from one rock unit to the next depending on the bulk mineralogy and porosity of the unit (Collins 1995). Thus, there is significant uncertainty as to the orientation of fractures and faulting within the study site.

Figure 1.5. Shown here are joints widened by carbonate dissolution within the Glen Rose formation, Canyon Lake spillway, Canyon Lake, TX. The fracture, joint and fault patterns within a single rock unit typically trend parallel to each other.

## THE EXPERIMENTATION SITE

To study the effects of brush removal on the hydrologic cycle of the Edwards aquifer region, a hydrologic experimentation site was established (Taucer et al. 2006;

Dasgupta et al., 2006) within the contributing zone, approximately 45 km north of San Antonio (Figure 1.3). The study area consists of a small, rectangular experiment plot (14 m x 7 m) within a stand of *Juniperus ashei* (Figure 1.6). The site instrumentation includes a rainfall simulator, a runoff gauge, rain gauges, soil moisture probes and a 2.5 m deep trench excavated on the downslope (2% topographic gradient) boundary of the site. The purpose of the trench, which exposes the shallow limestone and marl stratigraphy, is to quantify and sample lateral subsurface flow. Rainfall simulations were conducted on this site both before and after clearing of the *Juniperus ashei* to evaluate the hydrologic effects of brush removal.

(*a*) (*b*)

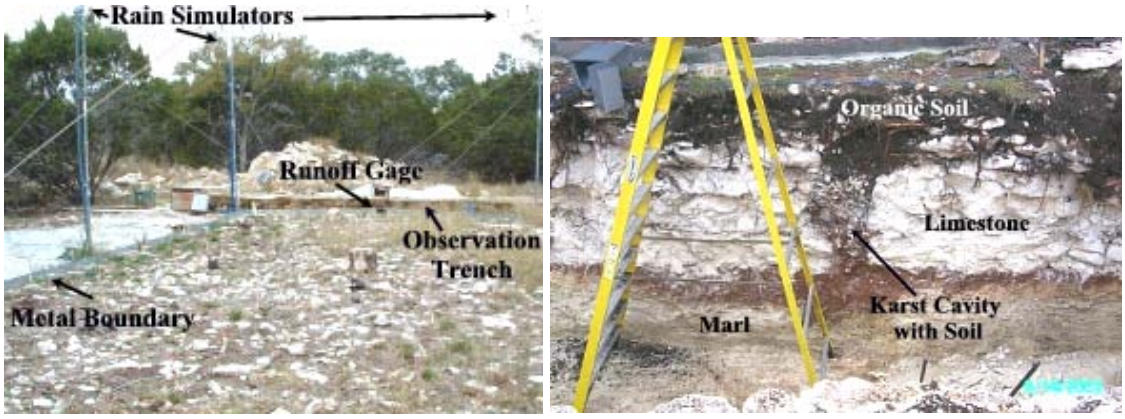


Figure 1.6. The research site showing: (*a*) the rainfall simulator and surface runoff gauge; (*b*) the downslope trench for quantifying and sampling lateral subsurface flow.

The exposed lithology in the observation trench indicates that the top 0.3 m consists of weathered limestone and organic soil; below that is 1.5 m of limestone containing joints and karst features; these layers are underlain by a low permeability layer of marl (Figure 1.6*b*). Soil and roots partially fill many of the exposed joints and karst features along the trench face.

## PREVIOUS HYDROLOGIC RESULTS

Hydrological experiments on the study plot were run both before and after clearing the brush. During simulated rainfall most of the lateral subsurface flow is observed to exit at the trench face in discrete locations corresponding to the joints and karst features that contain roots (Dasgupta et al., 2006). In the pre-cut condition, a greater volume of the water applied by the rainfall simulator reached the trench face compared to identical simulations performed under the post-cut condition. Taucer et al. (2006) showed that during intense rainfall simulations (0.152 m/hr), nearly all water that reached the surface of the plot infiltrated into high-capacity subsurface conduits. There was negligible surface runoff, yet only 57% of the applied water escaped from the downslope trench face. Most of that amount emerged from a very limited number of discrete joints, conduits, or bedding planes. A significant amount (16%) of the water intercepted by the *Juniperus ashei* brush was channeled by stemflow into the subsurface at the base of the brush. Although no runoff was collected on the downslope portion of the plot, ponding was observed in all rainfall simulations. Even after intense rainfall events the organic litter was observed to be dry just a few centimeters below the surface. The *Juniperus ashei* litter exhibits a high degree of hydrophobicity, or water repellency. The preponderance of stemflow and the hydrophobicity of the litter suggests that the *Juniperus ashei* may channel flow directly to its roots, promoting preferential flow to the subsurface. This raises questions about how the roots of the *Juniperus ashei* might affect the subsurface preferential flow pathways provided by fractures.

To better understand the preferential subsurface conduit system, a series of tracer tests was conducted by Taucer et al. (2006). Three non-reactive tracers were applied to the surface at different locations within the plot to allow for simultaneous monitoring during a rainfall simulation experiment. Uranine was applied to the distal upslope portion of the site; eosine was applied in the middle of the plot around the largest tree trunk; and phloxine was applied in close proximity to the trench (Figure 1.7). Water samples from the trench face were collected for tracer analysis at 16 discrete locations

that had been observed as key groundwater egress points during previous rainfall simulations (Figure 1.8).

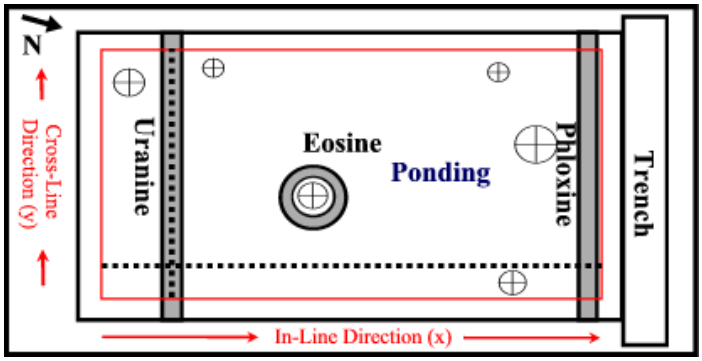


Figure 1.7. Map view of the experimental plot. The red box represents the extent of the 3-D GPR survey (12.7 x 6.3 m), which is surrounded by metal sheeting to capture runoff. The gray areas show the locations of the three surface-applied dyes. The dotted lines indicate the location of the in-line and cross-line GPR sections discussed in Chapter II. The crosshairs indicate the location and relative size of *Juniperus ashei* trunks on the site. The figure is adapted from Taucer *et al*. (2006).

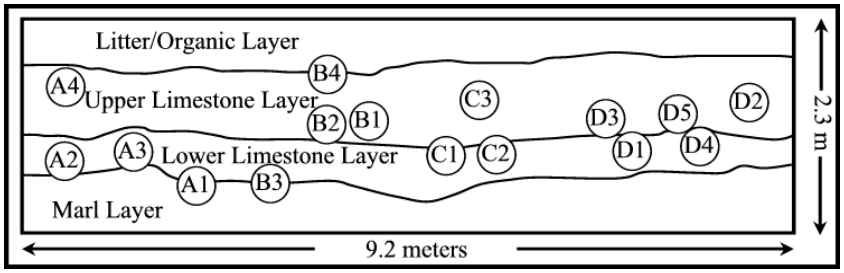


Figure 1.8. The tracer sampling locations and lithology in the vertical trench face. The figure is adapted from Taucer *et al*. (2006).

None of the distal uranine applied to the upslope portion of the plot was observed to exit at the trench face. In contrast, the A and B sampling regions (Figure 1.8) showed that the proximal phloxine and the middle eosine tracers exhibited similar breakthrough patterns. In some locations (A1 and A3) the peak concentration of the mid-range eosine

preceded the peak concentration of proximal phloxine, even though the mid-range eosine had traveled further. Within the C and D sampling regions only the proximal phloxine showed strong concentrations; the mid-range eosine was detected only at specific locations C1 and D4 and moreover in significantly lower concentration.

## OBJECTIVES

In this dissertation I have addressed the question of how does one detect and characterize fractures, joints and karst features within the shallow subsurface in a minimally invasive manner. I answer this question by exploring existing methodologies and by developing new methodologies for analyzing and acquiring ground-penetrating radar (GPR) data. I have also explored the significance of the results on the interactions between the ecology and hydrology, or ecohydrology, of the Honey Creek Nature Area of central Texas, USA.

## DISSERTATION STRUCTURE

**Chapter I** provides background information on the importance of fracture and karst feature detection and discrimination, the current state of the art in GPR methodologies for detecting and characterizing these features, and a summary of the setting and previous work conducted at the Honey Creek Nature Area experimentation plot. Much of the material in this chapter is repeated in subsequent chapter, because they were originally intended as standalone journal articles.

**Chapter II** is a republication of, “3D Polarimetric GPR coherency attributes and full-waveform inversion of transmission data for characterization of fractured rock” (Sassen and Everett, 2009). In this chapter I introduce a new coherency attribute algorithm for use with polarimetric GPR data. This algorithm enhances the detection of subsurface discontinuities. I also demonstrate its improvement over existing methods

with data from the Honey Creek site. Plus, I introduce a full-waveform nonlinear inversion technique that is used to estimate fracture aperture and electromagnetic fill properties from GPR transmission profiles. This method is validated on finite difference time-domain synthetic data, and applied to the Honey Creek site.

**Chapter III** is an analysis of the ecohydrologic significance of multicomponent GPR data and the coherency and inversion results at the site. The GPR results suggest that *Juniperus ashei*, an invasive shrub, has significantly altered the surface and subsurface hydrology and carbon storage within the central Texas region. This chapter will appear in the October, 2009 issue of Near Surface Geophysics, a special issue on hydrogeophysics as a paper entitled, "Ecohydrogeophysics at the Edwards Aquifer: Insights from Polarimetric Ground Penetrating Radar".

**Chapter IV** is the application of the data mining and knowledge discovery (DM/KDD) process to the GPR data from the Honey Creek Natural Area. I focused on the recently developed unsupervised learning technique, growing hierarchical self-organizing maps (GHSOM), and an adaption of an automatic labeling technique for enhancing interpretation of geophysical data. The GHSOM used in the DM/KDD process revealed distinctive patterns indicative of soil filled cavities and joints within the limestone under the experimentation plot. A version of this chapter will also be published in a peer-reviewed journal.

**Chapter V** is the discussion and conclusion for the dissertation as a whole. It highlights the contributions and caveats of this research.

**Appendix** covers an algorithm for the alternating direction implicit finite-difference time-domain (ADI-FDTD) modeling technique for simulating electromagnetic propagation in 3D, specifically for fast modeling of GPR. The section covers the discritization of Maxwell's equations, boundary conditions, and models of a GPR source for the ADI-FDTD method. This section also includes validation of the algorithm against analytic solutions and simulation examples.

# CHAPTER II

# 3D POLARIMETRIC GPR COHERENCY ATTRIBUTES AND FULL-WAVEFORM INVERSION OF TRANSMISSION DATA FOR CHARACTERIZATION OF FRACTURED ROCK*

## SUMMARY

Ground penetrating radar (GPR) can be utilized to detect and describe fractures for characterization of fractured rock formations. A fracture alters the incident waveform, or waveshape, of the GPR signal through constructive and destructive interference, depending on the aperture, fill and orientation of the fracture. As the electromagnetic waves of GPR are vectorial in nature, features exhibiting strong directionality can change the state of polarization of the incident field. GPR methods that focus on changes in waveform or polarization can improve the detection and discrimination of fractures within rock bodies. Coherency is a traditionally seismic attribute used for the delineation of discontinuities in wavelet shape. A coherency algorithm is developed for polarimetric GPR that uses the largest eigenvalue of the time-domain scattering matrix in the calculation of coherence. This coherency algorithm is sensitive to waveshape and unbiased by the polarization of the GPR antennas. The polarimetric coherency algorithm shows improvement over scalar coherency in removing the effects of polarization on field data collected from a fractured limestone plot used for hydrologic experimentation. Also, a method is described for time-domain full-waveform inversion of transmission data to quantitatively determine the fracture

---

*Reprinted with permission from: 3D Polarimetric GPR Coherency Attributes and full-waveform inversion of transmission data for characterization of fractured rock, Sassen and Everett, 2009, Geophysics, 74, no. 3, J23-J34, 2009, by The Society of Exploration Geophysics.

aperture and electromagnetic properties of the fill, based on a thin-layer model. Inversion results from field data at the experimentation plot show consistency with the location of fractures from the reflection data. Together, these methods provide improved fracture detection capability and quantitative information on fracture aperture, and the dielectric permittivity and electrical conductivity of the fill over traditional GPR imaging and scalar coherency attributes.

## INTRODUCTION

The detection of fractures and identification of their aperture and fill materials is an important area of near-surface geophysical research, with potential applications in fractured rock hydrology and rock mass studies for civil and mining engineering. The presence of fractures in rock can alter the hydraulic and mechanical properties of the rock mass significantly, and these bulk properties often differ considerably from laboratory measurements on rock samples. Consequently, geophysical techniques such as ground penetrating radar (GPR), which provide spatially continuous subsurface information, can enhance fractured rock description. GPR increasingly is being used for near-surface characterization of fractured rocks because of its high resolution imaging capabilities and good penetration (~10 m) in most rock materials. Early GPR studies of fractured rock utilized 2-D scalar data (e.g. Stevens et al., 1995). More recently, Van Gestel and Stoffa (2001) and Seol *et al.* (2001) demonstrated with Alford rotations the use of 2-D multicomponent GPR to determine the strike direction of fractures. Tsoflias et al. (2004) demonstrated the use of the polarization properties of GPR to detect vertical fractures. Tsoflias and Hoch (2006) investigated multi-polarization GPR for the characterization of thin vertical fracture properties. Grasmueck et al. (2005) showed the benefits of single-component GPR acquired in 3-D with high spatial sampling for imaging fractures. A 4-D GPR survey, i.e. repeated 3-D surveys in time, was used to track saline tracer flow in a sub-horizontal fracture (Talley et al., 2005). Jeannin et al. (2006) used the face of a vertical cliff to acquire vertical and horizontal reflection

profiles and horizontal transmission profiles to delineate fractures for a rock-mass stability study. There is still significant room for development of methods that enhance the detection of fractures by utilizing the vectorial nature of GPR and allow for quantitative descriptions of the fracture aperture and fill materials through geophysical inversion techniques.

The GPR response of a given fracture depends on the polarization and bandwidth of the GPR antennas, plus the incident angle of the waves on the fracture. A wavelet reflected from a thin layer is distorted by the constructive and destructive interference that occurs from multiple internal reflections (Widess, 1973). Additionally, the amount of received EM backscatter depends strongly on the polarization of the transmitting and receiving antennas, in addition to the geometry and electrical properties of the scatterer.

The purpose of this paper is to improve the characterization of fracture geometry and fill properties within rock bodies by noninvasive means. The objectives are to delineate fractures with polarimetric coherency images obtained from reflection GPR data, and to provide quantitative information on fractures from the inversion of transmission data. When polarimetric coherency is determined, it mitigates the effects of polarization on field data and this improves imaging of fractures from reflection data. The coherency also provides the necessary prior information on fracture orientation for inversion. An inversion procedure for transmission data will allow fracture aperture to be determined as well as the electromagnetic fill properties. My approach is to develop a new coherency attribute and full-waveform inversion algorithms, which I describe next.

## STEP 1: COHERENCY ATTRIBUTES APPLIED TO FRACTURE IMAGING

Coherency is a traditional seismic attribute used for the delineation of trace—to—trace discontinuities in seismic waveforms. A coherency attribute compares a small window of a waveform trace with surrounding traces to provide an indicator of similarity. For example, the traces on one side of a lateral boundary between two

materials that have different characteristic propagation properties will be dissimilar to neighboring traces on the other side of the boundary and hence will be associated with a low coherency score. While such differences may be difficult to see in a migrated image, a coherency attribute image often is relatively easy to visualize. Seismic coherency has been useful in delineating faults and paleochannels (e.g. Bahorich and Farmer, 1995). A thorough review of various forms of seismic coherency attributes can be found in Chopra and Marfurt (2007). In GPR, as in seismic reflection imaging, changes in subsurface impedance and target geometry affect the shape of the observed wavelet. McClymont et al. (2008) have demonstrated the utility of seismic coherency attributes for interpreting GPR data, treating the electromagnetic field as a scalar wavefield. However, EM waves are vectorial in nature with mutually orthogonal electric and magnetic fields transverse to the direction of propagation. Features exhibiting strong directionality such as faults, fractures and edges can change the state of polarization of an incident field, which introduces bias into scalar-based GPR images. To take advantage of the vector nature of EM waves and prevent bias, fully polarimetric GPR data and processing techniques should be used. Thus, methods that combine both polarization invariant information and wavelet shape information into a single, easily interpretable, attribute are desirable for the imaging of subsurface discontinuities. To this end, the largest eigenvalue of the scattering matrix, acquired from polarimetric GPR data, is used here in conjunction with the eigenstructure coherency algorithm of Gersztenkorn and Marfurt (1996) to produce a GPR coherency attribute that is unbiased by antenna polarization. The new polarimetric coherency algorithm is applied to polarimetric GPR data acquired over fractured limestone. Analysis of the field results shows significant improvement over scalar—based coherency images for providing information on the location of possible fractures.

## STEP 2. INVERSE MODELING FOR FRACTURE CHARACTERIZATION

Traditional migrated GPR images and coherency attributes provide only qualitative information on fracture properties. Often, quantitative information on fracture properties is also required. Bradford and Deeds (2006) utilized amplitude-variation-with-offset (AVO) analysis of GPR to determine the dielectric properties of thin beds. Geophysical inverse modeling attempts to associate an observed dataset with an optimal model of the relevant subsurface physical properties. Recent research includes full-waveform inversion of tomographic GPR data (Ernst et al., 2007; Kuroda et al., 2005; Jia et al., 2002), and inversion of GPR data from natural waveguides (van der Kruk et al., 2007; van der Kruk et al., 2006). There are few examples of inversion techniques developed specifically for thin-layer discontinuities or fractures. Deparis and Garambois (2007) utilized inversion of both amplitude and phase variation-with offset (APVO) analysis of GPR reflection hyperbola acquired from a cliff face to determine fracture properties. Lambot et al. (2004) utilized a thin-layer recursion formula to estimate soil electrical properties in the inversion of 1-D stepped frequency GPR data. Gregoire and Hollender (2004) used the amplitude spectrum from 2-D time-domain laboratory GPR reflection data and a thin-layer forward model to determine the aperture and electromagnetic properties of the fill of discontinuities. That study utilized the spectral ratio between a measured reflection wavelet and a reference wavelet. Very good agreement was found between laboratory measurements and the inversion results from the GPR when the aperture of the discontinuity is greater than one—fourth the dominant wavelength of the wavelet. When the aperture is less than one—fourth the dominant wavelength, the inversion was poorly constrained and success depended on prior knowledge of either permittivity or aperture. In the second step of my two-step procedure for fractured rock characterization, I utilize a full-waveform time-domain inversion model for determining fracture aperture, dielectric permittivity, and electrical conductivity from actual GPR transmission data. The fractures are previously identified using the first step of my two-step process, namely the polarimetric coherency imaging

described earlier.

## BASIC THEORY

### Reflection and transmission for thin layers

Fractured—rock characterization using GPR depends on many factors including the contrast in electromagnetic properties between the host rock and the fracture fill, the size and aperture of the fracture, the angle of radar wave incidence, the frequency band of the GPR signal, and the polarization of the antennas. Traditional GPR systems utilize bistatic dipole or bowtie antennas that produce nearly linearly polarized EM waves in which the electric field is aligned parallel to the long axis of the antenna. When the electric field is parallel to a planar bed (TE polarization), the reflection and transmission coefficients are different when compared to the case of the same electric field oriented perpendicular to the plane (TM polarization) (Figure 2.1). The differences between the TE and TM coefficients are a direct consequence of the fundamental electromagnetic boundary conditions, i.e. continuity of tangential electric and magnetic field vectors, at material interfaces.

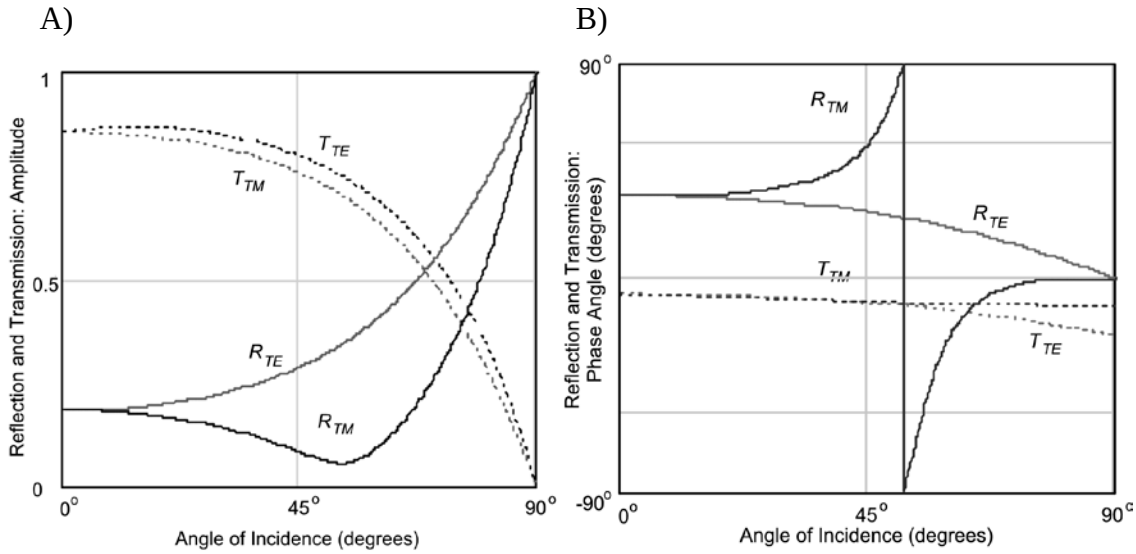


Figure 2.1. The amplitude (a) and phase (b) of the reflection and transmission coefficients. Plotted as a function of the angle of incidence for TE and TM polarized plane waves, equations 2.1-2.4, in a background medium of $\varepsilon_r = 12$, $\mu_r = 1$, and $\sigma = 0$ incident on a half space with $\varepsilon_r = 20$, $\mu_r = 1$, and $\sigma = 0.1$ S/m.

For a planar feature, of thickness greater than the longest significant wavelength of the GPR signal, the far—field reflection ($R$) and transmission coefficients ($T$), or Fresnel's equations, for transverse electric (subscript $_{TE}$) and transverse magnetic (subscript $_{TM}$) polarizations are

$$R_{TE} = \frac{\mu_2 k_1 \cos\theta_i - \mu_1 \sqrt{k_2^2 - k_1^2 \sin^2\theta_i}}{\mu_2 k_1 \cos\theta_i + \mu_1 \sqrt{k_2^2 - k_1^2 \sin^2\theta_i}}; \qquad (2.1)$$

$$T_{TE} = \frac{2\mu_2 k_1 \cos\theta_i}{\mu_2 k_1 \cos\theta_i + \mu_1 \sqrt{k_2^2 - k_1^2 \sin^2\theta_i}}; \qquad (2.2)$$

$$R_{TM} = \frac{\mu_2 k_1 \sqrt{k_2^2 - k_1^2 \sin^2\theta_i} - \mu_1 k_2^2 \cos\theta_i}{\mu_2 k_1 \sqrt{k_2^2 - k_1^2 \sin^2\theta_i} + \mu_1 k_2^2 \cos\theta_i}; \qquad (2.3)$$

$$T_{TM} = \frac{2\mu_2 k_1 k_2 \cos\theta_i}{\mu_1 k_2^2 \cos\theta_i + \mu_2 k_1 \sqrt{k_2^2 - k_1^2 \sin^2\theta_i}}; \quad (2.4)$$

$$k = \beta - i\alpha \quad (2.5)$$

$$\beta = \omega\left[\frac{\mu\varepsilon}{2}\left[\sqrt{1+(\frac{\sigma_{eff}}{\omega\varepsilon})^2}+1\right]\right]^{1/2}; \quad (2.6)$$

$$\alpha = \omega\left[\frac{\mu\varepsilon}{2}\left[\sqrt{1+(\frac{\sigma_{eff}}{\omega\varepsilon})^2}-1\right]\right]^{1/2}; \quad (2.7)$$

where ε is the dielectric permittivity, $\mu$ is the magnetic permeability, $k$ is the complex wavenumber, β is the propagation constant, α is the attenuation constant, $\omega$ is the angular frequency, and $\theta_i$ is the angle of incidence (Hollander and Tillard, 1998; Irving and Knight, 2003). Here, the effective electrical conductivity $\sigma_{eff}$ includes both DC electrical conductivity and losses associated with dielectric polarization. Dielectric losses are frequency dependent (Hollender and Tillard, 1998), but over the limited bandwidth of typical GPR systems dielectric loss can be treated as a static contribution to effective electrical conductivity (Irving and Knight, 2003). In conducting materials and lossy dielectrics, the radar wave velocity depends on frequency. Also, radar attenuation is frequency dependent, with increased attenuation at higher frequencies. Therefore, a wideband GPR wavelet propagating within a conductive medium undergoes significant dispersion.

In conductive media, Fresnel's equations and Snell's law remain valid; however, the physical interpretation of reflected and transmitted waves changes (Stratton, 1941). A wave reflected from conductive fracture fill is changed not only in amplitude, but also in phase, such that the angles of reflection and refraction become complex. Further details may be found in the classic texts of Stratton (1941) and von Hippel (1954). Also, in the general case in which the host medium is conductive, the angle of incidence on the planar fracture is complex. In this paper, to simplify the treatment, the angles of incidence, reflection and refraction are treated as real, which implies that planes of constant wave phase and wave amplitude are always parallel with each other.

In most near—surface geophysical investigations, open fractures, sedimentary beds, and planar fault zones are almost always thinner (a few mm or cm) than the longest wavelength of the GPR signal (typically ~1 m). In such cases, one must account for constructive and destructive interference caused by internal reflections within the thin layer. The reflection and transmission characteristics of thin layers have been studied extensively in optics (e.g. Iizuka, 2002). The effective reflection ($R_{eff}$) and transmission ($T_{eff}$) coefficients for a monochromatic plane wave incident on a thin layer of contrasting electromagnetic properties within a host medium are

$$R_{eff} = R_{12} + \frac{T_{12}T_{21}R_{21}\exp(-i\phi)}{1 - R_{21}R_{21}\exp(-i\phi)}; \qquad (2.8)$$

$$T_{eff} = \frac{T_{12}T_{21}\exp(-i\Delta)}{1 - R_{21}R_{21}\exp(-i\phi)}; \qquad (2.9)$$

$$\phi = 2k_2 d\cos\theta_2; \qquad (2.10)$$

$$\Delta = k_2 d/\cos\theta_2; \qquad (2.11)$$

$$\sin\theta_2 = (k_1/k_2)\sin\theta_i; \qquad (2.12)$$

where d is the layer thickness, $\phi$ is the two-way phase delay with respect to the transmitted signal, $\Delta$ is the one-way phase delay, and $\theta_2$ is the angle of refraction. The terms $T_{ij}$ and $R_{ij}$ are, respectively, the half-space transmission and reflection coefficients for a plane wave propagating in medium *i*, and incident upon medium *j*. The reflection and transmission terms in equations 2.8-2.9 can be determined using equations 2.1-2.4. Note that the phase delay associated with a thin layer, equation 2.10, depends on the layer thickness and the frequency of the input signal, as well as the layer electromagnetic properties. If the phase delay of the internally reflected monochromatic wave is zero relative to the primary reflected or transmitted wave, purely constructive interference occurs. If the phase delay is non—zero, a certain amount of destructive interference is present. This implies that, for a broadband GPR signal, some frequency components are reflected or transmitted more or less than others, thereby distorting the reflected wavelet.

Changes in the reflected waveform, as a function of fracture aperture, are shown

in Figure 2.2. Notice that the interference caused by the thin layer can significantly impact the wavelet shape and amplitude for even a very small change in layer thickness relative to the wavelet. The high sensitivity of GPR data to key subsurface features illustrates the potential for algorithms that can utilize full—waveform information to detect subsurface discontinuities and identify fracture properties.

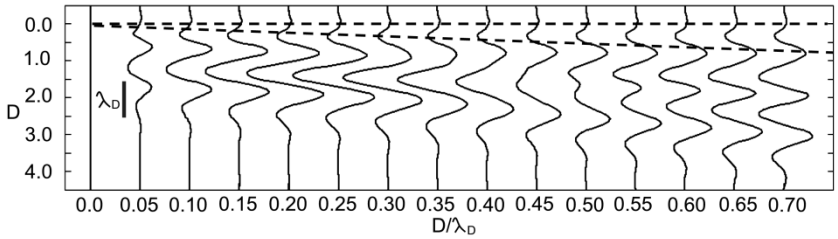


Figure 2.2. Reflected wavelets determined using a captured GPR wavelet and the thin-layer reflection model, equation 2.8, as a function of the ratio of the thin-layer thickness to the dominant wavelength of the wavelet in the thin-layer (after Widess, 1973). The dashed lines show the nondimensionalized thickness (D) of the thin-layer. The background media is $\varepsilon_r = 12$, $\mu_r = 1$, and $\sigma = 0$, the thin layer is $\varepsilon_r = 20$, $\mu_r = 1$, and $\sigma = 0.01$ S/m, and the angle of incidence is 15˚, at 15˚ there is little difference between TE and TM polarizations

**The case of arbitrary polarization and polarimetry**

The TM and TE reflection and transmission coefficients are end-members of the more general case of an arbitrarily polarized wave incident on a planar surface. In the arbitrary case, an incident wave has neither its electric nor magnetic field tangential to the interface of contrasting properties. The electromagnetic field changes polarization upon reflection and transmission; this phenomenon is sometimes called *depolarization* (Roberts and Daniels, 1996). An electromagnetic wave of arbitrary polarization can be

described by the superposition of two orthogonal electromagnetic waves (Boerner et al., 1990).

Since the strike of a subsurface feature of interest is generally unknown in geophysical applications, fully polarimetric GPR should be used to eliminate polarization bias. Traditional GPR surveys utilize dipole antennas parallel to the ground surface, thus only 2-D polarimetry will be considered here. To determine the vector describing the electric field of arbitrary polarization received at the surface, two orthogonally polarized receiving antennas are needed. Since the backscatter of an arbitrary target also depends on the polarization of the transmitting antenna, it is desirable to transmit in two orthogonal polarizations. The vector response is described by the time-domain scattering matrix $S(t)$ (Chen et al., 2001)

$$\overline{\overline{S}}(t) = \begin{bmatrix} S_{XX} & S_{XY} \\ S_{YX} & S_{YY} \end{bmatrix}. \qquad (2.13)$$

In equation 2.13, matrix element $S_{ij}$ is the intensity of the electric field at time $t$, measured at the receiving antenna of polarization $\hat{a}_j$, and backscattered from an arbitrary target that is illuminated by a transmitting antenna of polarization $\hat{a}_i$. The time-domain scattering matrix is a real—valued, symmetric matrix. The scattering matrix may be rotated to characterize arbitrary antenna polarization. The rotation of the $S$ matrix sketches out an ellipse, wherein the lengths of the major and minor axes are proportional respectively to the first and second eigenvalues $\lambda_1^S(t)$ and $\lambda_2^S(t)$ (Figure 2.3). While the terms of the scattering matrix are clearly dependent upon the $(X,Y)$ coordinate basis of the survey geometry, the eigenvalues and eigenvectors are rotational invariants. The first eigenvalue $\lambda_1^S(t)$ represents the maximum target backscatter magnitude for any antenna polarization, and hence corresponds to the GPR response under optimal polarization of the antennas.

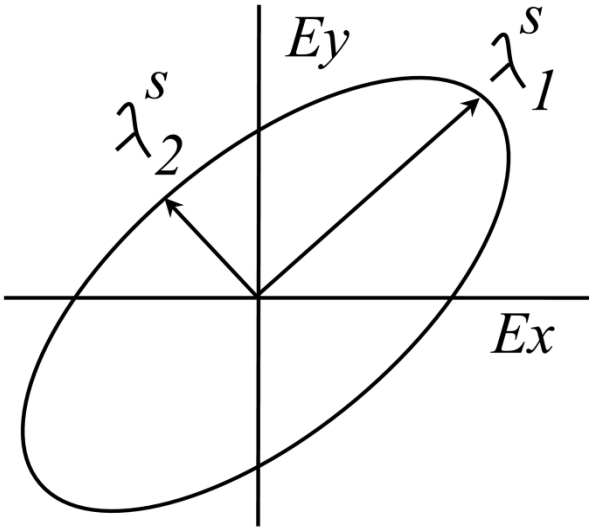


Figure 2.3. Example of a 2-D polarization ellipse. The first eigenvalue $\lambda_1^S$ corresponds to the maximum of the electric field for ideal antenna polarization in which target backscatter is maximized.

The four configurations of transmitting and receiving antennas shown in Figure 2.4 are used to populate the scattering matrix. According to reciprocity the XY and YX configurations are degenerate, so only one of the two cross-polarized configurations is needed to determine the off—diagonal terms (Roberts, 1994; Van Gestel and Stoffa, 2001). It should be noted that not all GPR systems have the flexibility to interchange the transmitting and receiving antennas, in those cases all four components must be collected. In practice, rough topography and above—ground obstacles can make difficult the precise alignment of the transmitter and receiver antennas. This leads to distortion of the scattering ellipse. Also, erroneously high eigenvalues may result when the signal to noise ratio is poor and the system noise is uncorrelated between the different components.

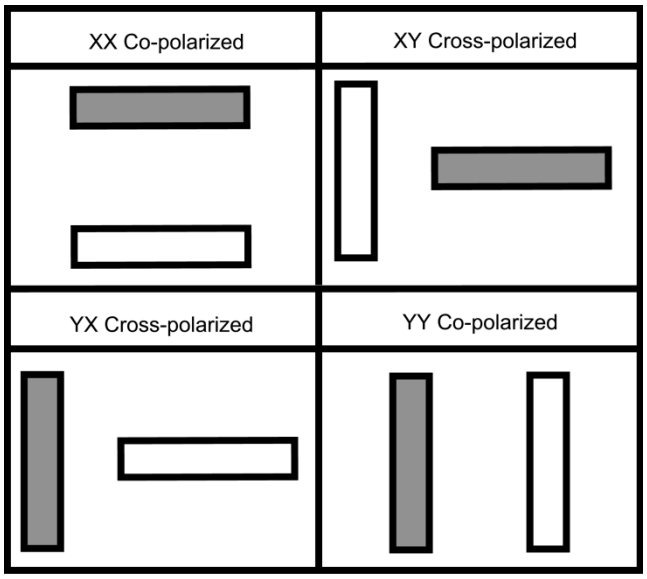


Figure 2.4. The antenna configurations used in the GPR study. The gray block represents the transmitting antenna and the white represents the receiving antenna.

Several authors have successfully demonstrated algorithms based on the scattering matrix for extracting the orientation of directional subsurface features. Van Gestel and Stoffa (2001) used Alford rotations to determine the strike of features. Seol et al. (2001) used the same approach to determine the orientation of fractures in a quarry. Chen *et al*. (2001) used eigenvalues and eigenvectors of the scattering matrix to find the orientation and aspect ratio of UXO-like targets. In these examples, the background environment was relatively simple and the target of interest was easily identifiable in the GPR data.

**Visualization of polarimetric GPR**

Visualization of fully polarimetric GPR data requires vector field plots. Such field plots can become very difficult to interpret in complicated natural environments. Thus, it is desirable to reduce the dimensionality for the purpose of easy interpretation. Previously, researchers have created psuedoscalar images from the superposition of two

orthogonal co-polarized data sets to allow for traditional seismic processing (Lehmann *et al*., 2000). However, the psuedoscalar images are only valid for weak scattering obeying the conditions of the Born approximation,

$\left|\varepsilon_s / \varepsilon_b\right| << 1$, and $s\left|k_b(\varepsilon_s / \varepsilon_b - 1)\right| << 1$,

where $\varepsilon_s$ is the dielectric permittivity of the scatterer, $\varepsilon_b$ is the permittivity of the background, $s$ is the long dimension of the scatterer, and $k_b$ is the propagation constant for the background medium (Hill, 1988). For fractured rock in which the fractures are filled with wet clay or water, these conditions are not generally fulfilled. Therefore it is very desirable to develop attribute algorithms that reduce the dimensionality of the data and tolerate noise, but retain the wealth of information afforded by fully polarimetric data. To achieve this goal, the first eigenvalue $\lambda_1^S(t)$ of the scattering matrix is critical. The coherency algorithm of Gersztakorn and Marfurt (1996), known as the eigenstructure coherency algorithm, is used in conjunction with $\lambda_1^S(t)$ to produce GPR coherency images.

## POLARIMETRIC GPR COHERENCY

The algorithm introduced here is a simple extension of the Gersztenkorn and Marfurt (1996) eigenstructure coherency algorithm in which segments of seismic or scalar GPR traces within a spatiotemporal analysis window are compared. Coherence $\gamma$ is computed using principal component analysis (Chopra and Marfurt, 2007). Principal components are calculated from the data covariance matrix, which describes the correlation and variance of the traces within the analysis window. When traces within an analysis window are very similar, the traces are highly correlated and the bulk of the variance is described by the largest eigenvalue $\lambda_1^C$ of the covariance matrix. Much of the random uncorrelated noise is orthogonal to the optimal eigenvector associated with $\lambda_1^C$. A comparison of $\lambda_1^C$ to the total variance defines the coherence $\gamma$; the formula is .

$$\gamma = \frac{\lambda_1^C}{\sum_{i=1}^{N} C_{ii}} \qquad (2.14)$$

The analysis window within which coherence γ is computed is iteratively scanned across the entire domain. In the new algorithm, the first eigenvalue of the scattering matrix $\lambda_1^S(t)$ for each time sample is used in place of the trace from a single GPR component. This is the key innovation of my algorithm. The spatial covariance matrix C is then calculated with

$$C_{i,j}(t) = \sum_{k=-K}^{+K} (\lambda_{1i}^s(t + k\Delta t) - \underline{\lambda_{1i}^s})(\lambda_{1j}^s(t + k\Delta t) - \underline{\lambda_{1j}^s}); \quad (2.15)$$

where $t$ is the time of center of the temporal time window, and $\underline{\lambda_1}^S$ is the sample mean of the first eigenvalues from the scattering matrix. The index $i$ represents the $i$—th trace within the spatial window, $j$ represents the $j$—th trace, and $2K$ is the temporal window size. The first eigenvalue of the covariance matrix $\lambda_1^C$ is calculated and then used in equation 2.14 to calculate the coherency $\gamma$ of the spatiotemporal window. Keep in mind that the eigenvalues $\lambda^C$ of the covariance matrix $C$ are not the same as the eigenvalues $\lambda^S(t)$ of the scattering matrix $S(t)$.

The newly developed algorithm is intended to significantly reduce the dimensionality of polarimetric GPR data for comparison between data traces while retaining the most important aspects of the data. Random noise can adversely affect the calculation of the eigenvalues $\lambda^S(t)$, but the use of the eigenstructure coherency method helps to mitigate the effects of random noise (Marfurt et al., 1999).

**Coherency field results**

Data for testing the GPR eigenstructure coherency algorithm were acquired on variable topography (small—scale irregularities with relief <0.2 m) atop a fractured, karst limestone. The survey area in the Glen Rose formation within the Edwards Plateau, central Texas, consists of a hydrological experimental plot (7 m x 14 m) with a 2 m deep

observation trench on the downslope side that was earlier used for the purpose of delineating preferential flow pathways (Taucer et al., 2006; Sassen and Everett, 2007). Site photographs and experimental plot description are found in the cited papers and will not be repeated here. The observation trench showed laterally continuous layers with 0.3 m of organic soil above 1.5 m of fractured limestone, underlain by marl of unknown extent. The target of the GPR study is the fractured limestone layer. Three different antenna configurations, XX, YY and YX (Figure 2.4), were used to collect reflection data over a 6.3 m x 12.7 m grid covering the surface of the plot (Figure 2.5).

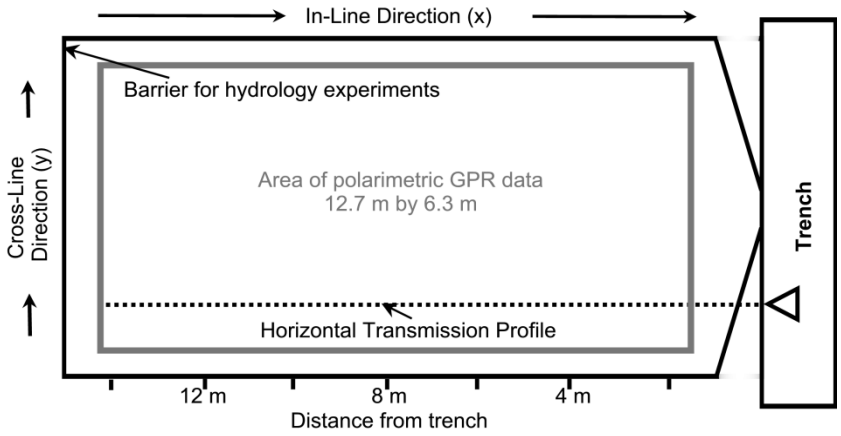


Figure 2.5. Illustration of the survey geometry of the 3-D data sets and the location of the horizontal transmission profile at the hydrologic experimentation site.

The XY response was determined from the YX data using reciprocity. All three data sets were acquired with a Pulse Ekko 100 system with a 400 V pulsed source using broadband antennas with a center frequency of 200 MHz and fixed transmitter—receiver offset 0.5 m. The spacing between stations is 0.1 m in the *x*-direction and 0.15 m in the *y*-direction. All data were stacked 64 fold and identically processed and migrated using phase-shift migration (Gazdag, 1978) with GPR—specific software developed by the first author. A migration velocity of $v=c/\sqrt{12}$ was used based on CMP gathers at the site. Following the processing and migration the coherency algorithm was applied. Migrated

time slices at 32 ns for each of the three components are shown in Figure 2.6 to enable comparison with the coherency results, Figure 2.7. The coherency algorithm gave encouraging results with a 5-trace spatial window, and an 8-sample time window (3.2 ns).

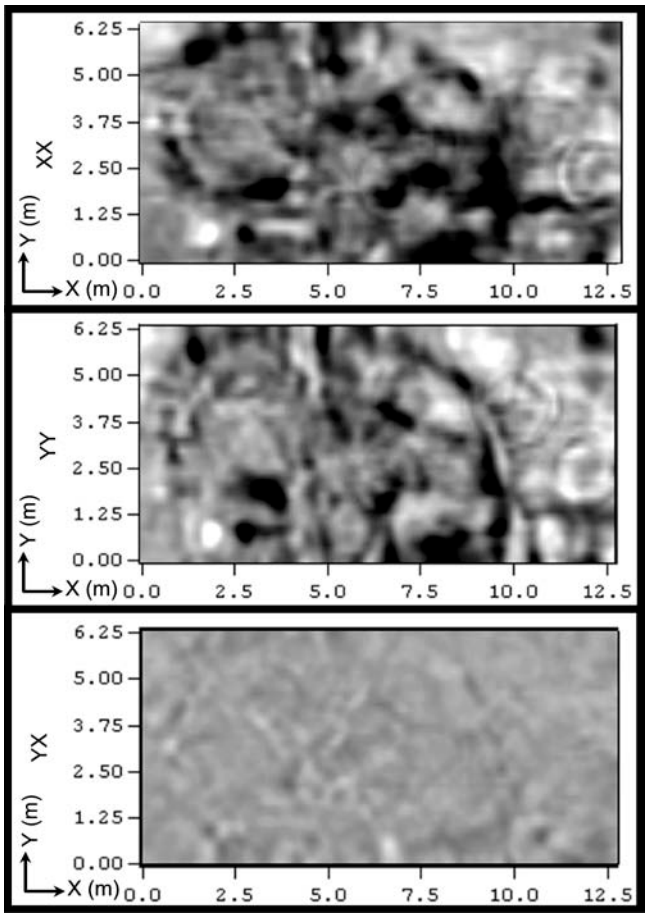


Figure 2.6. GPR time slices for the XX, YY and XY components at 32 ns. Each panel is shown with the same amplitude range and contrast settings so that the amplitude responses of each component can be compared.

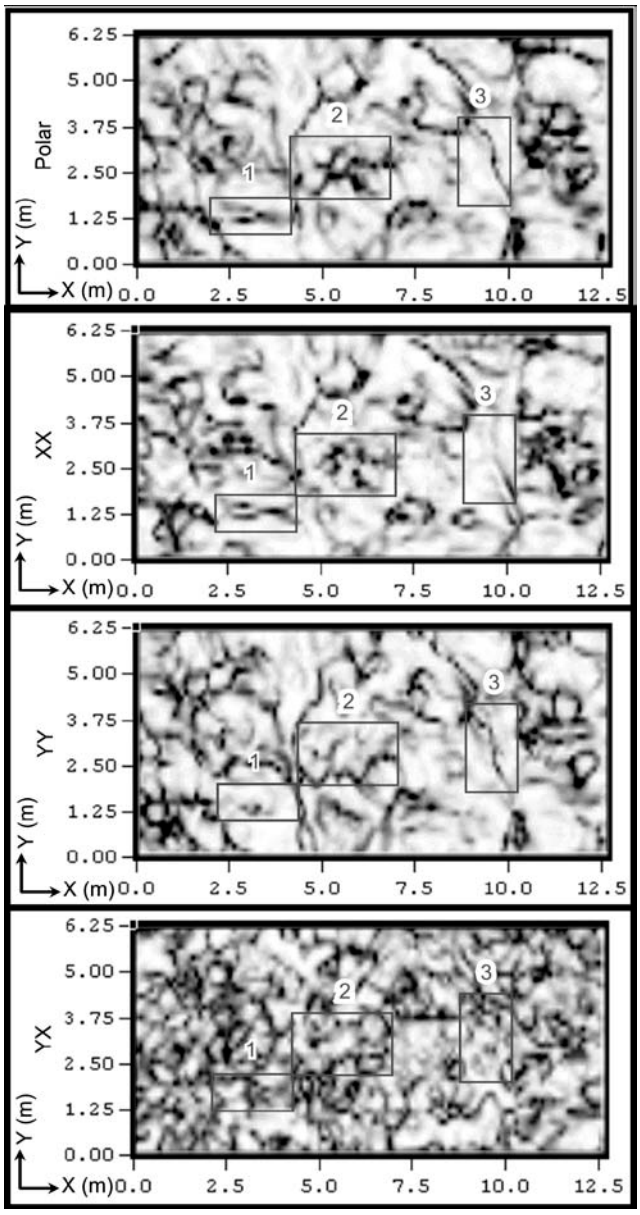


Figure 2.7. The polarimetric coherency slice (Polar) of the field data at 32 ns is shown along with the scalar coherency slices (XX, YY, and YX) for comparison. The boxes indicate areas of interest. In each panel the coherency ranges between 1 and 0, they are displayed with identical contrast, and darker areas represent lower coherency approaching 0. All scales are in meters.

The results show that the polarimetric coherency algorithm provides a much higher—contrast subsurface image, compared to the migrated time slices, and furthermore is not

biased by the polarization of the transmit and receive antennas. Figure 2.7 also shows a comparison of coherency slices of individual GPR components (bottom 3 panels) against the coherency slice (top panel) using the fully polarimetric data. In focus area 1, the left most box, a discontinuity can be clearly seen in the XX component that is very weak or obscured in the YY and YX components. The XX image indicates that this feature is best imaged with the antennas aligned parallel to its strike, and may have been missed had only YY or XY polarized data been acquired. This same feature is clearly seen in the polarimetric-based coherency image, which is derived from all the components. In focus area 2 the polarimetric coherency image appears as a composite of the YY and XX configurations. In focus area 3, a segment of a dominant discontinuity is weak in the XX configuration and is obscured in the YX configuration, while uninterrupted in the YY configuration. Again, the continuity of this feature could have been missed without the proper acquisition polarization. This same segment is shown with high contrast in the polarimetric-based coherency image. Essentially, the construction of a fully polarimetric coherency slice guarantees that a subsurface feature is imaged if it responds to at least one of the XX, YY, or cross—polarization configurations. It is not necessary to know in advance which of these polarizations is best—suited to imaging the subsurface feature. Figure 2.8 contrasts coherency images from the eigenvalues of the scattering matrix, a psuedoscalar coherency image created from a superposition of the YY and XX components, and a coherency image utilizing the eigenvalues of a diagonal scattering matrix populated only by the YY and XX components. The psuedoscalar image seems to be an improvement over individual components, but does not have the clarity and contrast of the polarimetric coherency image. Also, the coherency image that utilizes the eigenvalues from the diagonal scattering matrix (panel 3) provides less detail than images from either the polarimetric or pseudoscalar techniques. When using just the XX and YY components, the eigenvalue simply represents which of the two components has higher amplitude. Figure 2.9 shows a 3-D fence diagram of polarimetric coherency to illustrate the vertical continuity of the imaged fractures seen in figures 2.7 and 2.8. The

polarimetric coherency attributes help to determine the locations and three—dimensional continuity of fractures.

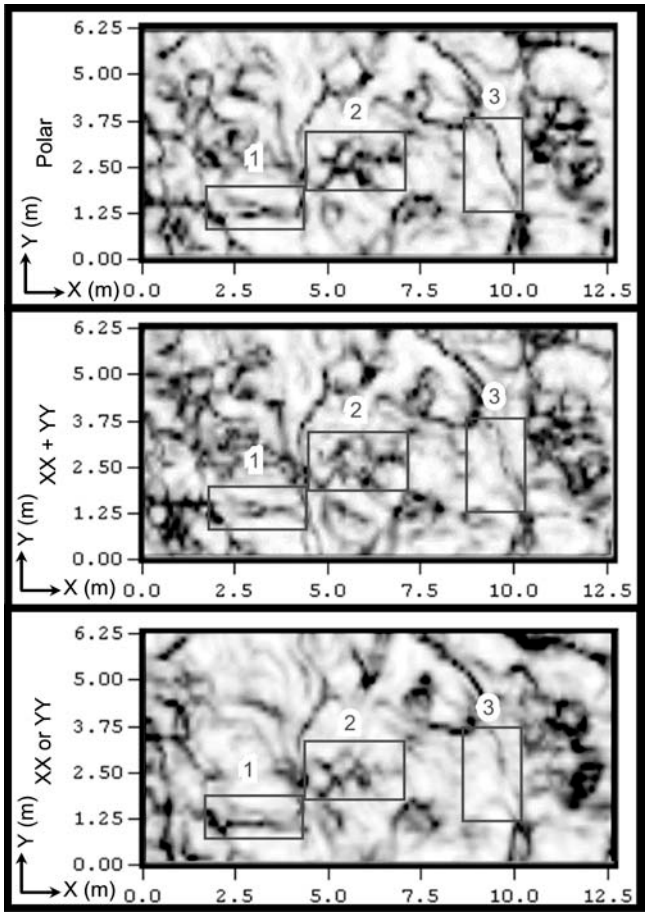


Figure 2.8. The same polarimetric coherency slice (Polar) is shown along with the psuedoscalar coherency slices (YY+XX) and the coherency based on the eigenvalues of only the XX and YY data (YY or XX) for comparison.

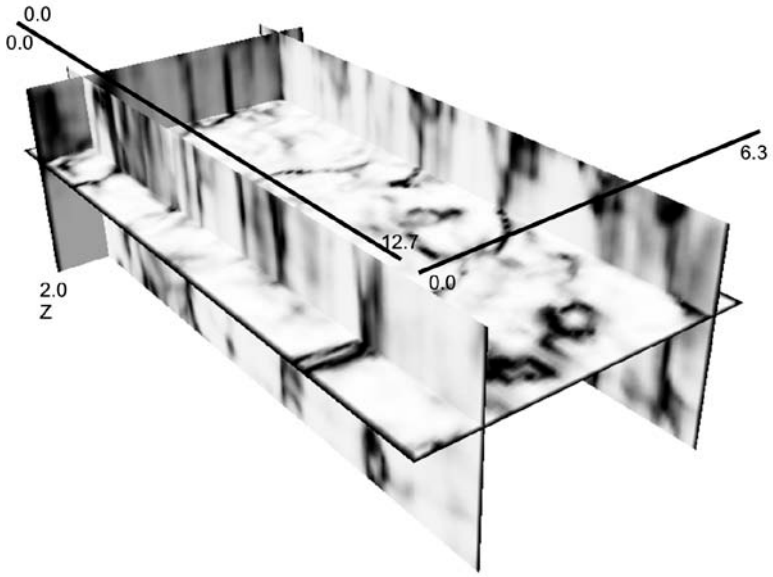


Figure 2.9. Fence diagram of the coherency data. Note the vertical continuity of the discontinuities seen in the horizontal slice at 32 ns.

## INVERSION OF TRANSMISSION DATA

Our two—step method for complete characterization of fractures requires both detection, through polarimetric coherence imaging, and a determination of the aperture and the nature of the fill materials associated with the detected fracture, through a full—waveform inversion of horizontal transmission profiles. The profiles were acquired at the Edwards Plateau site by taking advantage of the pre-existing observation trench (Figure 2.5). The transmitter antenna was placed against the vertical trench face and the receiver antenna was placed on the surface and marched out toward the opposite end of the experimental plot. The data were acquired with the Pulse Ekko 100 system using broadband antennas with a 100MHz center frequency and 0.2 m station spacing. The 100 MHz antennas were used to provide long—range GPR signal penetration. A similar acquisition technique has been previously used by Jeannin et al. (2006) to determine the location of fractures and to generate velocity tomograms. Both the transmitter and

receiver antennas were aligned parallel with the trench. The received signal retained significant power to a range of 8.0 m. The horizontal sounding profiles indicate reflections from subsurface vertical discontinuities and also reveal discrete steps in the first arrival time of the transmitted direct wave (Figure 2.10). Aside from the presence of a significant discontinuity, the changes in arrival time could be caused by changes in the thickness and properties of the thin soil layer on the surface. Radar propagation through a fracture generally alters the phase of the wavefield, making accurate picks of first arrival time difficult. To address these ambiguities in interpretation, inversion modeling has been performed on the direct ground waveforms to provide a quantitative estimate of fracture aperture and fill.

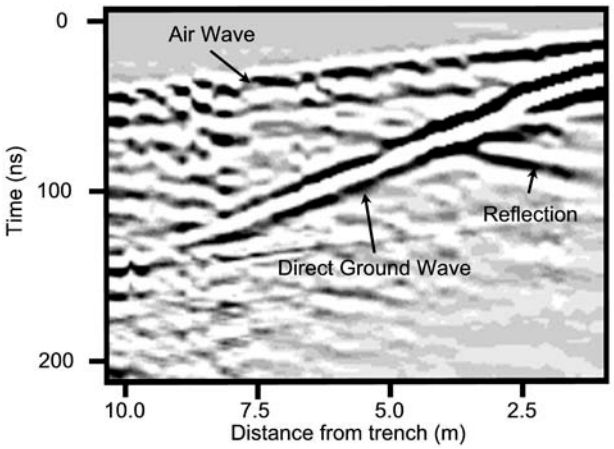


Figure 2.10. The horizontal transmission profile. The trench is to the right. Changes in slope of the direct ground wave indicate a change in the lateral velocity.

The various frequency components of a transmitted radar wavelet are changed in both amplitude and phase when passing through a thin layer. In the time domain, these changes are expressed as a distortion of the shape and amplitude of the transmitted wavelet. With this in mind, the scheme for estimating the fracture properties is to isolate a wavelet of the direct ground wave for use as a reference wavelet. The reference wave

$E_{ref}(t)$ is then transmitted through a forward model of a fracture, which may be regarded as a filter, for comparison with an observed wavelet $E_{obs}(t)$ acquired from a station further along the transmission profile. The wavelet $E_{obs}(t)$ presumably has been distorted by an actual fracture embedded in the subsurface. The forward model parameters are then iteratively updated to best match the filtered reference wavelet with the observed distorted wavelet.

**Preprocessing**

In order to isolate a reference wavelet for inversion, several filtering steps must be performed. To remove air—wave arrivals propagating at the speed of light, an *f-k* dip filter was applied to eliminate signal energy at slopes corresponding to free space propagation. In fact, the *f-k* filter was designed to cut positive slopes of all angles; this has the effect of removing interference from reflections. The *f-k* filter was based on a Butterworth filter to minimize spurious signal energy corresponding to frequencies in the sidebands of the filter response. Following *f—k* filtering, the data were cosine tapered around the direct arrival to remove extraneous noise. After the direct arrival was isolated in this manner, the amplitudes were corrected for spherical spreading and for the radiation pattern of the antennas. The approximate far-field amplitude pattern of GPR dipole radiation, as reviewed by Jiao et al. (2000), was used to account for the antenna pattern as a function of the angles of reception and transmission. This antenna pattern assumes no dependence on frequency.

**Inverse modeling**

The forward modeling algorithm requires first decomposing the reference wavelet $E_{ref}(t)$ into monochromatic waves in the Fourier domain $E_{ref}(\omega)$. Each frequency component (0 Hz – 625 MHz) is then multiplied by the model transmission coefficient $T_{eff,}$ equation 2.9, to simulate propagation through a fracture, according to

$$E_T(\omega) = T_{eff} E_{ref}(\omega) \exp(-ik_1 l / \cos\theta_i). \qquad (2.16)$$

The forward modeling also accounts for the propagation through the background medium, since $l$ is the horizontal distance along the surface and $\theta_i$ is the angle of incidence, while $k_1$ is the propagation constant for the host rock. The relative dielectric permittivity of the background medium is $\varepsilon_r$=12.0, estimated from the average velocity of the horizontal transmission profile and CMP gathers acquired at the experimental plot. The electrical conductivity of limestone in general is highly variable, ranging from ~0.003 S/m or more for weathered limestone to ~0.0002 S/m or less for intact rock. In this paper I use a nominal value of 0.005 S/m (Sharma, 1997) for all the inversions. The magnetic permeability of free space $\mu_r$=1 was used for all media. Following the model—based adjustment in amplitude and phase for each frequency component, as prescribed by equation 2.16, the data are transformed back into the time-domain. The forward-modeled wavelet $E_T(t)$ is then compared to a captured wavelet $E_{obs}(t)$ corresponding to a receiver location at some distance (a nominal 0.4 m was used) further from the trench (Figure 2.11). The value of 0.4 m is based on a compromise between minimizing the distance from the reference trace while having a propagation path through a subsurface fracture.

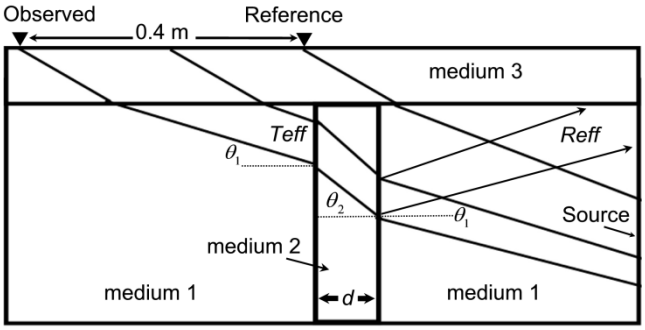


Figure 2.11. Idealized ray paths in the transmission profile. The reference signal is not influenced by the presence of the joint, while the ray path of the observed wavelet has been altered by the presence of a vertical joint.

The fracture model parameters, which include fracture aperture, the average dielectric within the fracture, and conductivity, are iteratively updated until the modeled wavelet best matches the observed wavelet.

The simple forward modeling scheme described above is based on plane—wave source excitation, thus it is strictly valid only in the far field. However, the 3-D reflection images and coherency slices, representative examples of which were shown earlier in this paper, indicate that the most significant subsurface discontinuities are nearly vertical. Furthermore, the limestone fractures are through—going in the sense that they extend from the underlying marl to the overlying soil interfaces, and they trend nearly parallel to the trench face. Thus, I have built the model on a reasonable assumption of TE—mode (electric field parallel to the fracture plane) excitation of a vertical discontinuity. The forward model also assumes that the soil layer is uniform in the area between the two traces so that there are no major changes in the wavelet from trace to trace as a result of soil lateral heterogeneity. Also, the forward model assumes that any changes in the angle of incidence between the transmitter and receiver caused by a non—planar fracture surface are not significant.

The Levenberg-Marquardt nonlinear inversion scheme was used to invert the data. A thorough review of the Levenberg-Marquardt (LM) technique is given in Pujol (2007). In order to simplify calculations the partial derivatives for the Jacobian terms are calculated numerically using a centered-difference scheme. The model variables were constrained to lie within the ranges ($0.0<\sigma<0.15$ S/m), ($1.0<\varepsilon_r<81.0$), and ($0.0<d<0.4$ m). The conductivity range spans free space to conductive clays; the permittivity range spans free space to water; while the fracture thickness $d$ spans the range of apertures likely to be encountered at the field site. The inversion is strongly dependent upon the starting model, so that a systematic variation of the starting model is used to find the best fits for each pair of reference and observed wavelets.

The suitability of a given model is evaluated using the $\chi^2$ merit function,

$$\chi^2 = \frac{1}{N}\sum_t^N \frac{(Mod_t - E_t)^2}{\sigma_t^2} \qquad (2.17)$$

where $\sigma_t^2$ is the variance of the observed response at time $t$. The modeled GPR response is $Mod_t$ while the observed response is $E_t$ As the acquired dataset consists of a 64—fold stacked trace, the variance in the data is not directly available and must be estimated. The variance $\sigma_t^2$ is estimated based on the observed radar amplitudes at the three consecutive times $t$—$\Delta t$,$t$, and $t$+$\Delta t$. This procedure for variance estimation effectively biases the inversion in favor of slow changes, while relaxing the fit requirements of rapidly changing transitions between amplitude peaks. Also, radar amplitude data with an absolute value less than 2% of the maximum amplitude are excluded from the $\chi^2$ calculation. This procedure reduces the effect of background noise on the inversion. The LM algorithm successfully terminates after a target value of $\chi^2$<1 is reached.

**Validation of the inversion model on synthetic data**

As the simplified forward model of GPR thin—layer reflection and transmission, reviewed in this paper, includes a number of limiting assumptions, the inversion model was tested on synthetic data generated by the 2D-FDTD model GPRMax (Giannopoulos, 2003). The FDTD model provides an idealized case to test the applicability of the inversion. The FDTD model contains the geometry and approximate physical properties of the materials observed from the observation trench (Figure 2.12). To match the sampling of the field data (Figure 2.13), the synthetic data generated using the FDTD algorithm were resampled with Shannon's sampling equation (e.g. Jerri, 1977),

$$E(t') = \sum_{t=0}^{\infty} E(t) \frac{\sin(\pi / \Delta t(t - t'))}{\pi / \Delta t(t - t')}, \qquad (2.18)$$

where $t$' is the required time sample for the field observations, and $t$ is the time index used by the FDTD algorithm. The time—resampled synthetic data were then put through the same preprocessing and inversion routines as would be the case for the actual field data.

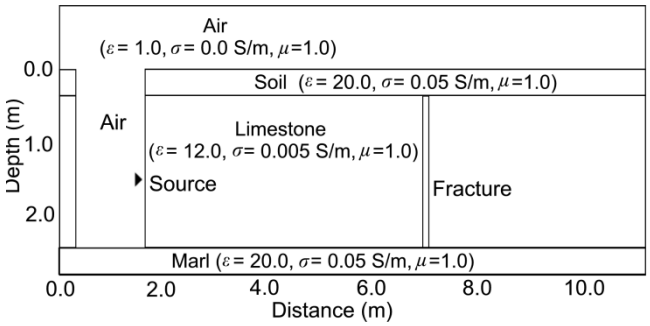


Figure 2.12. The FDTD model geometry and material parameters. The source is a Ricker wavelet with a center frequency of 100 MHz. The FDTD grid is 0.01 by 0.01 m and all boundaries are absorbing. The electromagnetic properties and aperture of the fracture are summarized in Table 2.1.

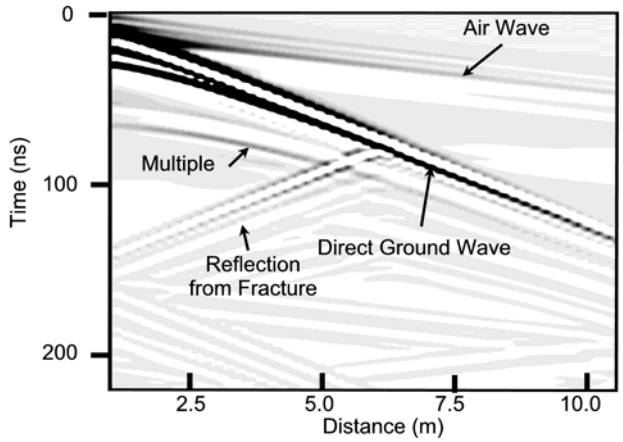


Figure 2.13. An example of the synthetic data generated from the geometry and properties shown in figure 2.12 with a 0.08 m soil filled fracture. The synthetic data was recorded at 0.2 m intervals along the soil air interface and resampled to 0.8 ns.

The inversion results for the synthetic data (summarized in Table 2.1) show that the technique is most effective for fracture apertures greater than 5% (>0.04 m) of the dominant wavelength within the fill material (~0.8 m). At a fracture thickness of less than 0.04 m, the best-fit inversion result is unreliable, i.e. the dielectric and the conductivity of the fill are poorly estimated. Essentially, the transmitted GPR wave does not respond to an electromagnetically thin fracture.

Table 2.1. Inversion results for the FDTD data. The FDTD fracture parameters were used in the model setup of figure 2.12 and are shown with the best-fit inversion results on the synthetic data. The model labels indicate different types of fracture fill, Air represents air fill, Min represent a remineralized fracture, and Soil represent a moist soil fill.

| **Model** | **Best Fit Inversion Results** | | | | **FDTD Fracture Parameters** | | |
|---|---|---|---|---|---|---|---|
| | **Aperture meters** | **Relative Permittivity** | **Conductivity S/m** | $\chi^2$ | **Aperture meters** | **Dielectric relative** | **Conductivity S/m** |
| Air 1 | 0.15 | 1.00 | 0.00E+00 | 0.06 | 0.16 | 1.00 | 0.00E+00 |
| Min 1 | 0.15 | 8.99 | 5.00E-03 | 0.02 | 0.16 | 10.00 | 1.00E-02 |
| Soil 1 | 0.11 | 21.66 | 9.19E-03 | 0.12 | 0.16 | 25.00 | 1.00E-02 |
| Air 2 | 0.10 | 1.00 | 0.00E+00 | 0.05 | 0.08 | 1.00 | 0.00E+00 |
| Soil 2 | 0.04 | 25.57 | 1.51E-02 | 0.04 | 0.08 | 25.00 | 1.00E-02 |
| Air 3 | 0.05 | 3.99 | 8.04E-06 | 0.13 | 0.04 | 1.00 | 0.00E+00 |
| Soil 3 | 0.03 | 18.74 | 1.32E-07 | 0.04 | 0.04 | 25.00 | 1.00E-02 |
| Air 4 | 0.05 | 4.00 | 7.73E-06 | 0.09 | 0.02 | 1.00 | 0.00E+00 |
| Soil 4 | 0.03 | 3.97 | 1.00E-05 | 0.07 | 0.02 | 25.00 | 1.00E-02 |

## Inversion field results

The fracture inversion was next performed for observed trace pairs along the entire length of the horizontal profile. The inversion failed to converge for any of the trace pairs located in the first 3 m of the profile. This failure is likely caused by breakdown of the far-field assumption. At transmitter receiver offsets greater than 8.0 m, the level of convergence also degraded. The signal to noise ratio at these distances is low. Furthermore, the 3-D time—slice images also suggest that the trench—distal subsurface is more complicated in architecture than the trench—proximal subsurface. The best convergence of the inversion corresponds to receiver locations near the discontinuities labeled A1, A2, S1 and S2 that are seen in both the 3-D images (Figure 2.14, *top*) and the reflections in the horizontal transmission profile (Figure 2.14, *bottom*).

An appreciable number of the total trace pairs along the profile converged to the target merit value $\chi^2<1$ (Table 2.2). A visual comparison of the observed wavelet and the forward—modeled wavelet for the inversions centered at 4.0 m (A1) and 6.4 m are shown in Figure 2.15. The two wavelets show close agreement especially at A1.

Table 2.2. Selected inversion results for the field data. The labels correspond to the interpreted fractures in figures 2.14a and 2.14b. The interpretation labels are: BG, is background heterogeneity, FC, is the inversion model failed to converge to a satisfactory level, Soil, is a soil filled fracture, Dry Soil, is a fracture filled with dry soil, and Air, is an air filled fracture.

| **Inversion Results for Field Data** | | | | | | |
|---|---|---|---|---|---|---|
| **Label** | **Distance meters** | **Aperture meters** | **Relative Permittivity** | **Electrical Conductivity** | **Chi Square** | **Interpretation** |
| | 3.8 | 0.14 | 8.8 | 1.90E-02 | 0.56 | BG |
| **A1** | **4.0** | **0.09** | **1.3** | **0.00E+00** | **0.27** | **Air** |
| | 4.2 | 0.12 | 8.5 | 2.16E-02 | 0.53 | BG |
| | 4.4 | 0.23 | 10.2 | 3.14E-02 | 0.34 | BG |
| | 4.6 | 0.09 | 9.7 | 8.94E-03 | 0.68 | BG |
| A2 | 4.8 | 0.10 | 4.0 | 1.00E-04 | 0.71 | **Dry Soil** |
| | 5.0 | 0.11 | 31.4 | 2.47E-02 | 1.48 | FC |
| | 6.0 | 0.03 | 12.1 | 1.23E-01 | 0.78 | BG |
| **S1** | **6.2** | **0.05** | **24.8** | **6.76E-05** | **0.73** | **Soil** |
| | 6.4 | 0.16 | 17.4 | 2.01E-02 | 13.93 | FC |
| | 7.6 | 0.13 | 8.8 | 2.85E-02 | 0.76 | BG |
| **S2** | **7.8** | **0.04** | **34.1** | **1.61E-03** | **0.94** | **Soil** |
| | 8.0 | 0.15 | 4.0 | 8.59E-02 | 1.53 | FC |

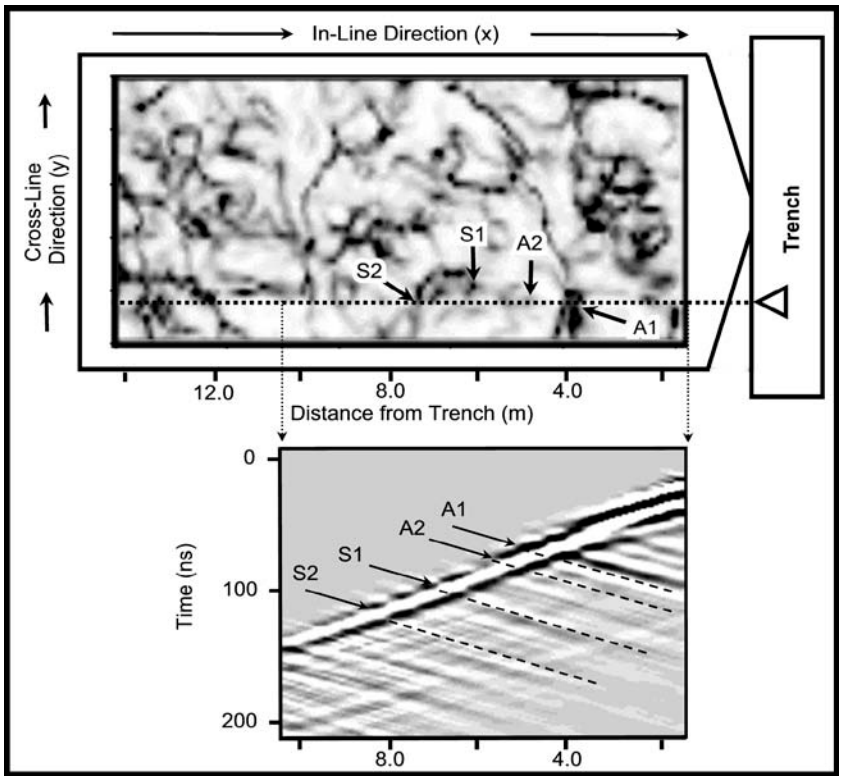


Figure 2.14. The best inverse models correlate with discontinuities outlined in the coherency image (A) and with the fractures interpreted from the YY reflection data (B) amplitudes.

The tabulated inversion results indicating low relative dielectric permittivity and electrical conductivity suggest that the strong reflection seen in the horizontal profile (Figure 2.14, *top*; feature labeled as A1) is a wide—aperture, air-filled fracture. The inversion results indicating high relative dielectric permittivity and electrical conductivity (features labeled S1 and S2) suggest that those fractures are soil—filled. The A2 inversion result doesn't appear to correspond to a recognizable fracture in the coherency image.

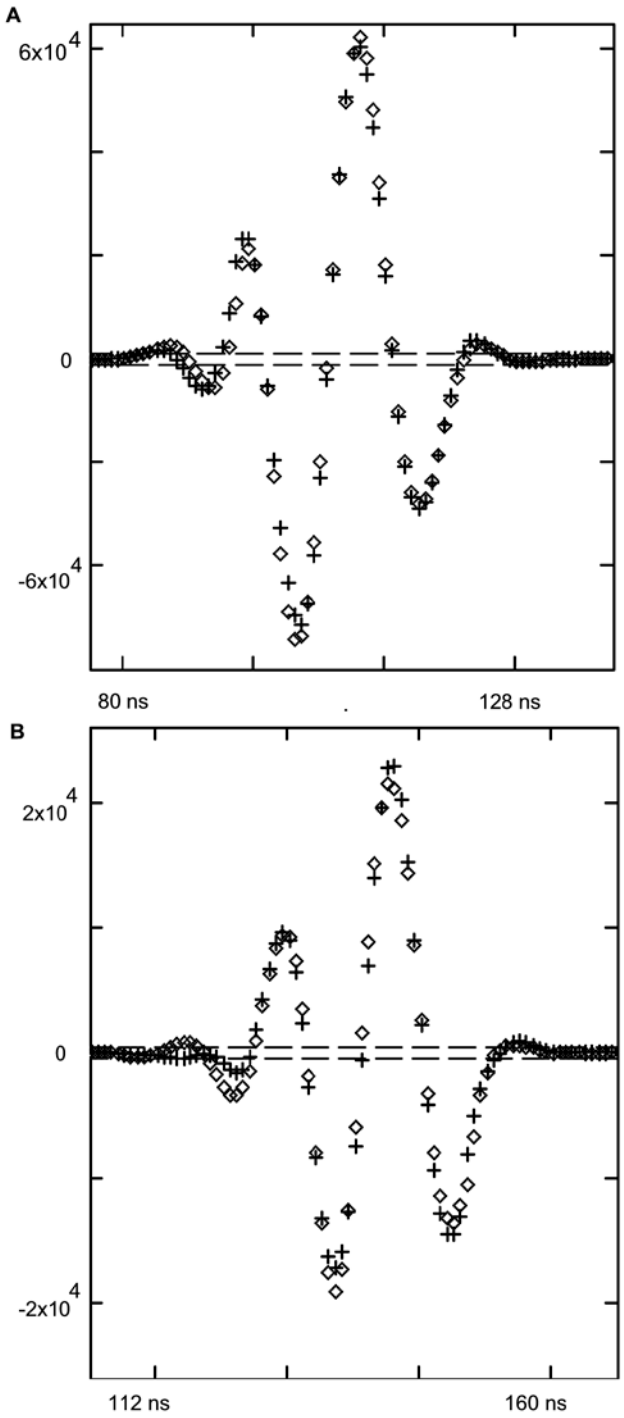


Figure 2.15. This figure illustrates the close agreement between the observed data (crosses) and the inverse model result (diamonds). Panel A shows the inversion centered at 4.0 m (A1 of Table 2.2) and panel B shows the inversion centered at 6.4 m (Table 2.2). The horizontal dashed lines demark the upper and lower limited of the data excluded from the merit function.

## DISCUSSION

The combination of fully polarimetric GPR coherency and inversion of transmission data provides improved fractured—rock analysis compared to traditional single—component or pseudoscalar GPR reflection data processing. The polarimetric coherency algorithm is introduced for the purpose of enhancing fracture detection, but the algorithm is also suited for any application where traditional coherency algorithms may be applied, especially if there is significant directionality to subsurface targets. This approach is also not exclusive to GPR, it may also find use with multicomponent shear wave data. Additionally, the algorithm can easily be extended to 3-D scattering matrices, and the eigenstructure coherency algorithm that is adapted here can be extended to imaging subsurface dipping features (e.g. Marfurt *et al*., 1999).

Improved migration algorithms specifically designed around the patterns of GPR antennas should also improve GPR coherency. In this study, the phase-shift migration algorithm of Gazdag (1978) was used to remove the effects of propagation from the raw data. This migration technique does not correct for the radiation pattern of the transmitter and receiver over a half-space, which departs significantly from the source pattern of a simple acoustic source. Multicomponent GPR imaging techniques (e.g. Streich and van der Kruk, 2007) are preferred which do account for the radiation pattern of the GPR transmitter and receiver. Incorporating this advanced imaging technique would further remove influence of the acquisition basis from the final coherency image.

Unlike the polarimetric coherency attribute algorithm, inverse modeling of the horizontal transmission data provides quantitative information on fracture thickness and the electromagnetic properties of the fill. The electromagnetic properties of the fill can be related to material properties, as required, using standard petrophysical relationships. A rigorous petrophysical analysis significantly enhances fracture rock characterization when used in conjunction with techniques such as coherency and direct sampling. However, the results in this paper indicate that a reliable inversion is limited to conditions of good signal to noise ratio and a valid far-field assumption. The far-field

assumption is often not satisfied in many GPR surveys. Also, the geometry of the fracture needs to be established prior to defining the forward model. The forward model is based on a plane-wave assumption, and assumes that a natural fracture or joint can be modeled as a continuous planar zone of constant thickness with homogeneous fill. Also, it assumed that the host rock and soil layer are homogeneous. General modeling techniques such as the finite-difference time-domain method can introduce additional flexibility into the forward model. The caveat to this is a significant increase in computation time and the inherent numerical stability issues associated with finite-difference modeling. The use of the full analytic radiation pattern of a dipole over a half space (Streich and van der Kruk, 2006.) in conjunction with the thin layer model could improve upon this work without great computational expense. The inversion technique depends heavily on the choice of starting model. Other inversion techniques such as the nonlinear conjugate gradient method in conjunction with global methods such as grid-search may improve on finding the global minima with fewer starting models. Also, further constraints on the starting model could be obtained directly from imaging or improved attributes. The validation of the inversion technique on synthetic data showed that the limits of reliability are reached when the fracture is approximately 5% of the dominant wavelength. Thus, the use of broadband GPR equipment with a higher center frequency than the 100 MHz used in this study would be desirable for the characterization of fractures, with the caveat of lower penetration depth.

## CONCLUSIONS

The polarimetric coherency algorithm shows significant improvement over traditional pseudoscalar imaging or scalar coherency algorithms for the delineation of subsurface discontinuities. The inversion of the horizontal sounding profiles shows promise in providing quantitative information on fracture aperture and fill that scientists and engineers need to adequately characterize fractured rock formations. The best approach to comprehensive fractured rock characterization remains integration of GPR

imaging and inversion with prior geologic knowledge, direct sampling, and other geophysical techniques. It is important to recognize that the polarimetric coherency image provides constraints for data inversion, while the inversion gives valuable insight into the character of the fractures seen in the coherency image. Together, the two techniques provide significantly more insight into fractured rock character than traditional GPR studies or discrete subsurface sampling alone. My inversion technique is limited in the range of application by the simplicity of the thin-layer forward model that assumes ideal geometry and homogenous layers. With continued improvement in attributes that enhance fracture delineation and more robust modeling methods, GPR methods may allow for quantitative insight into fractured rock during hydrologic or mechanical tests on field scale rock formations. The combined polarimetric—coherency/transmission—inversion method described in this paper could be applied in rock quarries, as there often exists the combination of vertical and horizontal outcrop faces.

# CHAPTER III

# ECOHYDROGEOPHYSICS AT THE EDWARDS AQUIFER: INSIGHTS FROM POLIMETRIC GROUND-PENETRATING RADAR*

## SUMMARY

Three-dimensional multicomponent ground-penetrating radar (GPR) reflection data and horizontal GPR transmission profiles were acquired and analyzed to better understand the interaction of vegetation with subsurface flow conduits at a hydrologic experimentation site. Previous researchers conducted a set of shallow (< 2.5 m) subsurface hydrology experiments during simulated rainfall events within a small plot (7 x 14 m) on the fractured and karsted limestone of the Edwards Aquifer region near San Antonio, Texas, USA, to better understand the influence of *Juniperus ashei* brush control on the local hydrology. Tracer experiments showed a high degree of variability in tracer recovery, advection speed, and concentration depending on the location of the application of the tracer. Both 3-D multicomponent GPR reflection images and coherency, and inversion of GPR horizontal transmission profiles were utilized to identify the main conduits of flow within the experimentation site in order to explain the observations of the experiments. The 3-D multicomponent GPR and coherency images revealed that the most obvious potential conduits run nearly parallel with the observation trench. Inversions of the horizontal transmission profiles indicate that some conduits are filled with soil while others have no fill. This information helps explain the high spatiotemporal variability observed in the tracer data. Additionally, the GPR and hydrologic experiments suggests that *Juniperus ashei* significantly impacts

---

*Reprinted with permission from: Ecohydrogeophysics at the Edwards Aquifer: Insights from polarimetric ground-penetrating radar Sassen, D.S., M.E. Everett, and C.L. Munster, 2009, Near Surface Geophysics, **7**, no. 5, 427-438., 2009, by EAGE.

infiltration by redirecting flow towards its roots occupying fractures within the rock. This study demonstrates that GPR provides a noninvasive tool that can improve future subsurface ecohydrologic experimentation.

## INTRODUCTION

The consequences of anthropogenic alteration of natural ecosystems are of pressing global concern, with implications for both water resources and atmospheric carbon levels. Changes in land use practices and fire control have allowed woody brush to expand into grasslands, deserts and disused agricultural land. The encroachment of brush and forest has been linked to decreases in water yields (Bosh and Hewlett, 1982). Brush encroachment in the United States is thought to lead to a significant sequestration of atmospheric carbon ($0.122 \times 10^{15}$ g C/year from 1980-1990) in the form of increased biomass (Houghton et al., 1999, Pacala et al., 2001). These studies may be of limited applicability to all ecosystems, especially environments in which landscape physiography significantly impacts water and carbon fluxes (e.g. Huxman et al., 2005).

The lack of adequate subsurface characterization has led to an underestimation of the influence of subsurface processes on ecosystems. The complexity of the subsurface has important influences on ecohydrology. For example, Jackson et al. (2002) showed that when subsurface variations in soil organic carbon are considered, there is a negative relationship between brush invasion and stored carbon in humid environments. Wilcox *et al*. (2008) showed that increased woody brush cover is correlated to increased, rather than reduced, groundwater volumes in an environment that is dominated by subsurface karst flow, rather than porous media flow. There is a need for non-destructive methods to investigate shallow (<10 m) subsurface ecological interactions. In this paper I explore the use of ground-penetrating radar (GPR) in a plot scale study of the impact of *Juniperus ashei,* an invasive brush species, on fractured epikarst limestone hydrogeology in central Texas, USA.

In the semiarid region of the southwest United States, human settlement over the

past 150 years has altered the natural environment of grassland and savannah into shrubland through the suppression of natural fires and intense grazing (Van Auken, 2000). The consequent proliferation of *Juniperus ashei*, a deep rooted evergreen shrub, within the central Texas rangeland is hypothesized to reduce recharge into local streams and the Edwards aquifer (Wilcox, 2002; Olenick et al., 2004). Careful management of the Edwards Aquifer of central Texas, USA, is important since it is the primary source of water for 1.7 million people including the residents of San Antonio (EAA, 2006). The water of the karst Edwards aquifer is under intense demand, with aquifer discharge exceeding annual recharge rates during the 1990's (Dugas et al., 1998). The demand will become even greater with continued population growth. There is a great deal of interest in restoring the natural ecology through brush control with hopes that it will increase rangeland productivity, and increase stream flow and aquifer recharge (Olenick, et al. 2004). The state government of Texas subsidizes brush removal from the contributing areas that provide recharge to the Edwards Aquifer in hopes of enhancing recharge volumes.

However, some empirical studies on brush invasion and control seem to indicate that brush removal is not an effective means of enhancing groundwater volumes in the Edwards aquifer region. One previous field study (Dugas et al., 1998) on the change in evapotranspiration and surface runoff following shrub removal within the Edwards Aquifer recharge zone indicates only temporary (3 years) gains in water yields. Wilcox et al. (2008) showed that in a similar karst environment brush encroachment increases groundwater yields. It was suggested that brush enhances infiltration and allows a larger portion of water to bypass evapotranspiration. Additionally, *Juniperus ashei* roots may enhance subsurface flow through the enlargement of joints within shallow limestone and by providing preferential pathways (Dasgupta et al., 2006). The effect of *Juniperus ashei* on subsurface fractures and karst features remains uncertain.

The subsurface hydrology in fractured rock and karst environments is typically characterized by the occurrence of discrete flow conduits (Bear *et al*., 1993). The 3-D geometry of fractures and karst features, along with the type and distribution of the fill

material, substantially impacts bulk hydraulic properties. Isolated cores, sampled at a few discrete points, are largely inadequate for a complete hydrologic characterization. Consequently, the use of geophysical techniques, such as ground penetrating radar (GPR), is advantageous since they provide continuous subsurface information. The acquisition and processing of scalar GPR reflection data has been successfully applied to the characterization of fractured rock (e.g. Grasmueck *et al*., 2005; Jeannin et al., 2006; Talley et al., 2005) and karst (e.g. Kruse et al., 2006; Tallini et al., 2006) environments. Most available GPR hardware and software is designed for scalar GPR techniques, however there are significant advantages to utilizing the vector nature of the GPR electromagnetic (EM) signal. when dealing with targets exhibiting long slender antenna-like geometry, such as fractures.

The received EM signal depends strongly on the polarization of the transmitting and receiving antennas, and on the geometry and electromagnetic properties of the target scatterer. Traditional GPR systems utilize bistatic dipole or bowtie antennas that produce nearly linearly polarized EM waves. Subsurface diffracting bodies generally change the polarization of these incident waves. It has been demonstrated, for example, that a low impedance cylinder, such as a clay-filled karst pipe, is best imaged with the long axis of the antennas oriented parallel to the cylinder, while a high impedance cylinder, such as an air-filled karst pipe, is best imaged with antennas oriented perpendicular to the axis of the cylinder (Radzevicius and Daniels, 2000). Traditional GPR surveys however utilize a single antenna polarization and, as the orientation and properties of subsurface targets are generally unknown, there is a great potential for interpretation bias. An example of the relationship between antenna orientation and the GPR response of a diffracting body is illustrated in Figure 3.1.

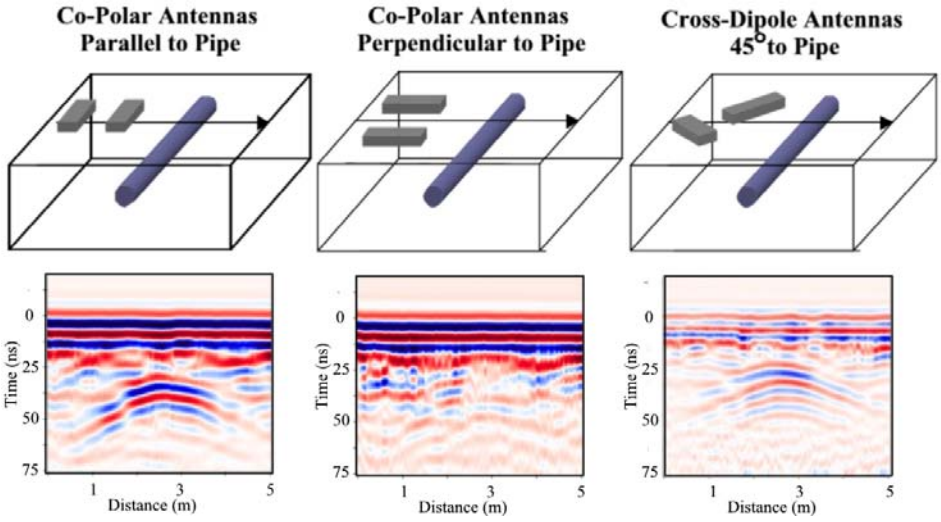


Figure 3.1: A GPR survey over a pipe in soil showing the effect of the orientation of 200 MHz antennas relative to that of a buried pipe. The PVC pipe is partially filled with water, and buried ~1.5 m in a natural, moist silty-sand soil. (After Sassen, 2008).

To take advantage of the vector nature of EM waves and to minimize imaging bias, polarimetric GPR data utilizing multiple EM components should be acquired. Previous research that focused on extracting polarization dependent information include the works Van Gestel and Stoffa (2001) and Seol et al. (2001), whom demonstrated using Alford rotations (Alford, 1986) for GPR. Alford rotations are a method by which 2-D polarimetric GPR data can determine the strike of elongate targets such as cylinders and fractures. Also, Tsoflias et al. (2004) used the polarization properties of GPR waves to detect vertical fractures in limestone. Recently, Streich and van der Kruk (2007) have developed a GPR imaging technique based on an analytic solution of the total field for a dipole over a have space that minimizes the effects of the antenna pattern on GPR data. This imaging method may provide the means to extract polarization dependent information more accurately by removing bias caused by variations in antenna patterns for the different antenna configurations used in acquiring polarimetric data. These processing and attribute extraction methods provide important detection

and discrimination insights that are not available with traditional single component GPR techniques.

Other authors have utilized the distortion of the transmitted electromagnetic wavelet caused by subsurface scatterering to enhance their detection and discrimination. The wavelet is distorted due to the constructive and destructive interference resulting from multiple internal reflections within a fracture or karst feature, as well as distortions caused by the dispersive nature of earth materials. Kofman et al., (2006) has interpreted reverberation phenomena, resulting from constructive interference, to identify air-filled cavities similar to karst pipes. Gregoire and Hollender (2004) utilized the changes in the amplitude spectrum of GPR reflection data, caused by constructive and destructive interference, as the basis for an inversion to determine the aperture and electromagnetic properties of the fill of a thin layer. Bradford and Deeds (2006) proposed amplitude-variation-with-offset (AVO) to determine the dielectric properties of thin beds. Deparis and Garambois (2007) inverted both amplitude and phase variation-with offset (APVO) data acquired from a cliff face to determine fracture properties. Lambot et al. (2004) utilized a thin-layer recursion formula to estimate 1-D soil geoelectrical properties from stepped frequency GPR data. McClymont et al. (2008) demonstrated the efficacy of coherency attributes, which respond to changes in wavelet shape, as an aid in the interpretation of GPR data from a fault zone. I build on the concept of using polarimetric GPR techniques and utilize wavelet distortion to improve upon the detection and discrimination of subsurface fractures and karst features.

Our procedure at the Edwards experimental plot is to acquire 3-D multicomponent ground-penetrating radar (GPR) data and to produce migrated images for each component. I then construct polarimetric coherency attributes using my new algorithm (Sassen and Everett, 2009) to better characterize subsurface flow conduits by looking for changes in wavelet shape. Additionally, I exploit the existing observation trench at the site to transmit GPR signals from its vertical face toward a receiver that is moved along the surface. This is done to create transmission profiles. The transmission profiles are inverted to determine the aperture and fill material of potential preferential

flow pathways at the experimentation site by utilizing a forward model of thin layer transmission. By utilizing advanced GPR techniques I minimize the potential for bias caused by antenna polarization, and I enhance the detection of subtle features. Moreover, I augment the imaging techniques with the interpretation of fracture properties based on a nonlinear waveform inversion.

Our immediate objective, using advanced GPR techniques at the site, is to identify potentially dominant subsurface conduits and to determine the geometry and fill properties of those conduits. Analysis of the GPR data is performed in order to reconcile the spatiotemporal variability in water flow and tracer concentrations observed at the site. A larger purpose is to use the GPR data to inform an investigation of the influence of *Juniperus ashei* on the subsurface conduits. The non—invasive nature of GPR data acquisition preserves the site hydrology to allow for future experimentation.

**Edwards Aquifer and the ecohydrology test site**

The recharge zone for the Edwards aquifer is a ~0.4 Mha region of central Texas (Olenick el al., 2004). The recharge zone is delineated by surface exposures of the Cretaceous Edwards formation lying within the Balcones Fault Zone (Figure 3.2). The contributing zone is defined as the surrounding areas that feed surface water and groundwater into the recharge zone.

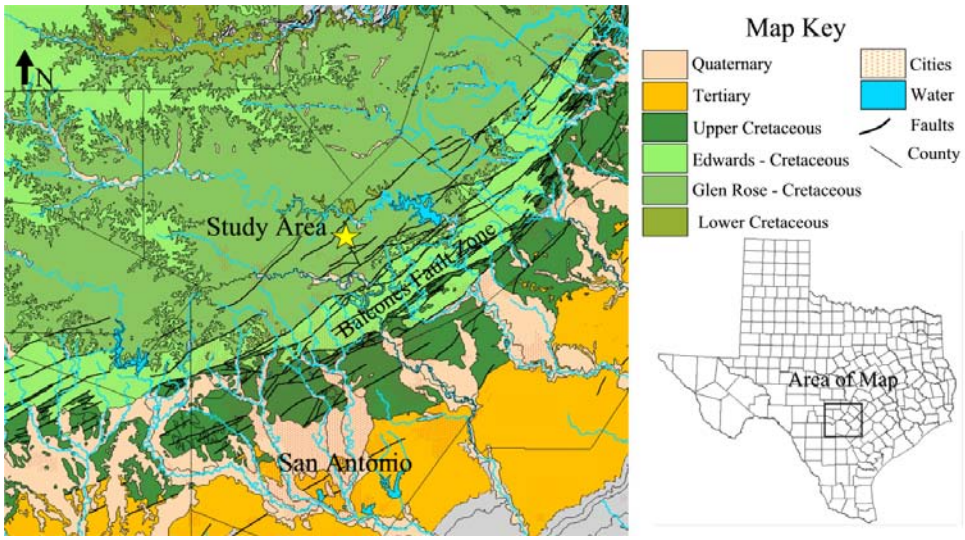


Figure 3.2. Geologic map of the Edwards Aquifer region with the location of the research site shown.

The main geologic unit of the Edwards Aquifer contributing zone, upon which the experimentation site is located, is the Cretaceous-aged Glen Rose formation. The Glen Rose formation alternates between regionally continuous layers of marl and limestone reflecting cycles of rising and falling sea level throughout the Cretaceous (Mancini and Scott, 2006). The limestone strata contain vertical conduits that enhance lateral subsurface flow while the relatively impermeable layers of marl act to baffle vertical flow. The faulting and jointing of the limestone allows acidic groundwater to flow through the relatively low permeability rock matrix, dissolving carbonate minerals and forming the karst features (Ferrill et al., 2004). Structurally, the study site is associated with the Balcones fault zone whose strike of main faulting is ~NE-SW (Collins, 1995). The more pervasive smaller-scale faults and joints generally trend both parallel and at an acute angle to the main strike of faulting, with increasing density and interconnectivity in the vicinity of the larger faults (Collins, 1987; 1995). However, under similar mechanical conditions, the pattern of joint density, orientation and aperture varies from one rock unit to the next (Collins 1995). Thus, there is significant uncertainty as to the orientation of fractures and faulting within the study site.

To study the effects of brush removal on the hydrologic cycle of the Edwards aquifer region, a hydrologic experimentation site was established (Taucer et al. 2006; Dasgupta et al., 2006) within the contributing zone, approximately 45 km north of San Antonio (Figure 3.2). The study area consists of a small, rectangular experiment plot (14 m x 7 m) within a stand of *Juniperus ashei* (Figure 3.3). The site instrumentation includes a rainfall simulator, a runoff gauge, rain gauges, soil moisture probes and a 2.5 m deep trench excavated on the downslope (2% topographic gradient) boundary of the site. The purpose of the trench, which exposes the shallow limestone and marl stratigraphy, is to quantify and sample lateral subsurface flow. Rainfall simulations were conducted on this site both before and after clearing of the *Juniperus ashei* to evaluate the hydrologic effects of brush removal.

(*a*) (*b*)

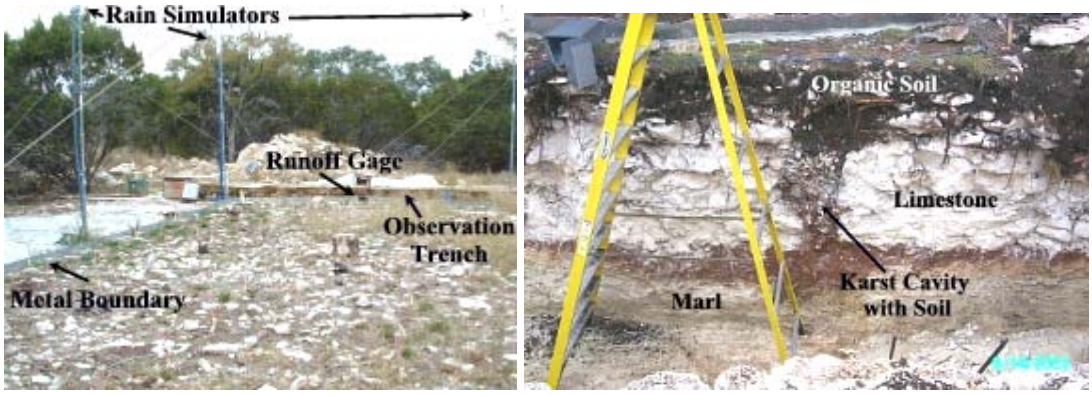


Figure 3.3. The post-cut research site showing: (*a*) the rainfall simulator and surface runoff gauge; (*b*) the downslope trench for quantifying and sampling lateral subsurface flow.

The exposed lithology in the observation trench indicates that the top 0.3 m consists of weathered limestone and organic soil; below that is 1.5 m of limestone containing joints and karst features; these layers are underlain by a low permeability

layer of marl (Figure 3.3*b* ). Soil and roots partially fill many of the exposed joints and karst features along the trench face.

**Previous results**

Hydrological experiments on the study plot were run both before and after clearing the brush. During simulated rainfall most of the lateral subsurface flow is observed to exit at the trench face in discrete locations corresponding to the joints and karst features that contain roots (Dasgupta et al., 2006). In the pre-cut condition, a greater volume of the water applied by the rainfall simulator reached the trench face compared to identical simulations performed under the post-cut condition. Taucer et al. (2006) showed that during intense rainfall simulations (0.152 m/hr), nearly all water that reached the surface of the plot infiltrated into high-capacity subsurface conduits. There was negligible surface runoff, yet only 57% of the applied water escaped from the downslope trench face. Most of that amount emerged from a very limited number of discrete joints, conduits, or bedding planes. A significant amount (16%) of the water intercepted by the *Juniperus ashei* brush was channeled by stemflow into the subsurface at the base of the brush. Although no runoff was collected on the downslope portion of the plot, ponding was observed in all rainfall simulations. Even after intense rainfall events the organic litter was observed to be dry just a few centimeters below the surface. The *Juniperus ashei* litter exhibits a high degree of hydrophobicity, or water repellency. The preponderance of stemflow and the hydrophobicity of the litter suggests that the *Juniperus ashei* may channel flow directly to its roots, promoting preferential flow to the subsurface. This raises questions about how the roots of the *Juniperus ashei* might affect the subsurface preferential flow pathways provided by fractures.

To better understand the preferential subsurface conduit system, a series of tracer tests was conducted by Taucer et al. (2006). Three non-reactive tracers were applied to the surface at different locations within the plot to allow for simultaneous monitoring during a rainfall simulation experiment. Uranine was applied to the distal upslope

portion of the site; eosine was applied in the middle of the plot around the largest tree trunk; and phloxine was applied in close proximity to the trench (Figure 3.4). Water samples from the trench face were collected for tracer analysis at 16 discrete locations that had been observed as key groundwater egress points during previous rainfall simulations (Figure 3.5).

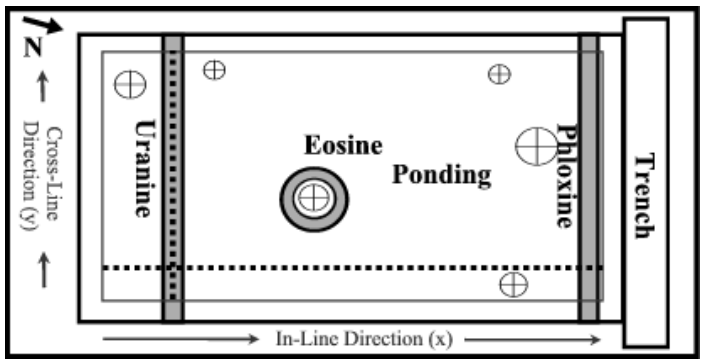


Figure 3.4. Plan view of the experimental plot. The gray box represents the extent of the 3-D GPR survey (12.7 x 6.3 m), which is surrounded by metal sheeting to capture runoff. The gray areas show the locations of the three surface-applied dyes. The dotted lines indicate the location of the in-line and cross-line GPR sections shown in Figure 3.8. The crosshairs indicate the location and relative size of *Juniperus ashei* trunks on the site. The figure is adapted from Taucer *et al*. (2006).

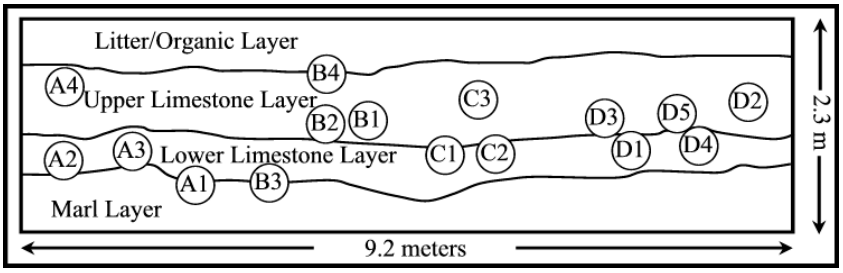


Figure 3.5. The tracer sampling locations and lithology in the vertical trench face at the downslope boundary of the experimental plot. The figure is adapted from Taucer *et al*. (2006).

None of the distal uranine applied to the upslope portion of the plot was observed to exit at the trench face. In contrast, the A and B sampling regions (Figure 3.5) showed that the proximal phloxine and the middle eosine tracers exhibited similar breakthrough patterns. In some locations (A1 and A3) the peak concentration of the mid-range eosine preceded the peak concentration of proximal phloxine, even though the mid-range eosine had traveled further. Within the C and D sampling regions only the proximal phloxine showed strong concentrations; the mid-range eosine was detected only at specific locations C1 and D4 and moreover in significantly lower concentration.

## METHODS

The methods are briefly summarized here. A more detailed explanation of the methods and their evaluation on the data within this paper can be found in Sassen and Everett, 2009.

### Multicomponent GPR images and polarimetric coherency

The 3-D multicomponent GPR data were acquired using multiple antenna configurations (Figure 3.6) following clearing of brush from the plot. In the first configuration, both the transmitter and receiver antennas are parallel to each other (co-polarized) and oriented in the in-line ($\pm x$) direction of the survey (XX component). The second antenna configuration is also co-polarized, but the antennas are oriented in the cross-line direction ($\pm y$) of the survey (YY component). The third configuration utilizes a transmitter antenna in the cross-line direction and a receiver antenna in the in-line direction (YX component).

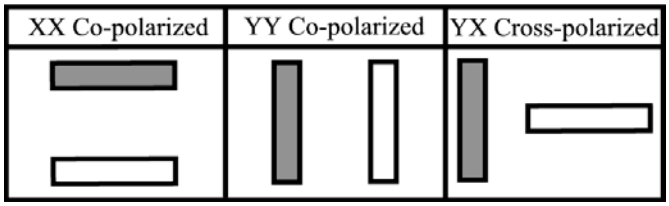


Figure 3.6. The antenna configurations used in the GPR study. The gray block represents the transmitting antenna, the white represents the receiving antenna.

All three data sets were acquired with a Sensors and Software Pulse Ekko 100 system using 200 MHz antennas. A fixed transmitter and receiver offset of 0.5 m was used, and each radar trace was stacked 64 times. The spacing between stations is 0.1 m in the in-line direction and 0.15 m in the cross-line direction. All data were identically processed and migrated, as described below, using GPR-specific software developed by the authors. Static shifts of the data, determined using cross-correlation lags, were used to adjust the travel time axis. Shifting the time axis on a radar trace proved necessary due to changes in propagation speed in the upper soil layer caused by the changing moisture conditions that occurred during the several weeks of GPR data acquisition. The data were then lowpass Butterworth filtered to remove high—frequency noise and compensated for spherical spreading and attenuation. Finally, the data were migrated using a 3-D phase-shift migration algorithm (Gazdag, 1978). The velocity model used for the migration assumed a homogeneous half-space with a speed of 0.08 m/ns, as determined from CMP gathers at the site. Since it was anticipated that fractures and other karst features of interest would distort the source GPR wavelet, the coherency of the data was calculated. I utilized the polarimetric coherency attribute algorithm developed in Sassen and Everett (2009), which combines data from each polarization to create a single unbiased coherency image. My polarimetric coherency algorithm inserts the largest eigenvalue of the time domain scattering matrix into the eigenstructure coherency algorithm of Gersztenkorn and Marfurt (1996). Using the largest eigenvalue of the scattering matrix ensures that an “optimal antenna polarization” is simulated. A localized region characterized by distorted radar wavelets, relative to clean signals

observed in neighboring radar traces, produces a low coherency score. In this way, a coherency map is built which highlights discontinuities such as fractures and karst features.

**Acquisition and inversion of transmission profiles**

In addition to the 3D multicomponent data, transmission profiles were also acquired. The transmitting antenna was placed against the vertical trench face and the receiver antenna was moved along the surface toward the upslope boundary of the simulation plot at 0.2 m intervals (Figure 3.7). Both the transmitter and receiver antennas were polarized parallel with the trench.

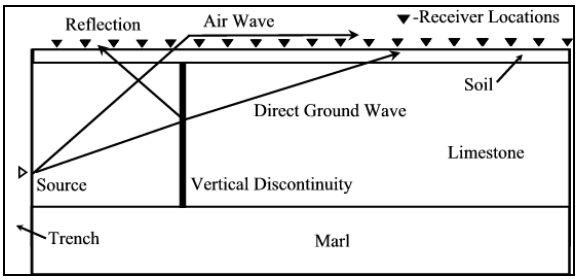


Figure 3.7. An idealized diagram of some of the possible ray paths of a GPR signal for a horizontal transmission profile in the presence of a nearly vertical discontinuity. The transmitting antenna (source) is placed on the face of the trench and the receiving antenna is moved along the surface.

The transmission data acquired at the site were used in a radar waveform inversion to determine the geometry and fill properties of some of the more significant fractures seen in the 3-D images.

The inversion scheme utilizes a forward model, equation (3.1),consisting of a reference wavelet $E_{ref}$ convolved with a theoretical expression $T_{eff}$ describing electromagnetic plane wave transmission through a thin layer (e.g. Iizuka, 2002).

$$E_T(\omega) = T_{eff} E_{ref}(\omega)\exp(-ik_1(l-d)/\cos\theta_i). \quad (3.1)$$

The modeling also accounts for propagation through the background medium, since $l$ is the horizontal distance along the surface, $d$ is the aperture of the fracture, and $\theta_i$ is the angle of incidence, while $k_1$ is the complex propagation constant for the host rock, which depends on electrical conductivity σ and dielectric permittivity ε. The convolved reference wavelet $E_T(\omega)$is compared with an observed wavelet from a radar signal that has propagated through the fracture (Figure 3.8). The reference wavelet is extracted from an observed radar signal that has not propagated through the fracture.

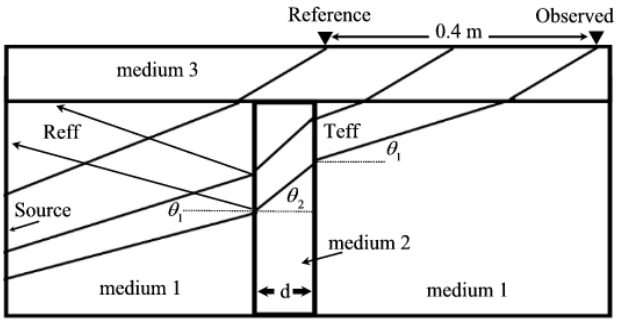


Figure 3.8. In this idealized case the ray path of the reference signal is not influenced by the presence of the vertical joint of width $d$, while the ray path of the observed wavelet has been altered by the presence of the joint.

Before the inversion, the radar signals are corrected for both geometric spreading and the far-field radiation pattern of the GPR antennas (Jiao *et al*., 2000). Next, the reference and observed signals, both associated with the direct wave, are isolated from reflections and other indirect signals through f-K filtering. The reference wavelet is then transformed into the frequency domain using a discrete Fourier transform. Each frequency component of the transformed reference wavelet $E_{ref}(\omega)$ is then applied to the forward model (equation 3.1). The convolved signal is then transformed back into the time-domain where it is then compared to the observed wavelet using a least-squares merit function for inversion.

The Levenburg-Marquadt inversion method (Pujol, 2007) iteratively updates the model parameters, which include fracture aperture and the electrical conductivity and dielectric permittivity of the fill material. The model is iterated until the merit function, $\chi^2$, has converged to a minimum value. Here, $\chi^2$ is defined as

$$\chi^2 = \frac{1}{N}\sum \frac{(Mod_t - E_t)^2}{\sigma_t^2} \qquad (3.2)$$

where $\sigma_t^2$ is the variance of the observed response at time *t*. The modeled time-domain GPR response is $Mod_t$ while the observed response is $E_t$. After the inversion, the inferred electrical conductivity and dielectric permittivity of the fracture fill is interpreted geologically using well-known petrophysical relationships (e.g. Sharma, 1997). This inversion method was repeated for pairs of reference and observed wavelets from traces spaced 0.4 m apart along the entire horizontal transmission profile. In this way, the inversion of transmission profiles was used to interpret potential hydraulic conduits at the study site.

## RESULTS

### Multicomponent GPR images and polarimetric coherency

Radar horizons interpreted from the migrated GPR data (Figure 3.9) correlate well with the observed lithological horizons that are exposed in the trench face (Figure 3.4). The two co-polarized configurations (XX and YY configurations) both produce strong responses for nearly horizontal strata, since such targets do not significantly depolarize the incident field. The lowermost limestone-marl reflection appears at 40-45 ns two-way-travel-time. With the velocity estimate of 0.08 m/ns obtained from the CMP gathers, the estimated depth to the lowest reflector is ~1.6-1.8 m, which correlates well with the observed depth in the trench. Below the limestone-marl interface, the GPR provided no useable data. The electrical conductivity of the marl is high which causes large attenuation of electromagnetic waves. The reflection at 35 ns, or 1.4 m depth, is

interpreted to be the clay-filled bedding plane separating the upper and lower limestone layer (Figure 3.5). The strong laterally continuous horizontal reflections at the top of the radar sections, termed ground clutter, are direct arrivals that partially obscure the later arrival from the soil-limestone interface.

Small breaks in the continuity of the nearly horizontal reflectors are interpreted as nearly vertical joints that have been widened by carbonate dissolution. A significant break in the lateral reflections is seen toward the left side of the cross-sections, which is on the upslope side of the plot. The lateral break is interpreted as due to a sinkhole that potentially provides a pathway through the low permeability marl. In the data from the YX configuration (cross-polarized), the area of the interpreted sinkhole shows relatively strong returns that indicate, as expected, strong depolarization of the incident waves (Figure 3.9).

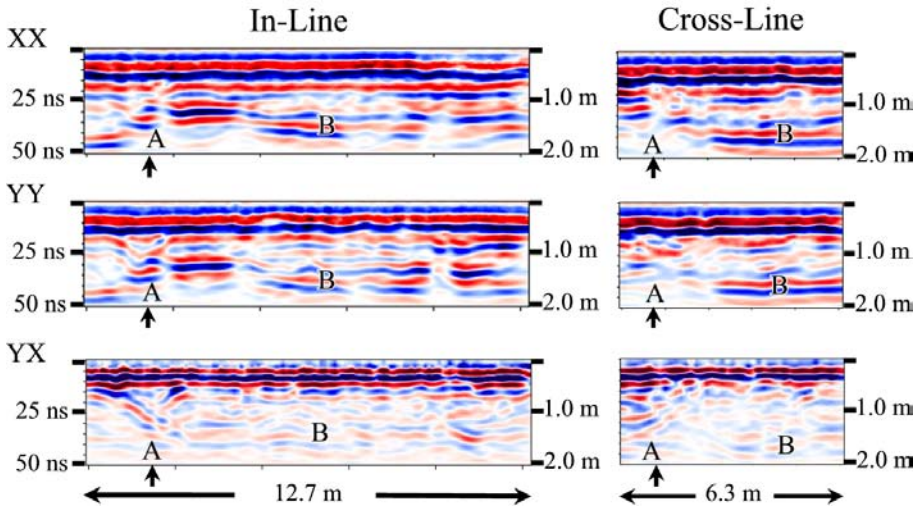


Figure 3.9. In-line and cross-line GPR sections (Figure 3.4) of the GPR data for all three polarizations. The vertical arrows mark the point where the in-line and cross-line sections intersect each other. Label (B) is the marl-limestone reflector for each antenna configuration. Label (A) represents a large break in the limestone-marl reflector in the XX and YY configurations. The strong returns seen at this location in the YX configuration are interpreted are de-polarizations caused by a sinkhole.

The conical shape of the putative sinkhole is clearly seen in a cut-away data cube of the YX image (Figure 3.10). The horizontal reflectors that are dominant in the co-polarized configurations are much more subtle in the YX configuration. This is expected since horizontal reflectors do not depolarize the incident signal. Also, dipping features that were not apparent in the co-polarized sections can be seen throughout the section (Figure 3.10).

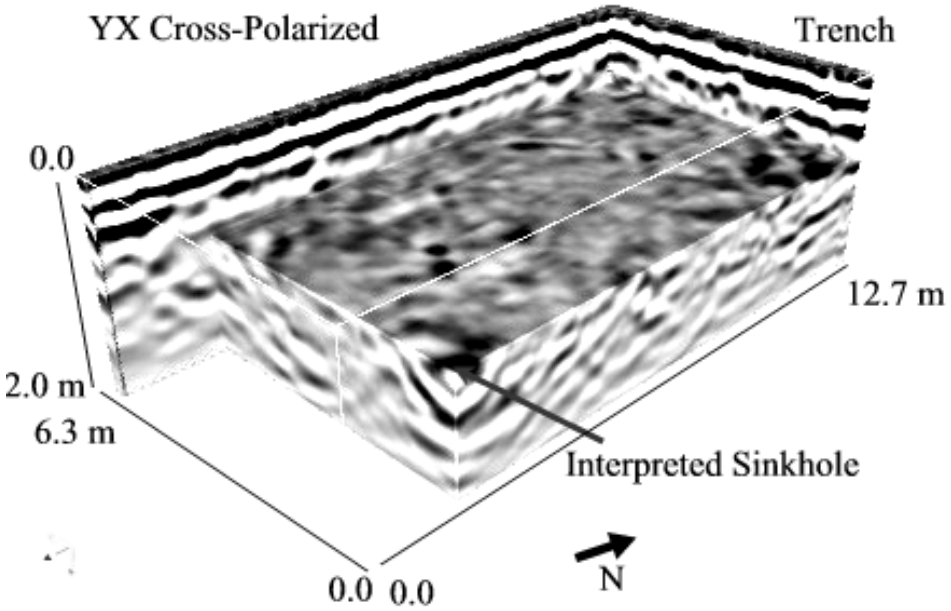


Figure 3.10. A 3-D data cube is cut away to reveal the conical geometry of the interpreted sinkhole.

Time-slices constructed from data acquired with the various antenna polarizations show that the main lateral discontinuities strike nearly parallel to the trench (Figure 3.11). Further insights can be gained from the cut—away view of the data cube shown in Figure 3.12. The discontinuities are interpreted to be fractures widened by carbonate dissolution, and they trend roughly parallel to the regional strike of the Balcones Fault zone, i.e. northeast-southwest. Discontinuities are also seen trending

perpendicular to the trench in the XX and YY polarization time-slices. They are probably caused by jointing that provides key interconnectivity between the more significant features trending nearly parallel to the trench. Additional ambiguous discontinuities can be seen, especially in the cross-polarized configuration, that trend both parallel with the main breaks and at approximately $50^{o}$ to the strike of the more obvious discontinuities. Time slices for the YX configuration tend to become more chaotic towards the upslope end of the plot where the significant break in the horizontal reflectors is observed. There are several faint circular anomalies, or rings, located on the right side of the time slices in Figure 3.11. These are likely caused by coherent cultural noise since they correspond to the location of metal stakes that were used to support the rainfall simulation towers.

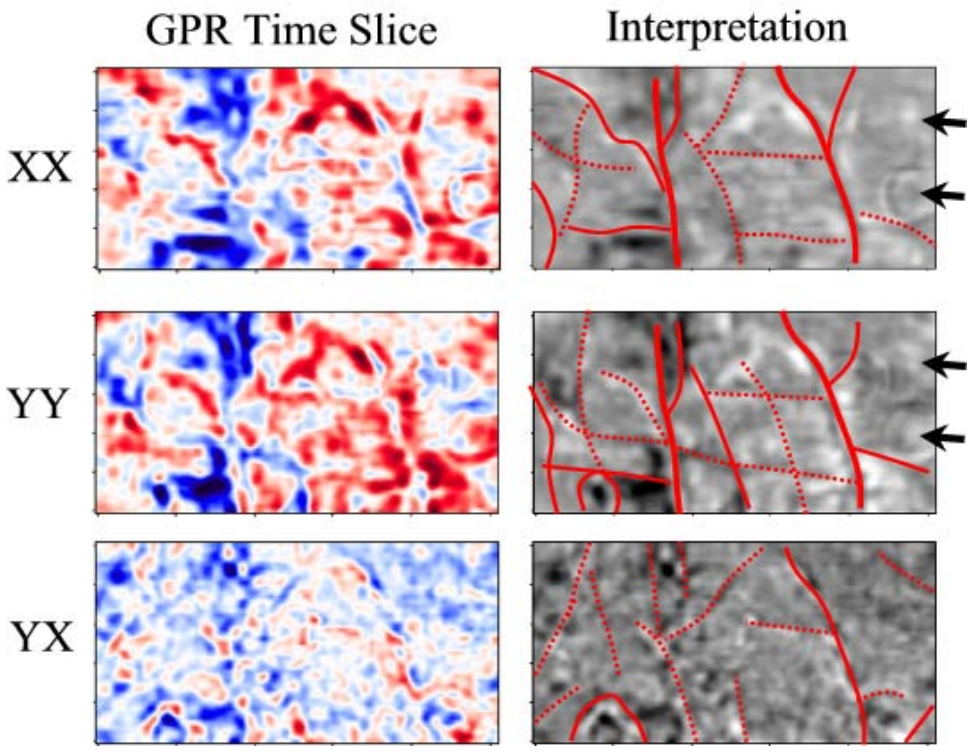


Figure 3.11. (*left*) Time slices at 32 ns, or 1.3 m depth, for all three polarizations of the GPR antennas; (*right*) the interpreted fracture locations overlaying grayscale time slices, the arrows indicate the location of the circular anomalies caused by the metal stakes.

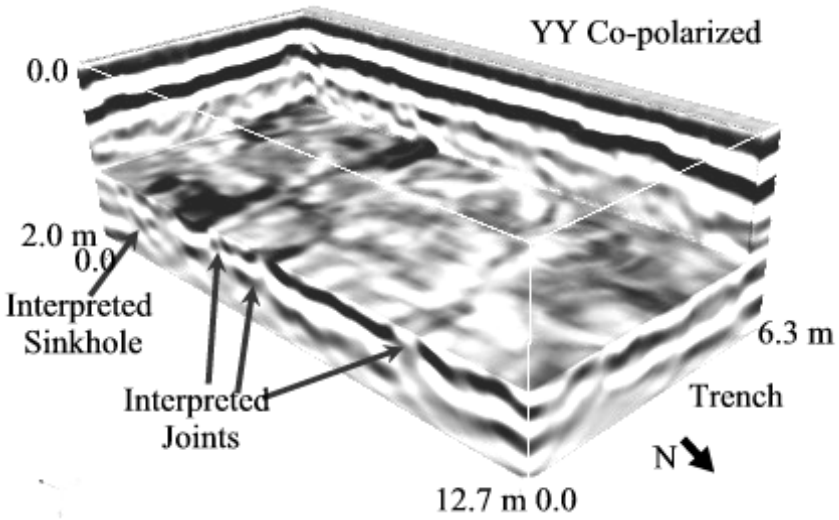


Figure 3.12. A 3-D rendering that relates the discontinuity in the reflections seen in the cross-section views to the discontinuities seen in the time-slice views.

Polarimetric coherency images aid significantly in the interpretation of subsurface discontinuities. They provide a means of evaluating, in a manner that is independent of source polarization, the amount of wavelet distortion caused by a subsurface discontinuity. Figure 3.13 shows a polarimetric coherency slice at 1.3 m depth overlaid by the position of the *Juniperus ashei* stumps. The location of the stumps correlates with zones of low coherency score. Accordingly, some of these stumps are probably aligned with significant discontinuities that are interpreted as fractures widened by carbonate dissolution. This alignment is significant in that it suggests that *Juniper ashei* preferentially grows in preexisting fractures. The roots provide access for water to infiltrate the preferential flow pathways.

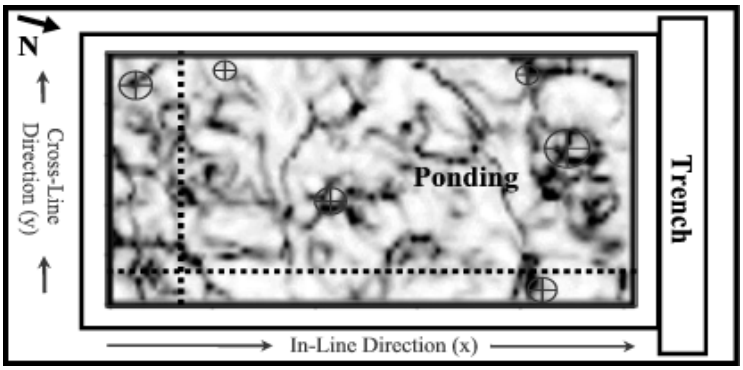


Figure 3.13. Time slice of polarimetric coherency at 32 ns (1.3 m depth), dark areas are areas of low coherency, indicating laterally discontinuous geological structure. The crosshair symbols represent positions of *Juniperus ashei* stumps.

**Inversion of horizontal transmission profiles**

While multicomponent GPR images and polarimetric coherency maps reveal the locations of potential subsurface conduits, they do not provide information about the size and fill of the discontinuities. The transmission profiles I acquired contain radar reflections from vertical discontinuities and lateral changes in the velocity of the direct ground wave. Such radargram features occur at locations that coincide with the main lateral discontinuities interpreted from the time slices (Figure 3.14). Aside from the presence of a significant discontinuity, the velocity changes seen in the transmission profiles could also be caused by changes in the thickness and properties of the thin surface soil layer. To address this ambiguity, inverse modeling is performed on the direct-wave signals.

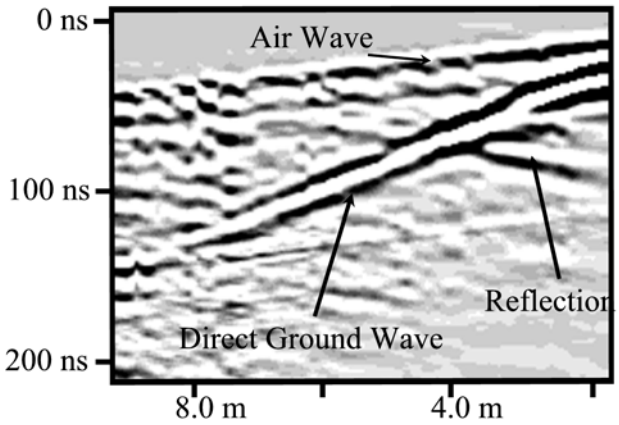


Figure 3.14. The horizontal sounding profile. The trench is to the left. Changes in slope of the direct ground wave indicate a change in the lateral velocity.

The inversion was applied to all pairs of reference and observed traces (Figure 3.8) along the entire length of the profile. The inversion failed to minimize the misfit error, or converge, to an acceptable level for any trace pairs in the first 3.0 m of the profile. This could be due to a breakdown in the plane—wave assumption of the forward model (Sassen and Everett, 2009). Also, the inversion scheme failed to converge for the pairs of reference and observed traces beyond 8.0 m. The transmitted signal to noise ratio at this distance is low and the 3-D images also suggest that this part of the subsurface is more complicated in geological structure. The best level of convergence for the inverse model (Table 3.1) corresponds to the locations of discontinuities seen in the time slices and reflections seen in the transmission profile (Figure 3.15).

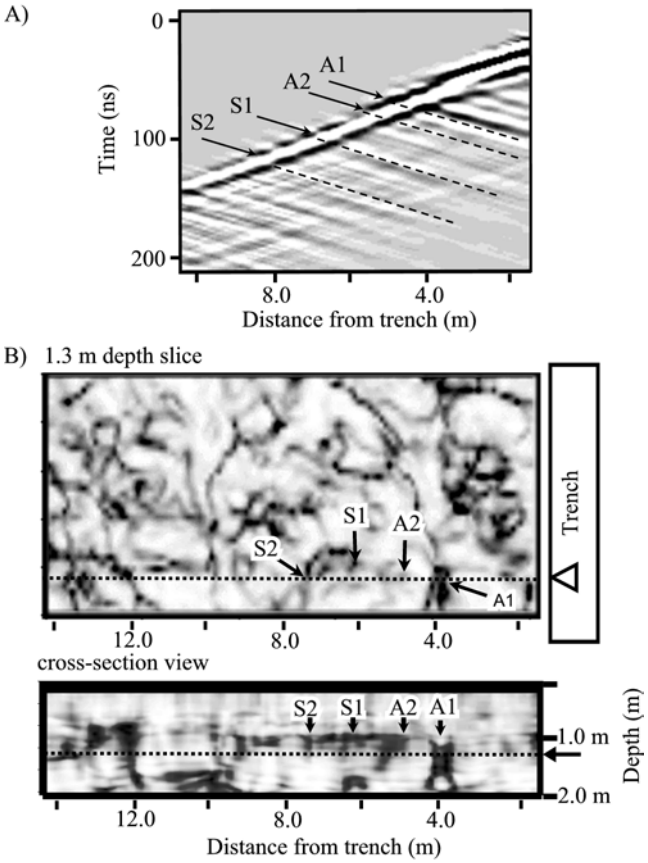


Figure 3.15. The best inverse models correlate with reflections seen in an enhanced horizontal transmission profile (A) and with the joints interpreted from a polarimetric coherency depth slice and cross-section view (B). The transmission profile shown in figure 3.14 was f-K filtered to remove shallowly dipping events and then muted at times preceding the arrival of the direct wave to enhance the appearance of the reflected arrivals. The intersections of the cross-section and the depth slice of the coherency are shown by dashed lines.

Table 3.1. Selected inversion results. The labels correspond to the interpreted fractures in figures 3.11a and 3.11b. The interpretation labels are: BG, is background heterogeneity, FC, is the inversion model failed to converge to a satisfactory level, Soil, is a soil filled fracture, Dry Soil, is a fracture filled with dry soil, and Air, is an air filled fracture.

| **Inversion Results for Field Data** | | | | | | |
|---|---|---|---|---|---|---|
| **Label** | **Distance** | **Aperture meters** | **Relative Dielectric** | **Electrical Conductivity** | **Misfit $\chi^2$** | **Interpretation** |
| | 3.8 | 0.14 | 8.8 | 1.90E-02 | 0.56 | BG |
| **A1** | **4.0** | **0.09** | **1.3** | **0.00E+00** | **0.27** | **Air** |
| | 4.2 | 0.12 | 8.5 | 2.16E-02 | 0.53 | BG |
| | 4.4 | 0.23 | 10.2 | 3.14E-02 | 0.34 | BG |
| | 4.6 | 0.09 | 9.7 | 8.94E-03 | 0.68 | BG |
| A2 | 4.8 | 0.10 | 4.0 | 1.00E-04 | 0.71 | **Dry Soil** |
| | 5.0 | 0.11 | 31.4 | 2.47E-02 | 1.48 | FC |
| | 6.0 | 0.03 | 12.1 | 1.23E-01 | 0.78 | BG |
| **S1** | **6.2** | **0.05** | **24.8** | **6.76E-05** | **0.73** | **Soil** |
| | 6.4 | 0.16 | 17.4 | 2.01E-02 | 13.93 | FC |
| | 7.6 | 0.13 | 8.8 | 2.85E-02 | 0.76 | BG |
| **S2** | **7.8** | **0.04** | **34.1** | **1.61E-03** | **0.94** | **Soil** |
| | 8.0 | 0.15 | 4.0 | 8.59E-02 | 1.53 | FC |

In general, an inversion result characterized by high dielectric permittivity and high electrical conductivity is suggestive of soil fill, whereas an inversion result of very low dielectric permittivity and very low electrical conductivity suggests an air-filled fracture. The inversion results of my GPR transmission profile data indicate that the strong reflection seen in the profile (Figure 3.15, A1) is a wide-aperture joint filled with air. The A2 inversion result doesn't correspond to a parallel fracture as the model assumes, but to an interpreted fracture nearly perpendicular to the transmitted wave. The inversion results for S1 and S2 suggest that those fractures are soil-filled.

# DISCUSSION

The GPR results provided the following observations: the main trend of jointing is nearly parallel to the observation trench; the surface location of brush trunks correlates to fractured zones within the limestone; there is a possible sinkhole on the upslope side of the plot; the inversion shows that some fractures are soil-filled while others are air-filled. Combining the GPR results and unsaturated flow theory, a conceptual model of the subsurface hydrology of the plot can be formed to explain the tracer and flow experiments. Additionally, the observations suggest new hypotheses for the role of *Juniperus ashei* in groundwater recharge and carbon sequestration in this semiarid karst environment. Finally, I can suggest potential further uses of GPR for ecohydrology.

## Conceptual model of the subsurface hydrology

Flow rates within the unsaturated zone are determined by the gradient of matric potentials, or capillary suction, along with the familiar gravitational flow controlled by the hydraulic conductivity of the medium. The unsaturated hydraulic conductivity increases with increasing saturation and pore size. Conversely, the matric potential decreases with the mean pore radius and the saturation. In dry conditions, the high matric pressures of the fine matrix of the rock and soil govern the flow within fractured rock systems. However, as saturation increases, the matric pressure decreases, and gravitational forcing through open conduits largely determines the flow.

At the experiment site, it is likely that subsurface flow during the intense rainfall experiments was focused within preferential pathways such as open fractures and karst features. Conduit flow bypasses the slower matrix flow that is driven by capillary suction. This is supported by the observed strong correlation between the applied water volume and the initiation of conduit flow out of the trench face (Dasgupta et al., 2006). Lateral flow observed at the trench should become important as saturated conduits within the limestone encounter barriers, such as the marl interface, to vertical flow. The

excavation of the trench allowed the conduits that intercepted the trench to drain freely, thereby generating a significant difference in hydraulic head between the perched flow pathways and the bottom of the trench. The hydraulic gradient created by the opening of the trench combined with the natural gradient of the plot drives most of the rainfall toward the trench. This may have caused additional lateral subsurface flow to enter the trench face, along with any tracers. However, the GPR data reveal that the main discontinuities trend parallel to the trench face. The inversion results from the horizontal transmission profile suggest that some of these conduits are soil-filled while other conduits are open. The open conduits enhance flow parallel to the trench, while the soil-filled conduits provide a barrier to flow towards the trench. In either case, the net flow is somewhat oblique to the direction of the trench. This interpretation is supported by the observation that the eosine tracer applied to the middle of the site appears mostly on the left (north) side of the trench face rather than across the entire face. Water and dye that does not arrive at the trench face is either held in storage or flows along a stronger hydraulic gradient with connections to the open conduits. The sinkhole, interpreted from the GPR data, likely provides a vertical pathway through the underlying marl layer. A large open conduit on the upslope side of the plot explains the lack of uranine tracer reaching the trench, and accounts for a portion of the "lost" 43% of infiltrated water.

**Hypotheses on water recharge and carbon sequestration**

The GPR polarimetric coherency maps suggest a strong correlation between the locations of the juniper stumps and the subsurface discontinuities at this plot. This observation, coupled with the prior knowledge that stemflow is a significant component of infiltration (Taucer et al., 2008), suggests that the *Juniperus ashei* directs water deep into the subsurface where it is available to its roots, bypassing the shallow soil where grasses may compete for water. This potential advantage for the limited water resources of a semi-arid environment may explain the success of the *Juniperus ashei* in this environment. Also, by providing a bypass of the shallow soil and directing flow beyond

the deep roots of the brush, groundwater recharge could be enhanced. This provides a mechanism that would explain the watershed scale observations of Wilcox *et al*. (2008) of increased ground water volumes following the encroachment of brush in central Texas karst systems.

An area of ponding occurs over a large open fracture, as interpreted from the GPR inversion and images. This suggests that the observed hydrophobicity of the litter strongly influences infiltration. While the observation of hydrophobic coatings from *Juniperus ashei* litter is not new, the potential significance of hydrophobicity in this environment has not been evaluated. As matric potential is driven by the attraction of the polar molecules of water to the surfaces of minerals, hydrophobicity can nullify matric pressure and cause it to change to a positive pressure (Bauters *et al*., 1998). Previous researchers have shown that the presence of hydrophobic coatings enhances preferential flow through macropores (Steenhuis *et al*., 2005). Additionally, limestone has been shown to exhibit partial wetting with water, and complete wetting with organic liquids (Taylor et al., 2000). Thus, hydrophobic coatings on limestone are not easily displaced through counter ion exchange in wet conditions, and the influence of matric pressure is potentially minimized throughout the rock mass. Therefore, the hydrophobic litter may enhance rapid conduit flow within the limestone at even low moisture levels and prevent wetting of the shallow organic soil that grasses occupy. Hydrophobicity is also an important factor in the sequestration of atmospheric carbon within soil. The hydrophobic coatings keep the organic litter dry, preventing it from easily being decomposed to release the carbon back into the atmosphere. Piccolo *et al*. (1999) showed that, in laboratory conditions, hydrophobic amendments to soil significantly reduce soil organic decomposition. They further suggested that hydrophobic amendments to soil could be used to reduce atmospheric carbon. Additional research should be directed towards better understanding the influence of the hydrophobicity of *Juniperus ashei* on infiltration, subsurface flow and carbon storage.

### Evaluation of GPR for ecohydrology

Many of the foregoing observations could have been found by careful excavation of the site. Indeed, excavation provides direct ground truth as opposed to the indirect subsurface inferences that are characteristic of a GPR study. However, GPR provides a nondestructive means of subsurface characterization that preserves the site for future experimentation. While this forensic analysis of the hydrologic experiments is useful, GPR could also be used prior to instrument installation to guide experimental design. GPR could also be used as a tool to monitor changes in the subsurface during experimentation in areas of interest. In general, GPR adds considerable value to multidisciplinary investigations of physical, chemical and biological interactions between the surface, subsurface and ecological communities.

## CONCLUSIONS

The geophysics provided evidence that *Juniperus ashei* occupies fractures and karst features within the limestone of the test plot. These fractures and karst features provide preferential pathways through which water can quickly infiltrate deep into the subsurface beyond the shallow soil. The previous observation from this test site shows that *Juniperus ashei* redirects a significant portion of intercepted rainfall directly to its roots through stemflow, and that the *Juniperus ashei* litter is strongly hydrophobic and prevents infiltration into the shallow soil. These plot scale conclusions imply important processes that may affect the entire region. *Juniperus ashei* is well adapted to access water within fractured rock while limiting water to shallow rooted plants competing for limited water in the hydrogeologic setting of the Edwards Aquifer region.. This study also suggests that the brush may enhance regional groundwater recharge by focusing water into conduits where it can bypass the soil and evapotranspiration. Without natural fires to keep *Juniperus ashei* in check, the ecohydrology of the Edwards aquifer region has been significantly altered.

This study provides support for using multicomponent GPR in the design and interpretation of shallow hydrology experiments. In the context of the ecohydrology problem at the Edwards aquifer site, GPR data identified main hydrogeological structures that control subsurface flow and the fate of tracers. If these data were available beforehand the placement of the observation trench and the placement of sensors and tracer dyes could have been optimized to provide additional information on lateral flow and the role of brush removal on the local hydrology. While identifying potential flow pathways with traditional GPR reflection data and processing is very useful, the waveform inversion results presented here provide additional detailed information on the geometry and the fill properties of the potential flow conduits.

The shallow subsurface (0 to 10 m) is one of the most complicated interfaces in the earth and ecological sciences. There are strong interactions between the physical, chemical and biological processes of the surface, the ecological communities and the subsurface. GPR is a potentially powerful tool that can provide researchers with unique insight into this important zone.

# CHAPTER IV

# DISCOVERING NEW GEOPHYSICAL KNOWLEDGE WITH THE GROWING HIERARCHICAL SELF-ORGANIZING MAP: AN EXAMPLE FROM 3D POLARIMETRIC GPR

## SUMMARY

In this chapter I apply the recently developed growing hierarchical self-organizing maps (GHSOM) to knowledge discovery from geophysical data. I also introduce an automatic labeling procedure adapted for geophysical data sets. The GHSOM is an unsupervised learning technique appropriate for clustering and interpreting data where little to no prior information exists. It displays data in both topological and hierarchical orders, and when coupled with the automatic labeling procedure, provides intuitive understanding of cluster relationships. The GHSOM is a tool for discovering patterns within geophysical data sets that can be used for target discrimination. To test the approach, GHSOM is applied to multicomponent GPR data from a shallow ecohydrologic experimentation plot situated on fractured and karst limestone of the Glen Rose formation in central Texas, USA. When the GHSOM is coupled with the migrated GPR volume and prior knowledge of the local geology, I am able to distinguish patterns identifying soil filled cavities within the limestone. These newly discovered patterns allow estimation of the volume of soil within the limestone. Such an estimate is vital for understanding carbon, nitrogen and water fluxes within the plot domain. The GHSOM with the automatic labeling scheme shows strong potential as exploratory geophysical data tools, and are particularly useful for situations in which little prior information is available.

## INTRODUCTION

The recently developed growing hierarchical self-organizing maps (GHSOM) (Dittenback et al., 2002) have potential for knowledge discovery from geophysical data in cases where little or no ground truthing is available. The GHSOM is an unsupervised learning technique appropriate for clustering and interpreting data. It displays data in both topological and hierarchical orders, and when coupled with an automatic labeling procedure, provides intuitive understanding of cluster relationships in terms of subsurface targets. Here the GHSOM is applied to 3-D multicomponent GPR data from a shallow hydrologic experimentation plot consisting of soil-covered fractured and karsted limestone. My primary objective is to evaluate the effectiveness of GHSOM combined with an automatic labeling procedure for discovering patterns from geophysical data that are useful to interpretation. My secondary objective is to find patterns within attributes extracted from the GPR data which may indicate the location of fractures and karst cavities within the limestone. It is hoped to distinguish the fill materials of these features. At this stage I lack direct samples from the subsurface that could be used to constrain the results and only have the aid of the prior geologic knowledge to evaluate the data mining results. This provides a classic unsupervised learning situation.

Ever increasing computational power and storage space has provided geophysicists with the opportunity to access and process enormous amounts of data. The proliferation of geophysical attributes has provided interpreters with greater insights. This has helped to remove some of the guess work from interpretation. Interpreters hope to recognize patterns of a particularly useful attribute, or combination of attributes, to more confidently identify features of interest. Once a correlation between patterns and targets has been established, the patterns themselves become an attribute for finding and verifying the presence of the target. However, the recognition of useful combinations of attributes is not a trivial task. The computational methods for

identifying new and useful patterns fall within the domain of knowledge discovery databases and data mining (KDD/DM) (Mitra et al., 2002).

Geophysics has its own tradition of knowledge discovery. For example, the seismic facies analysis described by Johann *et al*, (2001) closely resembles the KDD/DM process. The KDD/DM process for geophysical applications is summarized below (Figure 4.1). The process starts with basic geophysical observations, which may be raw or previously processed data. In some cases as in GPR, preprocessing may be necessary to remove effects such as attenuation, acquisition angle, or source polarization. In the next step, attributes that may be useful for finding patterns of interest are selected. These attributes usually need some preprocessing or normalization so that each attribute has a similar value and variance for the data mining stage. In the data mining stage the data is searched for distinct pattern or trends. These patterns are organized and labeled in such a way to be insightful to the user. Next, the labeled patterns are provided to the interpreter as a key or index to the data. The interpreter uses this key, along with a geospatial representation of the patterns, to evaluate which of the patterns most indicates a desired target.

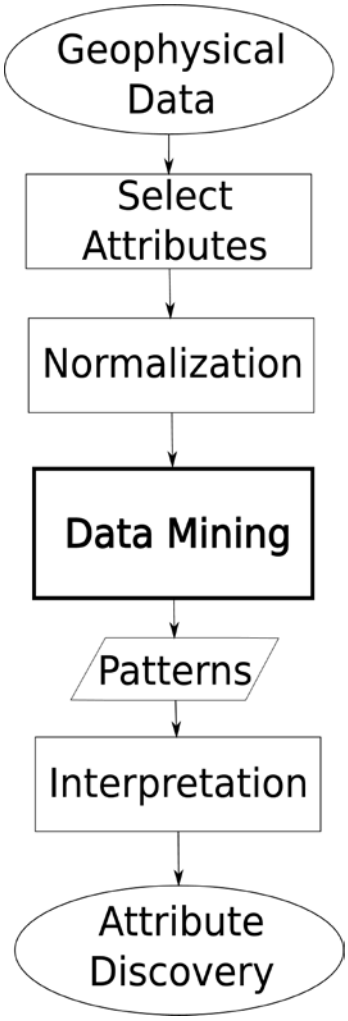


Figure 4.1. A flow chart of the geophysical attribute discovery process. This is an adaptation of the KDD/DM process (after Mitra et al., 2002).

Among the decisions needed in the KDD/DM process is the selection of an appropriate data mining technique. In geophysics it is often the case that very little prior knowledge of the subsurface is available. A class of data mining tools for such problems is the unsupervised learning techniques, also called clustering techniques. Unsupervised learning techniques group targets exhibiting similar attributes together into clusters while distancing targets exhibiting very different attributes. This is markedly different from typical pattern recognition or classification methods, in which the objective is to

place targets into groups, or classes, that most closely resemble previously labeled, or classified, representative examples.

Some of the more commonly used unsupervised classification techniques include k-means (MacQueen, 1969), fuzzy-c means (Bezdek et al, 1981), hierarchical clustering (e.g. Jardine and Sibson, 1968) and self-organizing maps (Kohonen, 1990). The popular k-means algorithm and the fuzzy-c means clustering methods require prior knowledge of the number of clusters. As a consequence of the continuity and noise inherent in geophysical data, distinct clusters often do not exist. As pointed out by Coleou et al. (2003) this characteristic of geophysical data handicaps data segmentation methods, such as k-means, that attempt to position cluster nodes as far apart as possible. "This repulsion between cluster nodes makes them sensitive to noise, prevents meaningful ordering, and leads to results heavily impacted by the selected number of classes" (Coleou et al. 2003). Because of these factors, methods that do not rely on choosing the number of clusters prior to training are preferred. As an alternative to segmentation methods, both the hierarchical clustering techniques and self organizing map (SOM) techniques do not require prior knowledge of the number of clusters, but instead thee clustering is guided by the data.

The hierarchical methods have the advantage of graphically displaying hierarchical relationships, or detail level, of the data. This allows the user some discretion as to what level of detail to analyze the clusters. Figure 4.2 illustrates the advantage of a hierarchical organization for classes of common basin sediments. An interpreter who is interested only in major divisions between salts and clastics may choose a simple representation of the data (Figure 4.2-A), while another interested in depositional facies may require a moderate level of detail (Figure 4.2-B). The prospect evaluator may be interested in the highest levels of detail (Figure 4.2-C). This provides a good demonstration of how subjective is the choice of the ideal number of clusters. It depends not only on what can be discerned from the data, but also the goals of the interpreter. Unfortunately, the hierarchical methods are computationally time consuming, scaling quadratically with dataset size, which limits their use in cases of very

large data sets (Herrero et al, 2001). Conversely, the SOM technique runtime scales linearly with the dataset size (Herrero et al, 2001). Plus, SOMs have the added advantage of expressing data of high dimensionality onto a low dimension map, where nodes representing similar data are topographically close and the map reflects the probability density function of the data (Kohonen, 1990). This is especially useful for applications in which estimates of uncertainty are desired.

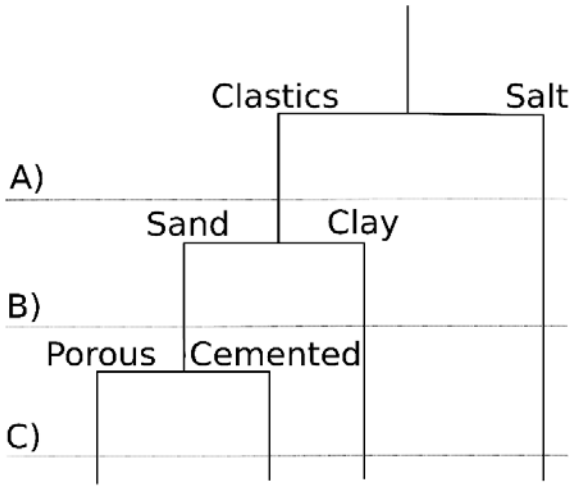


Figure 4.2. An example of a hierarchical dendrogram for typical classes of basin sediments. The user of hierarchical classifying techniques can choose from several levels of detail (A, B, or C) depending on the objective of the classification.

**SOM algorithm**

SOMs utilize unsupervised-competitive training algorithms to cluster similar inputs within the map during the training phase. The goal of the SOM is to cluster high-dimensional input data onto a lower dimension map while preserving the multidimensional-spatial relationships, or topological order, of the clusters. The SOM consists of $N$ output nodes arranged in a 2-D grid. Each node is assigned a weight vector $w_i$ of the same dimension as the output data vectors (Figure 4.3).

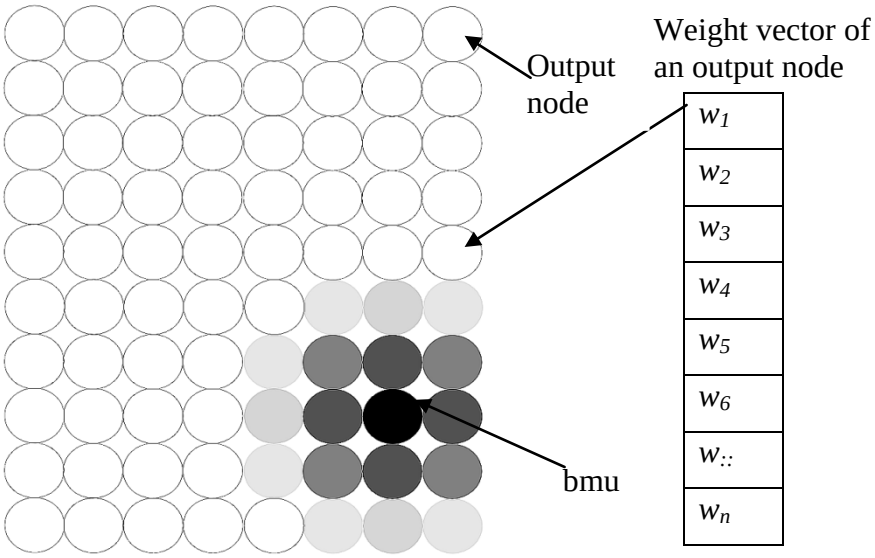


Figure 4.3. Illustration of a self-organizing map. The output nodes (circles) of a self-organizing map are typically arranged on a 2D surface. Output weight vectors are iteratively updated with each display of input vectors, with the best matching unit (bmu) being updated with the greatest learning rate (black) and the neighboring nodes updated with learning rates that decrease with distance from the bmu (shades of gray).

The weight vectors are initialized with random values. Each input vector ($x_j$) is displayed to the output nodes to determine the difference (Euclidean distance) between the input vector and the weight vector. The best matching unit (bmu) is determined; it and its neighbors are adapted to better match, or quantize, the input vector by

$$\vec{w}_i(t+1) = \vec{w}_i(t) - \alpha(t)(\vec{x}_j - \vec{w}_i(t)) \qquad (4.1)$$

where α(t) is an asymptotically decreasing learning rate. The learning rate decreases in amplitude and spatial influence according to,

$$\alpha(t) = A(t) \cdot \exp\left(\frac{\left\| r_i - r_{win} \right\|^2}{2\sigma_{(t)}^2}\right) \qquad (4.2)$$

where $r_{win}$ is the position of the winning node, $r_i$ is the position of node *i*, *A(t)* controls the amplitude of the learning rate and asymptotically decreases in time , and σ(t) controls

the spatial influence size and also asymptotically decreases in time (Kohonen, 1990). After all input vectors have been displayed, the process is repeated until a predetermined number of training epochs or level of match has been reached. Through the training, weight vectors take on the appearance of the set of input vectors best matching them. The result is a feature map consisting of output nodes that are organized in position as a function of similarity between differing weight vectors.

The SOM method has seen previous use in geophysical data analysis. In a comparison of several unsupervised learning techniques for seismic facies analysis, Marriquin et al. (2009) preferred SOMs for identifying data clusters. Castro de Matos et al. (2007) used SOMs in their process of seismic facies analysis. Klose (2006) used SOMs to analyze patterns from 6 seismic properties to interpret tomographic seismic data. Bauer *et al*. (2008) used the SOM to find clusters from the attributes of P-wave velocity, attenuation and anisotropy in tomographic data. Benavides et al. (2009) used SOMs to identify clusters separating UXOs from fragments and clutter in time-domain EM data. Essenreiter et al. (2001) used the SOM to find patterns useful for identifying reflection multiples in seismic data.

While traditional SOM methods are growing in popularity within the geophysical community, there are some limitations which need to be overcome before SOM can become a more accessible and reliable tool. The SOM requires some expertise in visually interpreting the number and boundaries of clusters. Also, the size of the SOM must be predefined before training. If the map is too small, important clusters may be grouped together. If too large, clusters may be needlessly subdivided. Without prior knowledge of the features expressed by the clusters, interpretation of the meaning of the SOM is difficult. Plus, SOMs do not provide any insight into the hierarchical structure of the data so that intuitive decisions at various levels of detail cannot be made. Several adaptations of the SOM have been developed to make it more accessible and less reliant on *a priori* information. Widely used interpretation methods include the U-matrix (Ultsch, 1993) graphic display, which simplifies interpretation by highlighting areas of significant change between clusters. Also, methods have to provide meaning to SOMs

without any *a priori* knowledge using automatic labeling procedures have been developed by Rauber and Merkl (1999) and Azcarraga et al. (2005). To alleviate the user from the requirement of defining the size of the SOM prior to training, automatically growing SOM algorithms have been introduced (Fritzke, 1994; Fritzke 1995). Finally, two of the more recent SOM adaptations of the traditional SOM's treat several shortcomings by combining automatic map growth with hierarchal growth (Herrero, et al., 2001; Dittenbach et al., 2002, Rauber et al., 2002). This development has provided a tool possessing the advantages and computational efficiency of the SOM with the intuitive organization of hierarchical clustering methods. Here I utilize the growing hierarchical self-organizing map (GHSOM) algorithm of Dittenbach et al. (2002) for unsupervised learning of geophysical data.

## THE GHSOM ALGORITHM

### Growing grid

Training of a GHSOM begins as it would for the traditional SOM, but with a small initial grid size for the first training epoch. With a growing grid SOM, the smallest size map possible (2x2) is initialized which then grows as dictated by comparisons of the mean quantization error (MQE) against the quantization error (*qe*) of its parent node (Figure 4.4). The parent node quantization error ($qe_{parent}$) gives the error between the *n* input data vectors $x_j$ that best match the parent node weight vector ($w_{parent}$).

$$qe_{parent} = \sum_{j=1}^{n} \left\| \vec{w}_{parent} - \vec{x}_j \right\| \qquad (4.3)$$

The mean quantization error of the *N* nodes of the map is given as:

$$MQE_i = \frac{1}{N} \sum_{i=1}^{N} qe_i \qquad (4.4)$$

New nodes are added in the form of rows or columns to the grid if the $qe_{parent}$ is greater than a certain fraction ($\tau_1$) of the mean quantization error (*MQE*) of the new map.

$$MQE_i < \tau_1 \cdot qe_{parent} \qquad (4.5)$$

The criterion (4.5) ensures that the grown map will sufficiently describe the input vector of the parent node, but purposely does not ensure that every node within this grown map equally shares in the total quantization error of the map. The new nodes are initialized with the average of the weights of the surrounding nodes to ensure that map continuity and orientation is preserved. Growth is controlled by $\tau_1$. Decreasing $\tau_1$ provides larger, more complex maps that can reveal more about the pdf of the data, while increasing $\tau_1$ provides simplified maps for easier interpretation. There is a tradeoff between map complexity and ease of interpretation. A complex map better describes the complexity of the data set but is more difficult to interpret. A simple map understates the complexity of the data set but is easier to interpret.

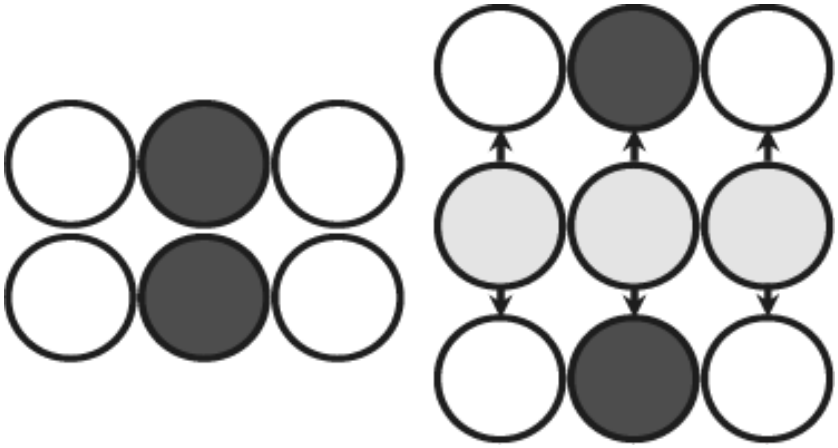

Figure 4.4. Illustration of growth of a self-organizing map. The two black nodes represent the node with the highest qe and the most different neighboring node. A new line of nodes is added to the grid to allow for the spread of the node possessing the highest qe.

**Hierarchical growth**

Following the initial training of the growing SOM, the quality of the training is evaluated to determine if further layers of maps are needed to adequately represent the data (Figure 4.5). The layer quantization error ($qe_{layer}$) is a measure of the overall heterogeneity of the input data mapped to a particular layer. The minimum quality of data representation for any particular node is a fraction ($\tau_2$) of the layer quantization error.

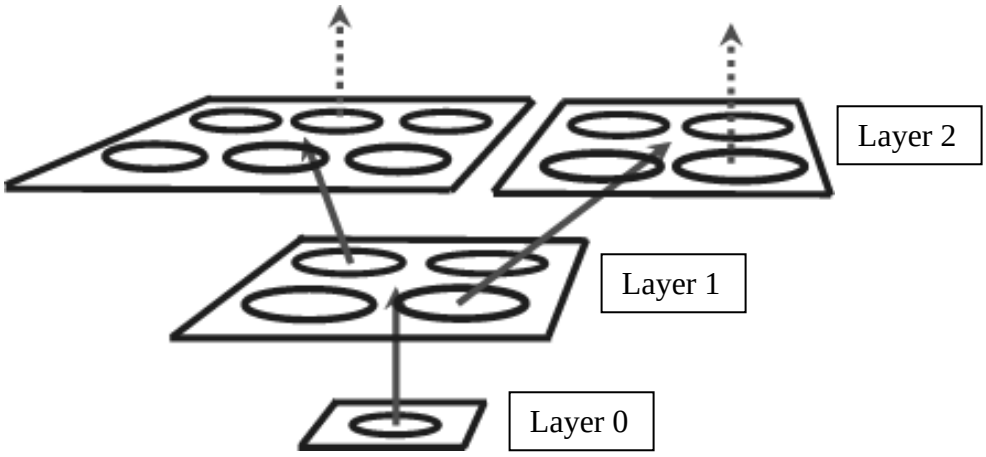


Figure 4.5. The hierarchical structure of the GHSOM. Nodes with poor fit quality (denoted by arrows) are grown into new maps.

The layer quantization error ($qe_{layer}$) is a measure of the overall dissimilarity of the input data mapped to a particular layer:

$$qe_{layer} = \sum_{i=1}^{N} qe_i \qquad (4.6)$$

While, the node quantization error ($qe_i$) gives the error between the n input data vectors that best matches the weight vector i

$$qe_i = \sum_{j=1}^{n} \left\| \vec{w}_i - \vec{x}_j \right\| \quad (4.7)$$

The minimum quality of data representation for any particular node is a fraction ($\tau_2$) of the layer quantization error:

$$qe_i < \tau_2 \cdot qe_{layer} \quad (4.8)$$

For any node that fails this quality check, a new 2x2 SOM layer is formed to represent the data of that node. The new node is initialized with the average of the weights of the nodes surrounding the failed node to ensure that the new layer preserves the same orientation as the parent layer. This new layer is undergoes the same processes of growing the grid and hierarchical growth as before until a previously prescribed level of quantization error and data quality is reached.

**Labeling and color**

In order for a SOM to be useful to the interpreter, the output nodes must be labeled. In supervised learning situations, labels are given to clusters through representative examples. Several supervised learning techniques are available for classifying and refining SOMs, including learning vector quantization (LVQ) (Kohonen, 1990). In an unsupervised case, where one lacks prior knowledge, labels are generated using the attributes that are most representative of the cluster or node. Thus, in unsupervised learning, a labeling strategy must be specified. In summary, labels can be assigned prior to the learning phase in the supervised case, whereas labels cannot be assigned in the unsupervised case until after the learning is completed.

Rauber and Merkl (1999) developed a labeling technique for SOMs based on the observation that output vectors take on the average appearance of the input vectors best matching that unit. Labels are assigned based on the attributes that are most closely fit, or best matched, by the output vectors. In their applications the data are discrete and were presented to the SOM in a binary format. In geophysical applications attributes values typically vary continuously and the variance of each attribute can be determined.

Building on the basic premise that the output vectors take on the average appearance of the input vectors best matching that node, I added a normalization step that takes into account differences in variance. The goodness of fit ($\chi_k$) of the $k^{th}$ attribute to the $i^{th}$ output weight is given by,

$$\chi_k = \frac{\sum_{j=1}^{N} \sqrt{(w_{i,k} - x^i{}_{j,k})^2}}{\sigma_k}, \qquad (4.9)$$

where $x^i$ are the vectors that best match output weight $i$, $N$ is the number of input vectors best matching the $i^{th}$ output weight vector, and $\sigma_k$ is the standard deviation of the $k^{th}$ attribute for the entire layer. If this merit function is less than one, it indicates that the output node $i$ represents a specific subset of attribute $k$ rather than fitting the entire population of that attribute for the layer. If the value is greater than one then the node shows no special adaption to a subset of that attribute. This merit function is nonparametric, or in other words it makes no assumption of the underlying probability density distribution function of the data. Attributes that have merit values less than one are ranked in ascending order, and the best ones characterized by a low rank ($\leq 5$ in these examples) are displayed on the trained nodes. Some nodes have less than five labels that indicates that fewer than five attributes have a goodness of fit of less than 1. No labels on a node indicate that this node does not represent any specific subset of the data. Also, with geophysical data, rather than binary data, we would like to know if the particular subset of attribute $k$ being represented by the output node $i$ is higher or lower than the average of that attribute for the layer ($\mu_k$), and by how much different it is, higher or lower, than normal. A useful measure of how different a particular weight is from the average of the layer for a particular attribute is given by

$$\varphi_k = \frac{w_{i,k} - \mu_k}{\sigma_k}. \qquad (4.10)$$

This calculation describes how many standard deviations from the mean of the attribute that an output weight represents. While this measure is strictly nonparametric, the "empirical rule" provides the user with rules of thumb that 99.7% of the data will be

within three standard deviations of the mean, 95% of the data will be within two standard deviation of the mean, and 68% of the data will be within one standard deviation of the mean, if the important assumption that the probability density function (pdf) of the data is normally distributed is true (Harnett and Murphy, 1980). However, the assumption of normally distributed data does not limit the user from making inferences with this measure in cases of non-normally distributed data. For example, if a significant portion of the input vectors are assigned to a node where the representative attribute is three standard deviations or more from the mean it indicates that it is highly probable that the distribution is not normal. These adaptations of the automatic labeling procedure of Dittenbach at al., (2002), for use with continuous geophysical data sets, provide useful insights into the patterns extracted by SOMs or GHSOMs. An example of an automatically labeled output node is shown in Figure 4.6.

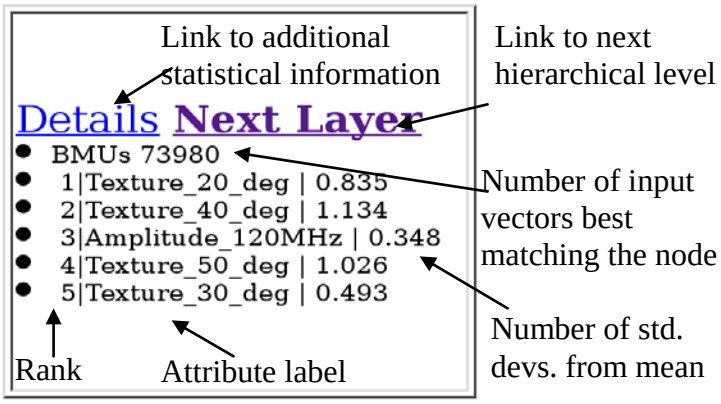


Figure 4.6. A node with automatically generated labels for the GHSOM. Each output node of the GHSOM is automatically labeled to provide the user with insight into the patterns represented by each node.

Following the training and labeling of the GHSOM, the cell of each input vector within the geophysical dataset is then assigned the color of the output node that it best matches. The result is that the geospatial distributions of the data can be visualized with

the GHSOM feature maps, thereby providing a key for interpretation. It is useful both in interpreting the SOM maps and in interpreting the geospatial representation of the pattern that the user has an intuitive representation of how closely related patterns are. Therefore, I ranked the output of nodes of the SOM by the distance from the node with the highest number of bmu's. The node with the highest number of BMU's is assigned blue and the node farthest from that node is labeled red (Figure 4.7). All other nodes are colored according to their distance ranking from the blue node using a linear RGB color map (blue to green to red). The result is that closely related nodes are colored similarly. In the geospatial display, sudden changes in color would indicate a significant discontinuity in the character of the subsurface, while continuous changes would be seen as gradual changes in color. This scheme provides the user with an intuitive representation of changes in patterns. This linear RGB color map scheme is most appropriate to data exhibiting two end members, which would be colored blue and red respectively. However, in cases of three or more end members within the data, two or more nodes may be unrelated yet have nearly identical distance from the node with the highest number of bmu’s. Thus, there is some ambiguity when using an RGB color scheme to represent a complex data set with more than two end members.

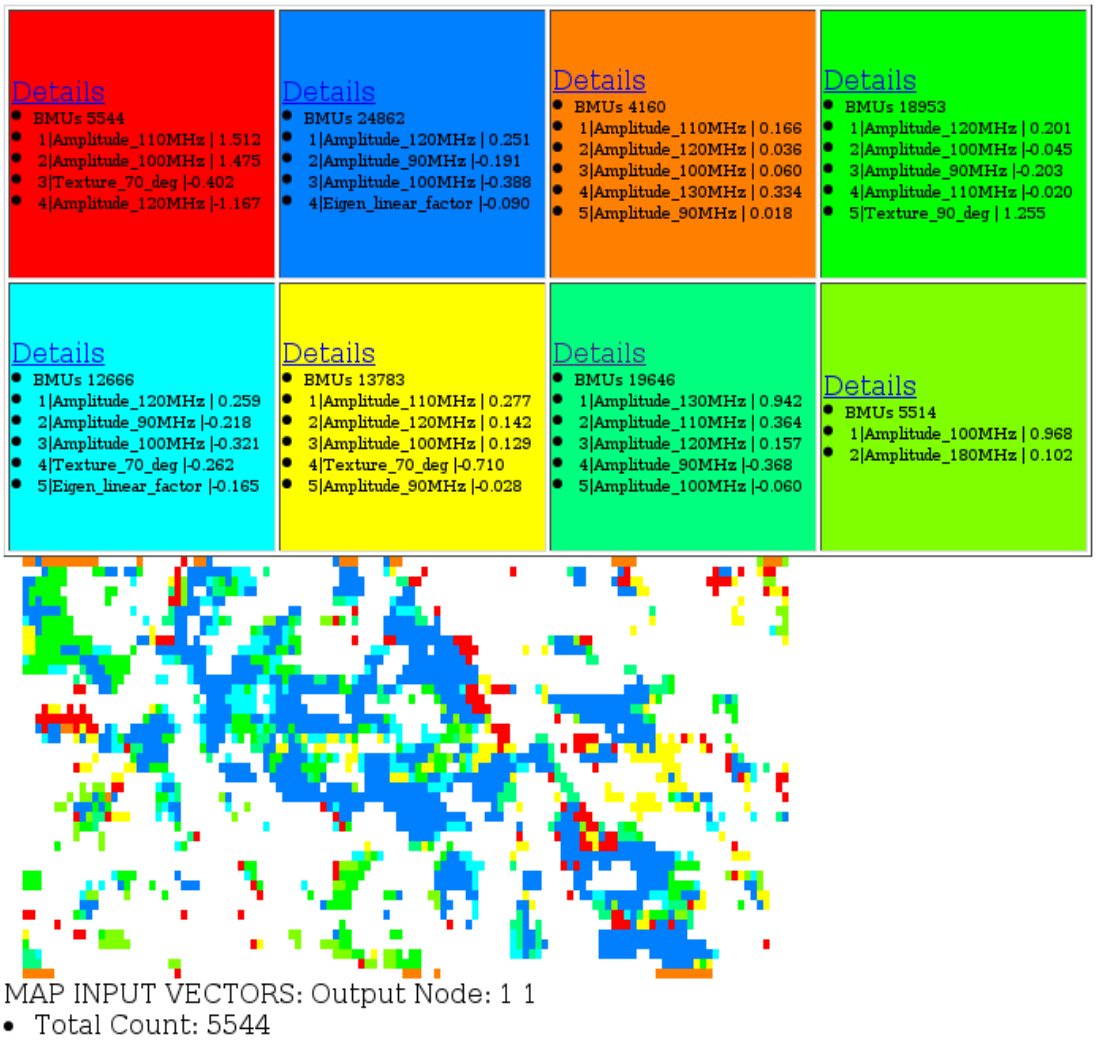


Figure 4.7. Screen capture of a GHSOM layer displaying the colored and labeled SOM (top), and a selected depth slice showing the geospatial distribution of the patterns (bottom).

## APPLICATION EXAMPLE: POLARIMETRIC GROUND PENETRATING RADAR

Three dimensional multicomponent GPR data were acquired from a shallow ecohydrologic experimentation plot situated on fractured and karst limestone of the Glen Rose formation, 45 km north of San Antonio, Texas, USA. The experiment plot measures14 m by 7 m and has a 2.5 m deep trench excavated on the downslope (2%

topographic gradient) boundary of the site. Additional coring and digging was prohibited because of the requirement that the integrity of the site be preserved for future experimentation. The geophysical objective is to determine the location and character of possible flow conduits with this fractured-karst limestone. Each component of the GPR data was acquired with a Sensors and Software Pulse Ekko 100 system using 200 MHz antennas. A fixed transmitter and receiver offset of 0.5 m was used, and each radar trace was stacked 64 times. The spacing between stations is 0.1 m in the in-line direction and 0.15 m in the cross-line direction. All data were identically processed and migrated (Sassen and Everett, 2009). Several geophysical attributes were extracted from the data to aid in the interpretation: coherency; instantaneous amplitude spectra; texture, and; polarization. While some of these attributes helped to distinguish the location of subsurface discontinuities, the attributes do not indicate whether a conduit is open, filled with soil, or contains roots. I show here that data mining of the numerous attributes with the GHSOM yields patterns that better distinguish the properties of these conduits.

**Preprocessing**

An important step in the preparation of the GPR data for data mining is reducing the dependence on instrument parameters, otherwise known as the spatiotemporal aspect (e.g. angle of incidence, response time, polarization, and source spectra). Standard geophysical processing steps, such as migration, can minimize the impact of spatiotemporal aspect on GPR and seismic data. In this example of ground penetrating radar, the polarization of the transmitter and receiver play an important role in shaping the response from subsurface features. To reduce polarization dependence, fully polarimetric data should be acquired and then reduced to the principle components, or eigenvalues, of the data. Polarimetric data can be described by the time-domain scattering matrix **S**(t) (Chen et al., 2001).

$$\overline{\overline{S}}(t) = \begin{bmatrix} S_{XX} & S_{XY} \\ S_{YX} & S_{YY} \end{bmatrix}; \qquad (4.11)$$

where $S_{ij}$ is the intensity of the electric field at the receiving antenna at time ($t$) of polarization direction ($\hat{a}_j$) backscattered from an arbitrary target illuminated by a transmitting antenna of polarization $\hat{a}_i$. The rotation of the **S** matrix sketches out an ellipse, where the primary axis and secondary axis are defined respectively by the 1st and 2nd eigenvalues ($\lambda$) and eigenvectors (Figure 4.8). The first eigenvalue $\lambda_1$ corresponds to the maximum of the electric field, as the antenna polarization is varied.

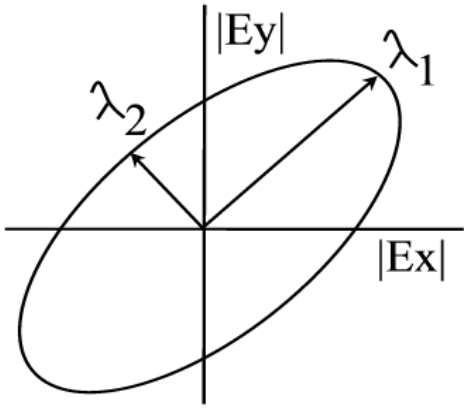


Figure 4.8. Illustration of the scattering ellipse for the electric field. The first and second eigenvalues correspond to the largest and smallest radius of the ellipse.

While the terms of the scattering matrix are dependent upon the coordinate basis of the survey, the eigenvalues and eigenvectors are invariant. Therefore, utilizing the first eigenvalue of the scattering matrix, one minimizes the response dependence to polarization. The amplitude at each time ($t$) from each of the components at each discrete position has been replaced with a single polarization invariant eigenvalue for extracting the attributes defined below.

## Attributes

In data mining and pattern recognition it is often desirable to reduce data complexity to the most salient points to improve the efficiency of training. In the example of GPR, important characteristics of the data include spectra, wavelet shape, the texture of the migrated data, and polarization. These characteristics can be extracted from the data with the use of attributes. The selection of the attributes also strongly influences the end result of the pattern clustering. The user must select attributes for analysis that apply the problem at hand. The four attributes that I chose are: (1) instantaneous amplitude spectra; (2) a textural attribute; (3) coherency, and; (4) the estimated linearity factor. Note that the four attributes are not orthogonal in the sense that the information contents of each attribute somewhat overlap. This is in contrast, for example, with using empirical orthogonal functions as attributes.

***Instantaneous amplitude spectra:*** The spectra are estimated with the discrete wavelet transform (DWT) using the Morelet Wavelet (Chopra and Marfurt, 2007) centered on a time slice of interest (Figure 4.9).

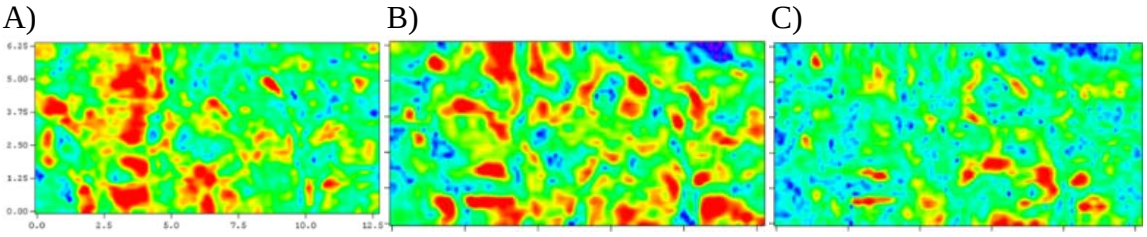


Figure 4.9. A time slice at 32 ns showing the instantaneous amplitude response of fractured limestone A) 90 MHz, B) 130MHz, and C) 180MHz. Reds indicate high amplitude response while blues represent low amplitude response. All slices are 12.7 x 6.3 meters.

The spectra are normalized by the maximum amplitude in each frequency bin to minimize the effect of the source spectra. Ten different frequencies spanning a range centered on the peak of the amplitude spectra (130 MHz) were used in the GHSOM training. The instantaneous amplitude spectra are useful in discriminating resonant features, such as thin layers, as some frequencies will constructively interfere and others destructively.

***Textural analysis:*** The R*-transform (Moysey et al., 2006) is used as the textural attribute (Figure 4.10). The R*-transform, based on the radon transform, provides a rotationally invariant measure of texture. The output of the R*-transform is the power for both the positive and negative component of each angle within the analysis window. This texture measure lends itself to intuitive understanding of the pattern. For example, the R*-transform of textures dominated by horizontal layers will have peak power at angles approaching 0º, vertical features will have peak power at angles approaching 90 º, and random textures will have flat distributions. Ten angle bins were selected from 0º to 90º at 10º intervals to create the texture attribute vector used in the training set. Figure 4.10 show the R*-transform for three different angle bins.

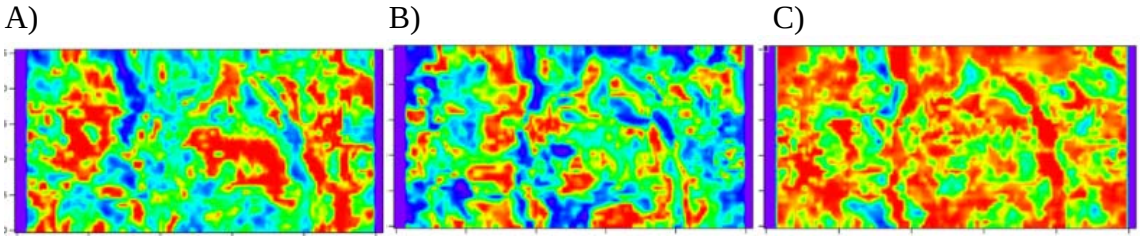


Figure 4.10. A time slice at 32 ns showing the textural features of fractured limestone A) horizontal, B) 40°, and C) vertical. Reds indicate high total amplitude for that dip angle response while blues represent low total amplitude. All slices are 12.7 x 6.3 meters.

***Estimated Linearity Factor (ELF):*** ELF (Chen et al., 2001) is a measure of the polarization dependence of a scatterer. ELF was calculated with the normalized difference between the time averaged primary $\lambda_1$ and secondary $\lambda_2$ eigenvalues of the scattering matrix.

$$ELF = \frac{\left|\left|\bar{\lambda}_1\right| - \left|\bar{\lambda}_2\right|\right|}{\left|\left|\bar{\lambda}_1\right| + \left|\bar{\lambda}_2\right|\right|} \qquad (4.12)$$

Features that are of high electromagnetic contrast and elongate, or linear, have high ELF scores approaching 1, such features include fractures faults, karst pipes, and veins, while features that are omni-directional scatterers approach 0 (Figure 4.11).

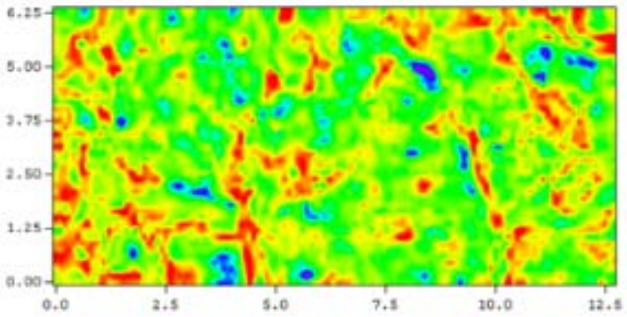


Figure 4.11. A time slice at 32 ns showing the estimated linearity factor (ELF) of fractured limestone. Reds indicate highly linear features and blues indicate omni-directional scatterers. Eight samples, or 3.2 ns of data, were averaged for each eigenvalue component.

***Polarimetric coherency:*** Polarimetric Coherency (Sassen and Everett, 2009) measures the similarity of wavelet shape within an analysis window. It is useful for delineating discontinuities such as fractures. The GPR polarimetric coherency is an extension of the standard seismic coherency attributes used in exploration geophysics. Areas of poor similarity trend towards a coherency score of 0, and areas of high similarity have coherency scores trending towards 1 (Figure 4.12).

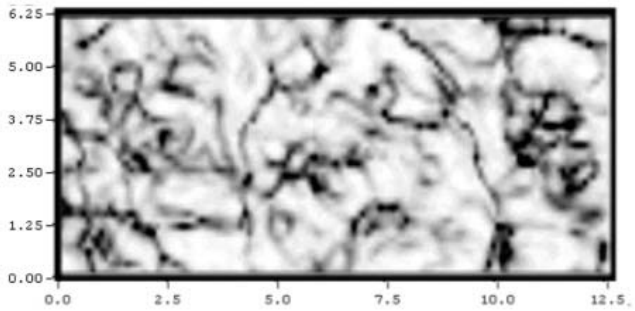


Figure 4.12. A time slice at 32 ns showing the polarimetric coherency attribute of fractured limestone, black indicates low coherency and white represents high coherency.

**Normalization**

Prior to application of the GHSOM it is important to normalize the attributes. Since the calculation of the quantization error is an $L_1$ merit function, the quantization error will scale linearly with the absolute value of the attribute. For example, if an attribute is normalized to scale from 0 to 1000 and the same attribute is rescaled to 0 to 1 the quantization error could be as much as 1000 times greater for the first normalization despite the identical misfit in terms of percentage. Scale disparity leads to an output vector that best fits the largest attribute at the expense of the smaller attributes. Therefore, to place equal weight amongst all of the attributes they are normalized so that the peak value is 1.0. Conversely, one may change the normalization to give greater or less weight to an attribute based on perceived importance or differences in error estimates. The spectral and texture attribute training sets used in this study are normalized

$$\frac{x_{i,j}}{x_{\max(i)}}; \qquad (4.13)$$

where $x_{max(i)}$ is the maximum value of each attribute $x_j$ of all the frequencies*(j)* at spatial location*(i)*. The scalar attributes of coherency and ELF were simply normalized by the global maxima for those respective attributes.

**Initial parameters of the GHSOM**

To test the GHSOM I used three different sets of the GPR attributes. The three sets are: (1) the instantaneous spectral amplitude vector; (2) the R*transform texture vector, and; (3) all four attributes, including the instantaneous spectral amplitude vector and the R*transform texture vector along with polarimetric coherency and ELF. The initial learning amplitude A(t) was set to 0.8 and decreased by training epoch (t) by,

$$A(t) = \frac{A(t-1)}{1.05}. \qquad (4.14)$$

The initial spatial influence σ was set to 0.6 and decreased with training epoch (*t*) by,

$$\sigma(t) = \frac{\sigma(t-1)}{1.05}. \qquad (4.15)$$

The threshold values controlling feature map growth ($\tau_1$) and hierarchical growth ($\tau_2$) are 0.1 and 0.05 respectively.

**UNSUPERVISED CLASSIFICATION RESULTS**

**Spectral attributes**

The first training set for the GHSOM consists of the instantaneous amplitude attribute, at 10 frequencies, extracted from the GPR data set. Layer 1 of the trained GHSOM is shown in figure 4.13. To properly interpret the result, the numerical values of the attributes contained in the node labels must be analyzed. The labels of several nodes of this GHSOM show significant differences from the mean attribute of the data set, especially nodes 4,1 (red) and 1,2 (yellow-green). Labels of node 4,1 indicate that this node represents spectral patterns with anomalously high amplitudes (+1.6 to +2.4 standard deviations from the mean) for the frequencies of 140Mhz and above. Conversely, the labels of node 1,2 indicates an amplitude peak at the lowest frequency, 90 MHz, (+2.0 standard deviations from the mean) and low amplitude spectra for higher frequencies (-2.0 for 120MHz). Note that these two nodes represent the two end

members of spectral distributions, and the GHSOM has organized these two nodes on opposite ends of the map.


Figure 4.13. The self-organized map of the instantaneous amplitude spectra attributes (Layer 1) is used as the key to interpret the geospatial output in figure 4.14.

In the visualization of the geospatial distribution of the patterns (Figure 4.14 A-C) it becomes apparent that areas of very low reflectivity seen in the migrated GPR images correlate to the patterns of low frequency dominated spectra of node 1,2 (yellow-green).

Figure 4.14. Illustration of the interpretation of soil filled cavities within the limestone. Areas of low reflectivity within a migrated GPR cross-section are outlined with dashed lines (A), the geospatial representation of the patterns from layer 1 of the GHSOM (B), the patterns (nodes 1,2 and 2,1) that correlate to the low reflectivity areas(C), the spectral content of the output weight vector shows that the output nodes associated with the low reflectivity area have spectra shifted to lower frequency(D) , and a photograph of the observation trench showing a soil filled cavity (E) that is aligned with the trend of the low amplitude area outlined on the far right side of (A).

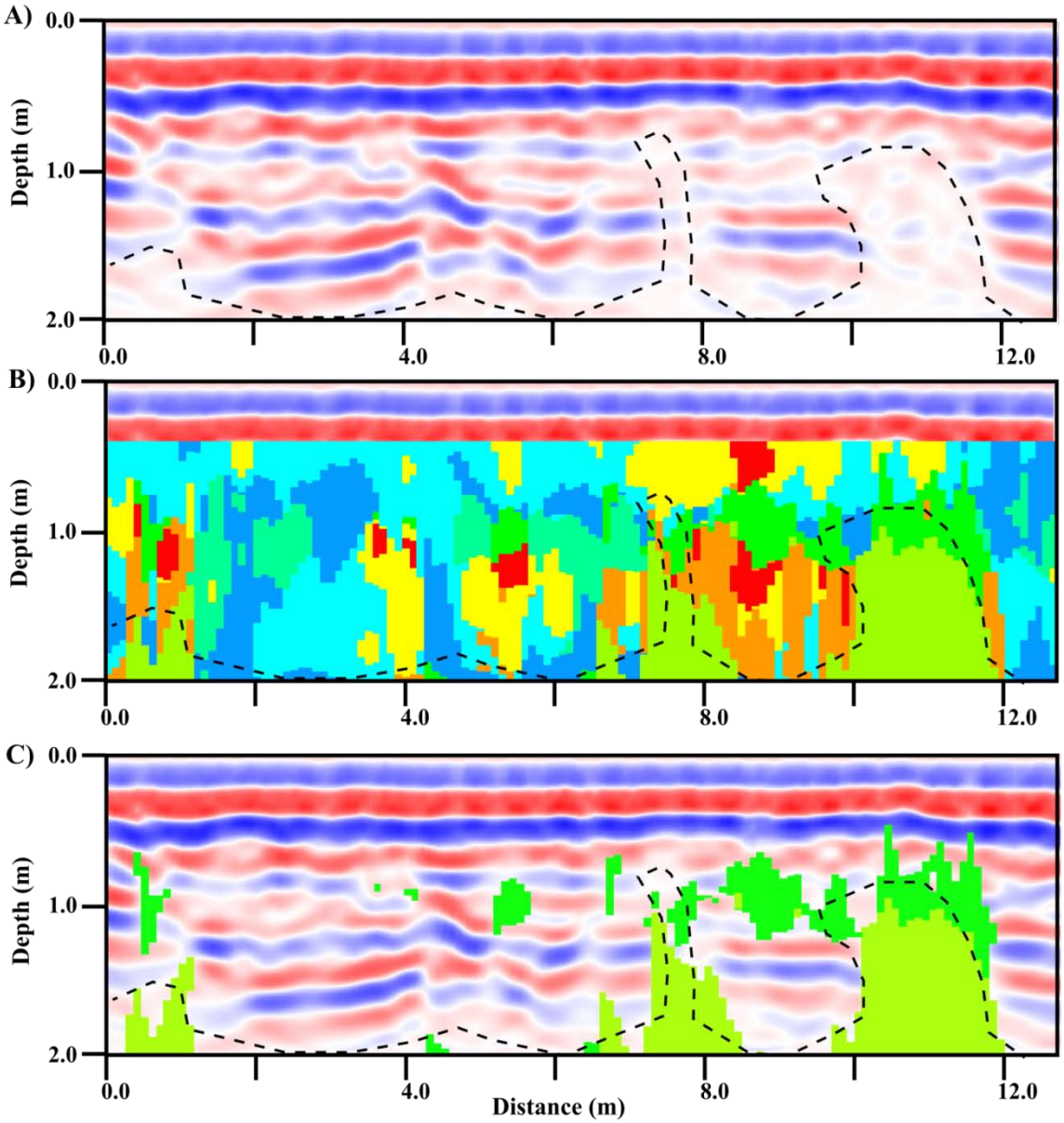
A)
B)
C)
Depth (m)
0.0
1.0
2.0
0.0
4.0
8.0
12.0
Distance (m)
D)
Spectra
Node 2,1
Mean
Node 1,2
Frequency MHz
E)
Soil Filled Cavity

Originally, these areas of very low reflectivity were thought to be highly fractured areas because of low coherency scores (darker areas of Figure 4.15-B), indicative of discontinuities in the GPR signal, observed within these areas. However, the shift in the frequency spectra towards a lower center frequency (Figure 4.14-D) suggests that frequency dependant attenuation and dispersion caused by conductive material such as wet soil or clay is leading to the observations of low reflectivity. This interpretation is backed by the observation that this pattern is collocated on low coherency areas of the subsurface (Figure 4.15-B) that have been interpreted as joints and karst features (Sassen and Everett, 2009), which would provide a pathway for the subsurface accumulation of soil. In addition, the trend of one area of this pattern aligns with a soil filled karst feature seen in the observation trench (Figure 4.14-E). This example has show how the SOM can lead to an improved hydrogeophysical interpretation of GPR data.

Estimation of soil volume contained within the shallow fractured/karst subsurface is very important in hydrologic and ecological studies for understanding carbon and nitrogen cycles, as well as potential water storage. Volume calculations of these patterns (Figure 4.15-C and D) are 5% of the total volume of the experimentation plot for node 1,2 and 7% for node 2,1. The anomalously high frequency pattern expressed by node 4,1 (Figure 4.13) could be caused by resonant features such as karst pipes or thin layers. However, in the visualization of the pattern, no obvious correlation exists between this high frequency pattern and interpretable features. More information is needed to understand what geologic feature these patterns indicate.

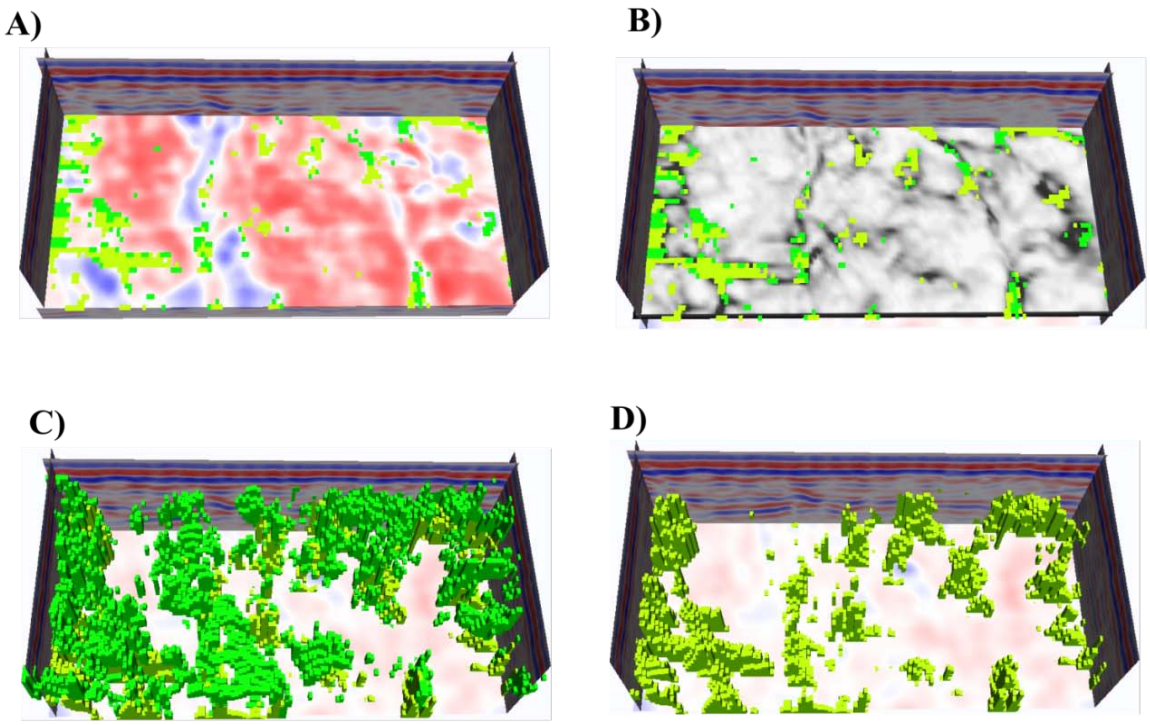


Figure 4.15. 3-D aspect views of the distribution of the patterns assigned to node 1,2 and node 2,1 (Figure 4.13) that are associated with the interpreted soil filled cavities (Figure 4.14). The spatial relationship between the patterns and an amplitude time slice at 1.5 meters depth (A), and a coherency attribute time slice at 1.5 meters depth (B). 3-D surface renderings of the patterns node 2,1 (D) and both nodes 2,1 and 1,2 together (C) superimposed on GPR fence diagrams.

## Texture attributes

In analysis of the textural attribute vector, several end members of texture become apparent. The size of the analysis window used in the textural analysis limits the use of this attribute to within areas more than half a window size from the spatial

edge of the data. As a result the first 8 and last 8 columns of each GPR line are given a null texture vector (Figure 4.17-B). The GHSOM positioned this pattern, node 2,3 (orange), at the far end of the map from the most common node, node 1,1 (blue). The labels of the node with the greatest number of bmu's, node 1,1 (blue), show that within this texture pattern the power from horizontally oriented features are slightly higher than the mean, with low energy in higher angled bins (Figure 4.16). This indicates that this node is representative of horizontally continuous features (Figure 4.17-D). This is interpreted as a pattern indicative of largely intact limestone that constitutes the bulk of the subsurface within the plot. This is supported by the observation that the geospatial distribution of this pattern is limited to areas of high coherency (light gray areas in Figure 4.18-A&C). The node that is most distant from node 1,1 in Euclidean space is node 2,2 (red). In the geospatial visualization of the patterns one can see that node 2,2 correlates to the low frequency spectra pattern from node 1,2 in figure 4.16 and low coherency areas in figure 4.18. Given the consistently high power in each of the normalized angle bins, this pattern is indicative of a random texture pattern, and is consistent with the textured expected from soil colluviums.

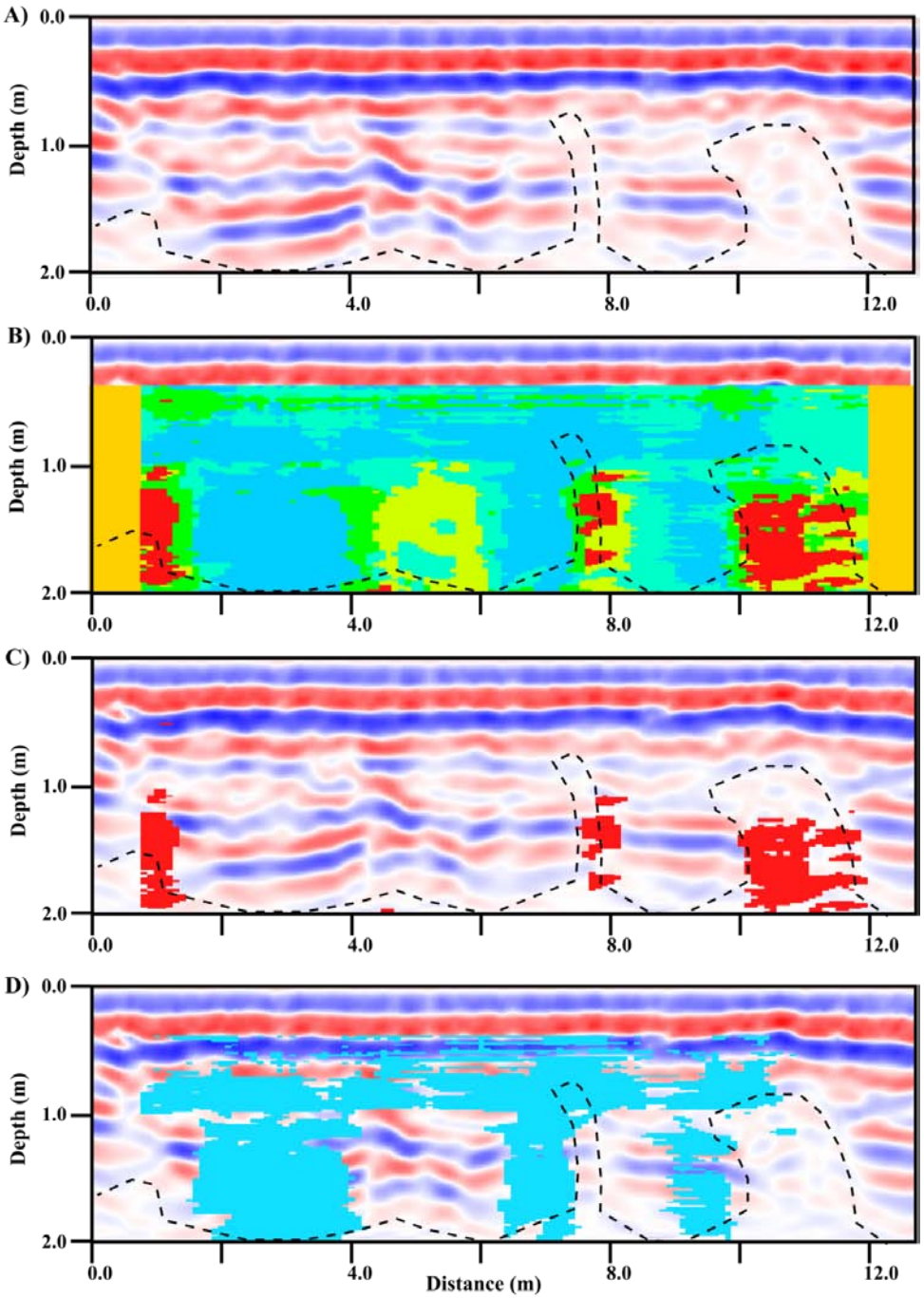


Figure 4.16. Interpretation of the GHSOM output for textural attributes. The identical areas of low reflectivity within a migrated GPR cross-section are outlined with dashed lines from figure 4.15 are shown in (A), the geospatial representation of the patterns from layer 1 of the GHSOM (see figure 4.18) are shown in (B), the distribution of pattern (nodes 2,2) that correlates to the low reflectivity areas (C), and the spatial distribution of the pattern from node 1,1 that is interpreted as intact limestone.

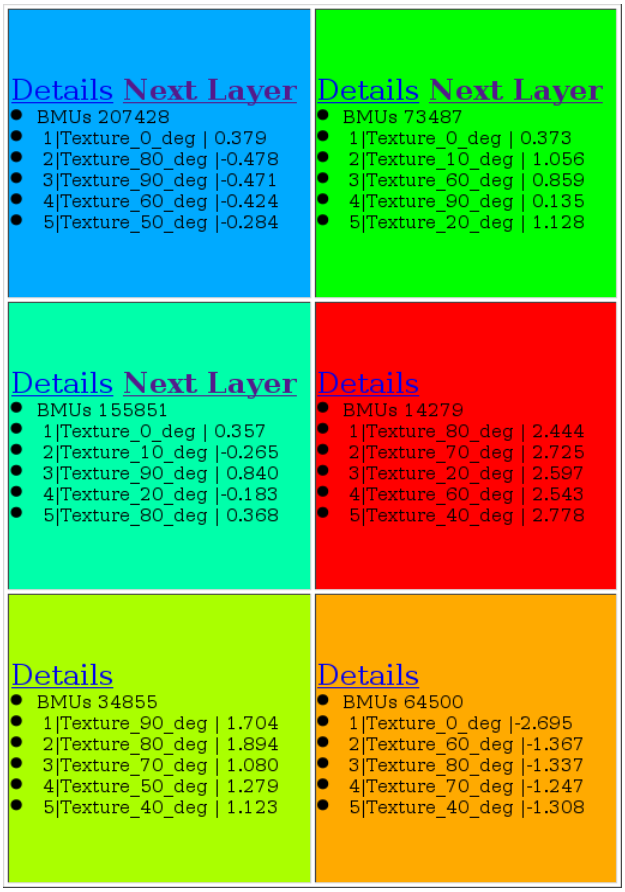


Figure 4.17. The self-organized map of the textural attributes (Layer 1) is used as the key to interpret the geospatial output in Figure 4.16.

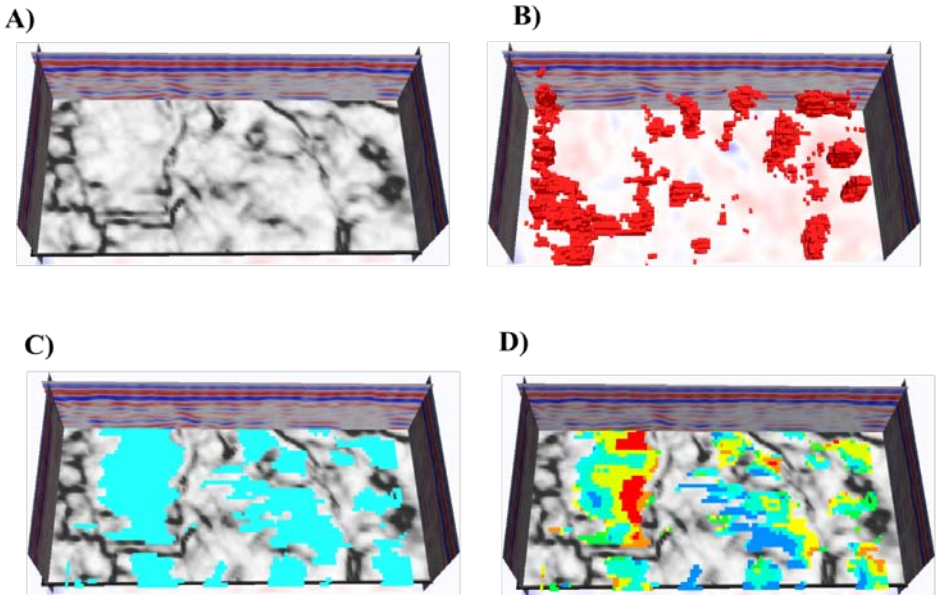


Figure 4.18. 3-D aspect views of the distribution of the patterns assigned to nodes 2,2 and node 1,1 (Figure 4.17) with a coherency time slice at 1.5 meters (A). The surface rendering of the textural pattern (node 2,2) is shown in (B). Figures C and D show a time slice of the intact limestone pattern (node 1,1 from figure 4.17) superimposed on the coherency time slice, where D shows the distribution of layer 2 pattern assignments seen in Figure 4.19.

In an attempt to gain more specific information on the state of the intact limestone I analyzed the second layer (Figure 4.19) grown from the bmu's of node 1,1 of figure 4.17.

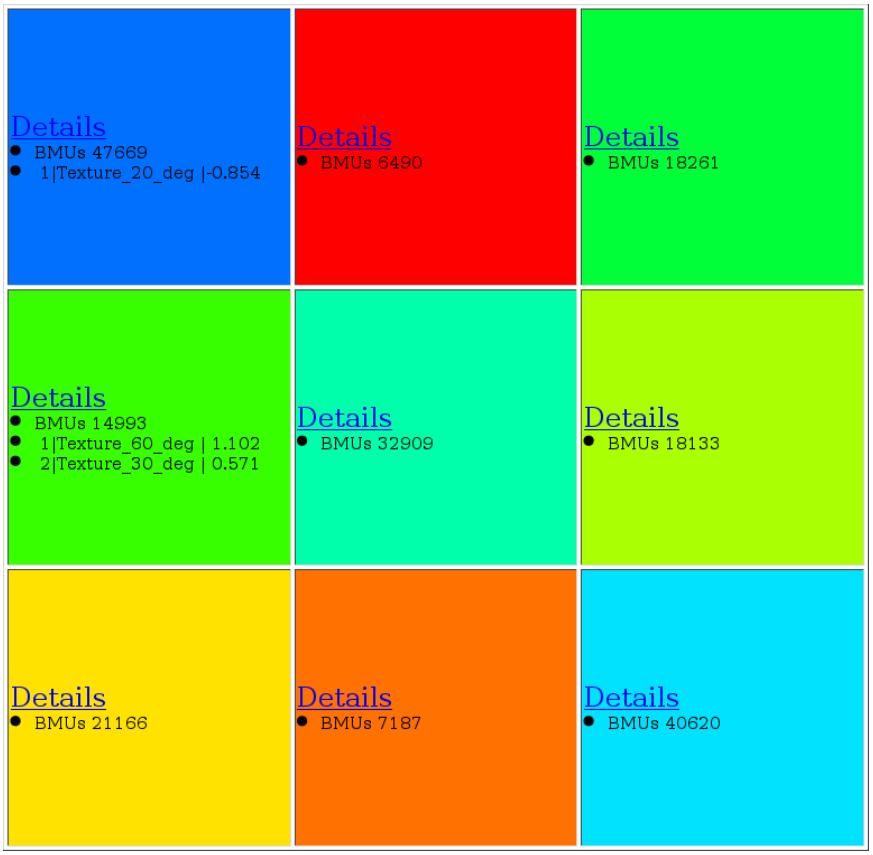


Figure 4.19. Shown here is the 2nd layer of the self-organized map of the instantaneous amplitude spectral attributes grown from the input patterns best matching the intact limestone pattern (node 1,1 of Figure 4.16), and is used as the key to aid in the interpretation of the geospatial output in figure 4.18-D.

The automatic labels for the feature map of the second layer show that very few nodes have labels (Figure 4.19), indicating that the nodes do not represent specific subsets of the data, but largely represent the entire population of the layer. Plus, the colors assigned to the geospatial output (Figure 4.18-D) change gradually from blue to red. The labels and geospatial data suggests that divisions within the second layer are mostly attributable continuous variation in texture. This gradual variation of patterns was typical of most of the higher layers of the GHSOM outputs. This subtle level of detail seen in the higher levels of the GHSOM is much more than what I need to meet my objective.

**Combined attributes**

The final application of the GHSOM utilized the amplitude attributes, the textural attributes, coherency and ELF together as the training set (Figure 4.20). Many of the same patterns emerge from the combined set of attributes. The labels output for some nodes are nearly identical to the previous outputs from the other training sets. Again, with this training set we see a distinct pattern with its amplitude spectra shifted towards low frequencies, node 1,2 – red, that correlates with the spatial distribution of the pattern interpreted as soil fill within the limestone (Figure 4.21). Another distinctive pattern, node 3,1 (yellow-green), is distinguished by the very high frequency components, that possible indicates resonant features, and was also seen within the first training set (Figure 4.13). In some cases, the combination of all of the attributes together is more informative than the previous sets. The labels of nodes 2,2 and 1,1 (Figure 4.20) indicate that these nodes are representative inputs with higher than average coherency (+0.422 to +0.327 standard deviations from the mean), texture dominated by horizontal features (0 bin +0.368 to +0.399 std. dev. from mean), and the spectral peaks close to mean of the data. These defining attributes are consistent with intact limestone that constitutes the bulk of the background that is also identified in the previous examples. The success from using the larger input set in the training in identifying the same patterns demonstrates the effectiveness of the GHSOM and automatic labeling procedure in identifying significant clusters and their defining attributes even with combinations of disparate attributes.

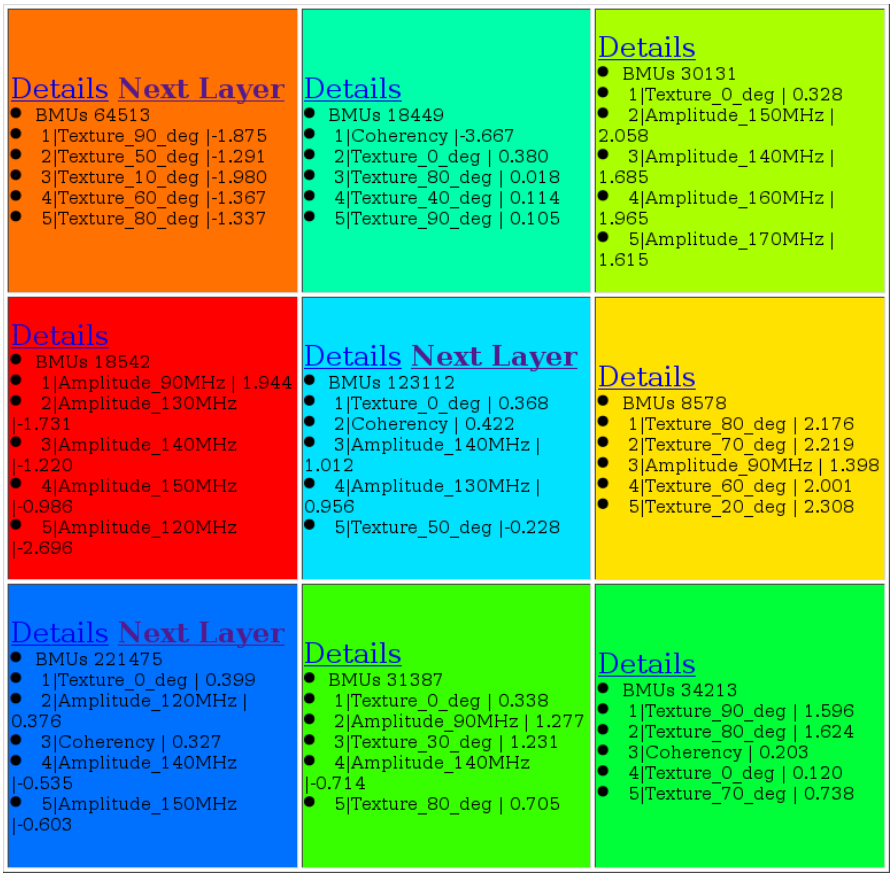


Figure 4.20. The SOM feature map generated from input vectors consisting of the instantaneous spectral amplitude attributes, the textural attributes, coherency and ELF. This feature map is used as the key to interpret the geospatial output in figure 4.21.

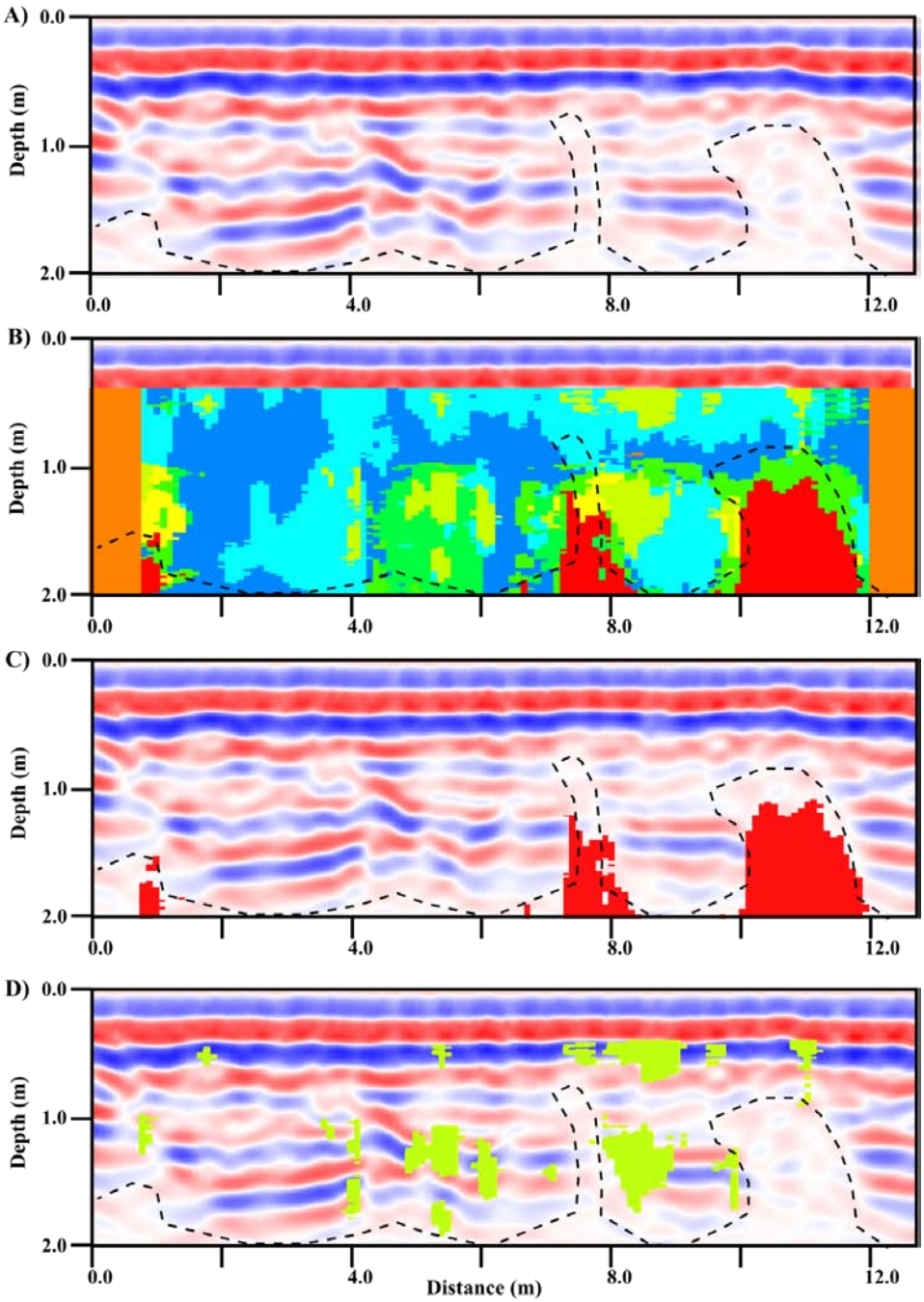


Figure 4.21. Interpretation of the GHSOM output for the combination of all attributes. The identical areas of low reflectivity within a migrated GPR cross-section are outlined with dashed lines from figures 4.14 and 4.17 are shown in (A), the geospatial representation of the patterns from layer 1 of the GHSOM (see figure 4.20) are shown in (B), the distribution of pattern (nodes 1,2) that correlates to the low reflectivity areas (C), and the spatial distribution of the pattern from node 3,1 indicating areas of anomalous spectral shift towards high frequencies(D).

## DISCUSSION AND CONCLUSIONS

The DM/KDD process in this example has led to the discovery of patterns indicative of the soils within the fractured/ karst limestone. The labeled GHSOMs provide a means of exploring data in a structured manner that allows the use of geologic and geophysical based knowledge to discover new information. Through the various examples I have demonstrated that the GHSOM can produce a useful key to help in the interpretation of data where little or no information exists. It also shows the potential for providing an estimate of the total volume of soil within the experimentation plot. However, because direct samples are lacking these interpretations suffer from significant uncertainty. Using the geospatial distributions of the patterns I can efficiently design subsurface coring surveys to test these interpretations, and to place error estimates on the volume of the soils within the karst with minimal impact to the experimentation site.

While the main focus of this paper is on the unsupervised learning case of data mining and knowledge discovery, the SOM also has significant advantages once independent confirmation of subsurface features becomes available and one can move towards supervised learning. Kohonen (1990) provides specific supervised learning methods, known as learning vector quantization (LVQ), that work within the context of the self-organizing map. In the LVQ process, nodes of an SOM best matching sets of representative examples define class centroids, and class memberships are defined as a function of a node's vector space distance from the various class centroids. Kohonen, 1990, showed that LVQ class boundaries closely follow Bayesian decision boundaries, where inclusion within the class indicates that an input vector most likely resembles the centroid of that class than any other centroid. Also, the capability of the SOM to represent the probability density function (pdf) of a cluster becomes useful. Bayesian statistics can then be used to suggest the probability of misclassifying features, thus providing estimates of risk.

The flexibility and adaptability of the GHSOM are important characteristics for geophysical applications. Geophysical data does not lend itself to simple clustering,

because most geologic features vary continuously from one end-member to the next and also because of omnipresent noise. Additionally, the data mining procedure must always be tailored to the end goal of the user. These issues suggest an iterative process where the interpreter can select different levels of hierarchy of adjust the weights and thresholds to get the needed level of detail without being negatively affected by excessive information. The ability to adjust data weights and threshold values prior to training leads to a certain level of supervision by the end user. While minimizing the need for user input and reliance on prior knowledge are important characteristics of the GHSOM, in many cases this limited supervision of the training process is vital to the end goal. In addition to the ability to define, or redefine, classes within the SOM with LVQ, an existing GHSOM may also adapt to new environments by additional training with new input vectors. Thus, it accumulates knowledge from each survey and exploits that knowledge to perform increasingly better in a wider domain of situations

# CHAPTER V
# DISCUSSION AND CONCLUSIONS

This research has been highly successful in pushing the envelope of knowledge in the area of nondestructive detection and characterization of fractures and karst features. The research has provided three distinct paths for dealing with GPR data 1) image enhancement for detecting discontinuities with polarimetric coherency, 2) quantitative interpretation of fractures with full-waveform inversion of transmission data, and 3) pattern identification with the growing hierarchical self-organizing map (GHSOM). These three distinctive methods complement each other by refining the interpretation of the results from the ecohydrology test site when used together.

The polarimetric coherency algorithm has minimized the bias of antenna polarization in the detection of subsurface discontinuities. Plus, it has been shown to be clearly better than existing methods. While the method was demonstrated on fractures, it has applications to any situation where subsurface discontinuities exist. The polarimetric coherency results were vital in providing the necessary constraint for the inversion results, and it also aided in the evaluation of the patterns extracted with the GHSOMs. The most significant caveat of the method is the requirement of three coordinated antenna polarization to construct the scattering matrix that significantly increases data acquisition time. Therefore, the method is best used in areas where targets of interest have strong electromagnetic contrasts and/or have large length to width ratios.

The full-waveform inversion technique for GPR transmission profiles shows promise in quantitatively determining the aperture and electromagnetic properties of thin layer features. Plus, the acquisition of the transmission data could be accomplished in a variety of ways including transmission from boreholes, cliff faces, and trenches, and wide angle reflection surveys. The method has been validated on idealized synthetic data. The ease of the acquisition of the data of the simplicity of the model makes it very

time efficient compared to other methods. However, the simplicity of the forward model limits the application of this method to specific conditions. The model is built around a plane wave approximation, which is only valid in the far field of the GPR source (>3 wavelengths from the source). Also, it assumes idealized geometry of the fracture as a thin parallel sided plate embedded in the limestone. Real fractures are rarely perfectly straight and often vary in aperture and have asperities. Also, the tests on the synthetic data show that it can only perform reliably on thin layers with a thickness greater than 5% of the dominant wavelength of the source. Because of these limitations the inversion technique is probably best suited to an auxiliary role for other inversion methods. It could be used as a method of initializing or constraining inversion methods based on more general models such as finite difference time domain or finite element that have prohibitively long computation times without some guidance.

The application of the GHSOM to the GPR data is the first known example of an application of this data mining technique to geophysical data. While most geophysical applications of the closely related self-organizing maps focus on the identification of the number of clusters, this application has focused on extracting previously undiscovered patterns within the data without any representative examples from direct samples. Also, a new automatic labeling procedure is introduced for dealing with continuous data sets typical of geophysical data. Using the GHSOM in the role of data mining and knowledge discovery, distinct patterns indicative of soil filled cavities within the limestone were discovered. This allowed for determination of the location and volume of soil within the subsurface. This is very useful information for determining the role of these deep soils in the ecology of *Juniperus ashei* and the water and carbon cycles in this environment. The GHSOM results could be further enhanced with some direct samples so that uncertainty levels could be estimated and class boundaries could be refined.

One of the primary problems with the development of detection and characterization methods at the Honey Creek experimentation site is the inability to dig or drill into the plot to directly verify the interpretation of the results. The integrity of the site was to be preserved for future experimentation. Without direct sampling it is not

possible to place an uncertainty on the interpretations. This is a classic common problem throughout geophysics. Geophysical exploration of the deep interior of planets is a prime example of a research problem that lacks the aid of any direct sampling. In near surface geophysics, where direct sampling is often possible, issues of safety, cost or socially sensitive areas are common obstacles to direct verification of interpretations. However, in the development of new exploration methods some form of independent verification should be sought whenever possible. In part, the ability to verify interpretations is a defining characteristic of near surface geophysics, which separates it from other geophysical disciplines that require inference and extrapolation. Despite this weakness, this research has provided the framework for others to further push the envelope of knowledge for noninvasive methods of detecting and characterizing fractured and karsted rock bodies.

In addition to the contribution to geophysics these methods also improved knowledge of the relationship between the subsurface and ecology. The geophysics provided evidence that *Juniperus ashei* occupies fractures and karst features within the limestone of the test plot. These fractures and karst features provide preferential pathways through which water can quickly infiltrate deep into the subsurface beyond the shallow soil. The previous observation from this test site shows that *Juniperus ashei* redirects a significant portion of intercepted rainfall directly to its roots through stemflow, and that the *Juniperus ashei* litter is strongly hydrophobic and prevents infiltration into the shallow soil. These plot scale conclusions imply important processes that may affect the entire region. *Juniperus ashei* is well adapted to access water within fractured rock while limiting water to shallow rooted plants competing for limited water in the hydrogeologic setting of the Edwards Aquifer region. This study also suggests that the brush may enhance regional groundwater recharge by focusing water into conduits where it can bypass the soil and evapotranspiration. The difficulties in characterizing the subsurface at the experimentation site are what drove the development of new geophysical methods.

# REFERENCES

Alford, R. M., 1986, Shear data in the presence of azimuthal anisotropy: 56th Ann. Internat. Mtg., Soc. Expl. Geophys., Expanded Abstracts, 476–479.

Azcarraga, A.P., H-M. Hsieh, S.L Pan, and R. Setiono, 2005, Extracting salient dimensions for automatic SOM labeling, IEEE Trans on Systems, Man, and Cybernetics – Part C: Applications and Reviews, **35**, 595-600.

Bahorich, M., and S. Farmer, 1995, 3-D seismic discontinuity for faults and stratigraphic features: The coherency cube: The Leading Edge, **14**, 1053-1058.

Bauer, K., G. Pratt, C. Haberland, and M. Weber, 2008, Neural network analysis of crosshole tomographic images: The seismic signature of gas hydrate bearing sediments in the Mackenzie Delta (NW Canada): Geophysical Research Letters, **35**, L19306,1-6.

Bauters, T.W.J., D.A. DiCarlo, T.S. Steenhuis, and J.Y. Parlang, 1998, Preferential flow in water-repellent sands: Soil Science Society of America Journal, **62**, 1185-1190.

Bear, J., C-F. Tsang, and G. De Marsily, 1993, Flow and contaminant transport in fractured rock: Academic Press, San Diego, CA.

Benavides, A., M.E. Everett, and C. Pierce, Jr., 2009, Unexploded ordnance discrimination using time-domain electromagnetic induction and self-organizing maps: Stoch Environ Res Risk Assess, **23**, 169-179.

Bezdek, J.C., C. Coray, R. Gunderson, and J. Watson, 1981, Detection and characterization of cluster substructure: Fuzzy c-Lines: SIAM Journal of Applied Mathematics, **40**, 339-357.

Boerner, W-M., W.L. Yan, A.Q. Xi, 1990, Basic equations of radar polarimetry and its solutions: the characteristic radar polarization states for the coherent and partially polarized cases, *in* R.A. Chipman and J.W. Morris, eds., Polarimetry: Radar, Infrared, Visible, Ultraviolet, and X-Ray: Proceedings SPIE, **1314**, 16-79.

Bosch, J.M., and J.D. Hewlett, 1982, A review of catchment experiments to determine the effect of vegatation changes on water yield and evapotranspiration: Journal of Hydrology, **55**, 3-23.

Bradford, J.H., and J.C. Deeds, 2006, Ground-penetrating radar theory and application of thin-bed offset-dependent reflectivity: Geophysics, **71**, no. 3, K47-K57.

Castro de Matos, M., P.L. Manassi Osorio, P.R. Schroeder Johann, 2007, Unsupervised seismic facies analysis using wavelet transform and self-organizing maps: Geophysics, **72**, no 1, P9-P21.

Chen, C-C., M.B. Higgins, K. O'Neill, and R. Detsch, 2001, Ultrawide-bandwidth fully-polarimetric ground penetrating radar classification of subsurface unexploded ordnance: IEEE Transactions on Geoscience and Remote Sensing, **39**, 1221-1230.

Chopra, S., and K.J. Marfurt, 2007, Seismic attributes for prospect identification and reservoir characterization: SEG geophysical developments series; no. 11, S.J. Hill, ed., Society of Exploration Geophysicist, Tulsa, OK.

Coleou, T., M. Poupn, and K. Azbel, 2003, Unsupervised seismic facies classification: A review and comparison of techniques and implementation: The Leading Edge, **22**, 942-953.

Collins, E.W., 1987, Characterization of fractures in limestones, northern segment of the Edwards Aquifer and Balcones Fault Zone, Central Texas: GCAGS Transactions, **37**, 43-54.

Collins, E.W., 1995, Structural framework of the Edwards Aquifer, Balcones Fault Zone, Central Texas: GCAGS Transactions, **45**, 135-142.

Dasgupta, S., B.P. Mohanty, and J.M. Kohne, 2006, Impacts of juniper vegetation and karst geology on subsurface flow processes in the Edwards Plateau, Texas: Vadose Zone Journal, **5**, 1076–1085.

Deparis, J. and S. Garambois, 2007, Inversion of dispersive APVO GPR curves: A thin-layer approach for fracture characterization on a vertical cliff: Proceedings of the 4$^{th}$ International Workshop on Advanced GPR, Naples, Italy, 49-55.

Dittenbach, M., A. Rauber, and D. Merkl, 2002, Uncovering hierarchical structure in data using the growing hierarchical self-organizing map: Neurocomputing, **48**, 199-216.

Dugas,W.A., R.A. Hicks, and P. Wright, 1998, Effect of removal of *Juniperus ashei* on evapotranspiration and runoff in the Seco Creek watershed: Water Resources Research, **34**, 1499-1506.

Edwards Aquifer Authority (EAA) Aquifer science research program plan 2006-2011, Report No. 06-03, 2006.

Ernst, J. R., 2007, Full-waveform inversion of crosshole radar data based on 2-D finite-difference time-domain solutions of Maxwell's equations: IEEE Transactions on Geoscience and Remote Sensing, **45**, 2807-2827.

Essenreiter, R., M. Karrenbach, and S. Treitel, 2001, Identification and classification of multiple reflections with self-organizing maps: Geophysical Prospecting, **49**, 341-352.

Ferrill, D.A., D.W. Sims, D.J. Waiting, A.P. Morris, N.M. Franklin, and A.L. Schultz, 2004, Structual framework of the Edwards Aquifer recharge zone in south-central Texas: GSA Bulletin, **116**, 407-418.

Fritzke, B., 1994, Growing Cell Structures – A self-organizing network for unsupervised and supervised learning: Neural Networks, **7**, 1441-1460.

Fritzke, B., 1995, Growing Grid – A self-organizing network with constant neighborhood range and adaptation strength: Neural Processing Letters, **2**, 9-13.

Gazdag, J., 1978, Wave equation migration with the phase-shift method: Geophysics, **43**, 68-89.

Gersztenkorn, A., and K.J. Marfurt, 1996, Eigenstructure based coherence computations: 66$^{th}$ Annual International Meeting: SEG, Expanded Abstracts, 328-331.

Giannopoulos, 2003, GPRMax 2D/3D user's manual, Giannopoulos, Edinburgh, UK.

Grasmueck, M., R. Weger, and H. Horstmeyer, 2005, Full-resolution GPR imaging: Geophysics, **70**, no 1, K12-K19.

Gregoire, C., and F. Hollender, 2004, Discontinuity characterization by the inversion of the spectral content of ground-penetrating radar (GPR) reflections- Application of the Jonscher model: Geophysics, **69**, 1141-1424.

Harnett, D.L., and J.L. Murphy, 1980, Introductory statistical analysis, Addison-Wesley, Reading, MA.

Herrero, J., A. Valencia, J. Dopazo, 2001, A hierarchical unsupervised growing neural network for clustering gene expression patterns: Bioinformatics, **17**, 126-136.

Hill, D.A., 1988, Electromagnetic scattering by buried objects of low contrast: IEEE Transactions on Geoscience and Remote Sensing, **26**, 195-203.

Hollender, F., and S. Tillard, 1998, Modeling ground-penetrating radar wave propagation and reflection with the Jonscher parameterization: Geophysics, **63**, 1933-1942.

Houghton, R.A., J.L. Hackler, and K.T. Lawrence, 1999, The U.S. carbon budget: Contributions from land-use change: Science, **285**, 574-578.

Huxman, T.E., B.P. Wilcox, D.D. Breshears, S.L. Scott, K.A. Snyder, E.E. Small, K. Hultine, W.T. Pockman, and R.B. Jackson, 2005, Ecohydrologic implications of woody plant encroachment: Ecology, **86**, 308-309.

Iizuka, K., 2002, Elements of photonics, Volume 1: In free space and special media: John Wiley and Sons, New York, p. 664.

Irving, J.D., and R.J. Knight, 2003, Removal of wavelet dispersion from ground-penetrating radar data: Geophysics: **68**, 960-970.

Jackson, R.B., J.L. Banner, E.G. Jobbagy, W.T. Pockman, and D.H. Wall, 2002, Ecosystem carbon loss with woody plant invasion of grasslands: Nature, **418**, 623-626.

Jardine, N., and R. Sibson, 1968, The construction of hierarchic and non-hierarchic classifications: The Computer Journal, **11**, 177-184.

Jeannin, M., S. Garambois, C. Gregoire, and D. Jongmans, 2006, Multiconfiguration GPR measurements for geometric fracture characterization in limestone cliffs

(Alps): Geophysics, **71**, no 3, B85-B92.

Jerri, A.J. 1977. The Shannon sampling theorem—its various extensions and applications: a tutorial review: Proc. IEEE, **65**, 1565—1596.

Jia, H.T., T. Takenaka, and T. Tanaka, 2002, Time-domain inverse scattering method for cross-borehole georadar data: IEEE Trans. Geoscience Remote Sensing, **40**, 1640-1647.

Jiao, Y., G.A. McMechan, and E. Perrinelli, 2000, In situ 2-D and 3-D measurements of radiation patterns of half-wave dipole GPR antennas: Journal of Applied Geophysics, **43**, 69-89.

Klose, C.D., 2006, Self-organizing maps for geoscientific data analysis: geological interpretation of multidimensional geophysical data: Comput Geosci, **10**, 265-277.

Kofman, L., A. Ronon, and S. Frydman, 2006, Detection of model voids by identifying reverberation phenomena in GPR records: Journal of Applied Geophysics, **59**, 284-299.

Kohonen, T., 1990, The Self-Organizing Map, Proceed of the IEEE, **78**, 1464-1480.

Kruse, S., M. Grasmueck, M. Weiss, and D. Viggiano, 2006, Sinkhole structure imaging in covered karst terrain: Geophysical Reseach Letters, **33**, L16405

Kuroda, S., M. Takeuchi, and H.J. Kim, 2005, Full waveform inversion algorithm for interpreting cross-borehole GPR data: 75$^{th}$ Annual International Meeting, SEG, Expanded Abstracts, 1176-1179.

Lambot, S., E.C. Slob, I. van den Bosch, B. Stockbrockx B., Scheers and M. Vanclooster, 2004, Estimation of soil electric properties from monostatic ground-penetrating radar signal inversion in the frequency domain: Water Resources Research, **40**, W04205.

Lehmann, F., D.E. Boerner, K. Holliger, and A.G. Green, 2000, Multicomponent georadar data: Some important implications for data acquisition and processing: Geophysics, **65**, 1542-1552.

MacQueen, J., 1969, Some methods for classification and analysis of multivariate observations, Proceeding of the Fifth Berkeley Symposium, 281-290.

Mancini, E.A., and R.W. Scott, 2006, Sequence Stratigraphy of Comanchean Cretaceous outcrop strata of Northest and South-Central Texas: Implications for enhanced petroleum exploration: GCAGS Transactions, **56**, 539-550.

Marfurt, K.J., V. Sudhaker, A. Gersztenkorn, K.D. Crawford, and S.E. Nissen, 1999, Coherency calculations in the presence of structural dip: Geophysics, **64**, 102-111.

Marriquin, I.D., J-J. Brault, and B.S. Hart, 2009, A visual data-mining methodology for seismic facies analysis: Part 1- Testing and comparison with other unsupervised clustering methods: Geophysics, **74**, no 1, P1-P11.

McClymont, A.F., A.G. Green, R. Streich, H. Horstmeyer, J. Tronicke, D.C. Nobes, J. Pettinga, J. Campbell, and R, Langridge, 2008, Visualization of active faults using geometric attributes of 3D GPR data: An example from the Alpine Fault Zone, New Zealand: Geophysics, **73**, no. 2, B11-B23.

Mitra, S., Pal, S.K., and P. Mitra, 2002, Data mining in soft computing framework: a survey: IEEE Trans on Neural Networks, **13**, 3-14.

Moysey, S., R.J. Knight, and H.M. Jol, 2006, Texture-based classification of ground-penetrating radar images: Geophysics, **71**, no. 6, K111-K118.

Olenick, K.L., J.R. Conner, R.N. Wilkins, U.P. Kreuter, and W.T. Hamilton, 2004, Economic implications of brush treatments to improve water yield: J. Rang Manage, **57**, 337-345.

Pacala, S.W., G.C. Hurtt, D. Baker, P. Peylin, R.A. Houghton, R.A. Birdsey, L. Heath, E.T. Sundquist, R.F. Stallard, P. Ciais, P. Moorcroft, J.P. Caspersen, E. Shevliakoca, B. Moore, G. Kohlmaier, E. Holland, M. Gloor, M.E. Harmon, S-M. Fan, J.L. Samiento, C.L. Goodale, D. Schimel, and C.B. Field, 2001, Consistent

land- and atmosphere-based U.S. carbon sink estimates: Science, **292**, 2316-2320.

Piccolo, A., R. Spaccini, G. Haberhauer, M.H. and Gerzabek, 1999, Increased sequestration of organic carbon in soil by hydrophobic protection: Naturwissenschaften, **86**, 496–499.

Pujol, J., 2007, The solution of nonlinear inverse problems and the Levenberg-Marquardt method: Geophysics, **72**, no**.** 4, W1-W16.

Radzevicius, S.J., and J.J. Daniels, 2000, Ground penetrating radar polarization and scattering from cylinders: Journal of Applied Geophysics, **45**, 111-125.

Rauber, A., and D. Merkl, 1999, Automatic labeling of self-organizing maps: Making a treasure-map reveal its secrets, Pacific-Asia Conference on Knowledge Discovery and Data Mining, 228-237.

Rauber, A., D. Merkl, and M. Dittenback, 2002, The growing hierarchical self-organizing map: exploratory analysis of high-dimensional data: IEEE Trans. on Neural Networks, **13**, 1331-1341.

Roberts, R.L., 1994, Analysis and theoretical modeling of GPR polarization data: Ph.D. Dissertation, The Ohio State University, Columbus.

Roberts, R.L., and J.J. Daniels, 1996, Analysis of GPR polarization phenomena: Journal of Environmental and Engineering Geophysics, **1**, 139-157.

Sassen, D.S., 2008, A coherency attributes algorithm for polarimetric ground penetration radar (GPR): 78th Annual International Meeting, SEG, Expanded Abstracts.

Sassen, D.S., and Everett, M.E., 2007, 3-D multicomponent GPR to characterize shallow subsurface flow paths in an epikarst limestone, Edwards Plateau, Texas: 77th Annual International Meeting, SEG, Expanded Abstracts, 1197-1201.

Sassen, D.S., and Everett, M.E., 2009, 3D Polarimetric GPR coherency attributes and full-waveform inversion of transmission data for characterization of fractured rock: Geophysics, **74**, no. 3, J23-J34.

Sassen, D.S., M.E. Everett, and C.L. Munster, 2009, Ecohydrogeophysics at the Edwards

Aquifer: Insights from polarimetric ground-penetrating radar: Near Surface Geophysics, **7**, 427-438.

Seol, S.J., J.-K. Kim, Y. Song, and S.-H. Chung, 2001, Finding the strike direction of fractures using GPR: Geophysical Prospecting, **49**, 200-308.

Sharma, P.V., 1997, Environmental and engineering geophysics: Cambridge University Press, Cambridge, UK.

Steenhuis, T.S., A.G. Hunt, J.Y. Parlange, and R.P. Ewing, 2005, Assessment of the application of percolation theory to a water repellent soil: Australian Journal of Soil Research, **43**, 357-360.

Stevens, K.M., G.S. Lodha, A.L. Holloway, and N.M. Soonawala, 1995, The application of ground penetrating radar for mapping fractures in plutonic rocks within the Whiteshell Research Area, Pinawa, Manitoba, Canada: Journal of Applied Geophysics, **33**, 125-141.

Stratton, J.A., 1941, Electromagnetic theory: McGraw-Hill, New York.

Streich, R., and J. van der Kruk, 2007, Accurate imaging of multicomponent GPR data based on exact radiation patterns: IEEE Transactions on Geosciences and remote sensing, **45**, 93-103.

Talley, J., G.S. Baker, M.W. Becker, and N. Beyrle, 2005, Four dimensional mapping of tracer channelization in subhorizontal bedrock features using surface ground penetrating radar: Geophysical Research Letters, **32**, 1-4.

Tallini, M., D. Gasbarri, D. Ranalli, and M. Scozzafava, 2006, Investigating epikarst using low-frequency GPR: Example from the Gran Sasso range (Central Italy): Bulletin of Engineering Geology and the Environment, **65**, 435-443.

Taucer, P.I., C. Munster, B. Wilcox, M. Owens, and B.P. Mohanty, 2008, Large-scale rainfall simulation experiments on juniper rangelands: Transactions of the ASABE, **51**, 1951-1961.

Taucer, P.I., C.L. Munster, B.P. Wilcox, B. Shade, S. Dasgupta, M.K. Owens, and B.

Mohanty, 2006, Large plot tracing of subsurface flow in the Edwards Aquifer epikarst, *in* Beck, B.F., Editor, Sinkholes and the engineering and environmental impacts of karst: ASCE Geotech.Sp. Publ., no. 144, 207-215.

Taylor, S.C., C. Hall, W.D. Wolf, and M.A. Wilson, 2000, Partial wetting in capillary liquid absorption by limestones: Journal of Colloid and Interface Science, **224**, 351-357.

Tsoflias, G.P., and Hoch A., 2006, Investigating multi-polarization GPR wave transmission through thin layers: Implications for vertical fracture characterization: Geophysical Research Letters, **33,** L20401.

Tsoflias, G.P., J-P. Van Gestel, P.L. Stoffa, D.D. Blankenship, and M. Sen, 2004, Vertical fracture detection by exploiting the polarization properties of ground-penetrating radar signals: Geophysics, **69**, 803-810.

Ultsch, A., 1993, Self-organizing neural networks for visualization and classification, *in* Opitz, O., B. Lausen and R. Klar, Editors, Information and classification-concepts, methods and applications: Springer Verlag, Berlin, 307–313.

Van Auken, O. W., 2000, Shrub invasions of North American semiarid grasslands: Annual Review of Ecological Systems, **31**, 197-215.

van der Kruk, J., S.A. Arcone, and L. Liu, 2007, Fundamental and higher mode inversion of dispersed GPR waves propagating in an ice layer: IEEE Transactions on Geoscience and Remote Sensing, **45**, 2483-2491.

van der Kruk, J., R. Steich, and A.G. Green, 2006, Properties of surface waveguides derived from separate and joint inversion of dispersive TE and TM GPR data: Geophysics, **71**, no. 1, K19-K29.

Van Gestel, J-P., and P.L. Stoffa, 2001, Application of Alford rotation to ground-penetrating radar data: Geophysics, **66**, 1781-1792.

von Hipple, A.R., 1966, Dielectrics and waves: The MIT Press, Cambridge, MA.

Widess, M.B., 1973, How thin is a thin bed?: Geophysics, **38**, 1176-1180.

Wilcox, B.P., 2002, Shrub control and stream flow on rangelands: A process based viewpoint: J. Range Management, **55**, 318-326.

Wilcox, B.P., Y. Huang, and J.W. Walker, 2008, Long-term trends in streamflow from semiarid rangelands: Uncovering drivers of change: Global Change Biology, **14**, 1676-1689.

# APPENDIX
# THE ALTERNATING DIRECTION IMPLICIT FINITE-DIFFERENCE TIME-DOMAIN METHOD

## INTRODUCTION

The simulation of ground penetrating radar for complicated subsurface geometries requires numerical methods, such as the finite-difference time-domain (FDTD) method. The traditional FDTD technique for modeling electromagnetics (EM) suffers from numerical dispersion unless time steps are kept below the Courant-Friedrichs-Lewy (CFL) stability limit. The accurate modeling of electromagnetic scattering by complex targets requires a refined grid, subgrids, or conformal grids that can significantly increase computation time (Holland, 1993). A relatively recent adaptation of the FDTD technique, the alternating direction implicit (ADI)-FDTD, uses implicit equations that help to cancel numerical dispersion and allow for unconditionally stable modeling of EM and therefore is not bound by the CFL stability limit. Here a review of the methods used to construct an ADI-FDTD algorithm for the simulation of GPR is presented. Also, validation and examples of simulations of the completed model are provided.

## REVIEW OF FDTD METHODS

The FDTD method has become the preferred method for GPR simulation. A small sample of FDTD applied to GPR include: Lampe and Holliger (2003), Lampe et al. (2005), and Roberts and Daniels (1997) who all demonstrated FDTD techniques for accurate representations of realistic GPR antennas over a half-space, and Wang and Tripp (1996) who demonstrated the utility of the FDTD for modeling the GPR response to 3D heterogeneous media.

FDTD modeling of electromagnetics seeks the time and space evolution of the electric and magnetic field through numerical approximation to Maxwell's equations.

$$-\nabla x\vec{E} = \frac{\partial}{\partial t}\mu\vec{H} \qquad (1)$$

$$\nabla x\vec{H} = \sigma\vec{E} + \frac{\partial}{\partial t}\varepsilon\vec{E} + \vec{J}_s \qquad (2)$$

The classical means of solving these equations was introduced by Yee, (1966). The Yee method is an explicit forward stepping method that utilizes an accurate centered-difference approximation. Yee's most important contribution is the Yee Cell (Figure A-1), which allows for the implementation of the centered difference scheme for the spatial derivatives of the coupled electric (**E)** and magnetic fields (**H)**. . In time the **H** field components are half a step ahead of the known **E** fields, thus the time derivative is updated with accurate midpoint approximations. The Yee cell is also utilized in the ADI-FDTD scheme presented here

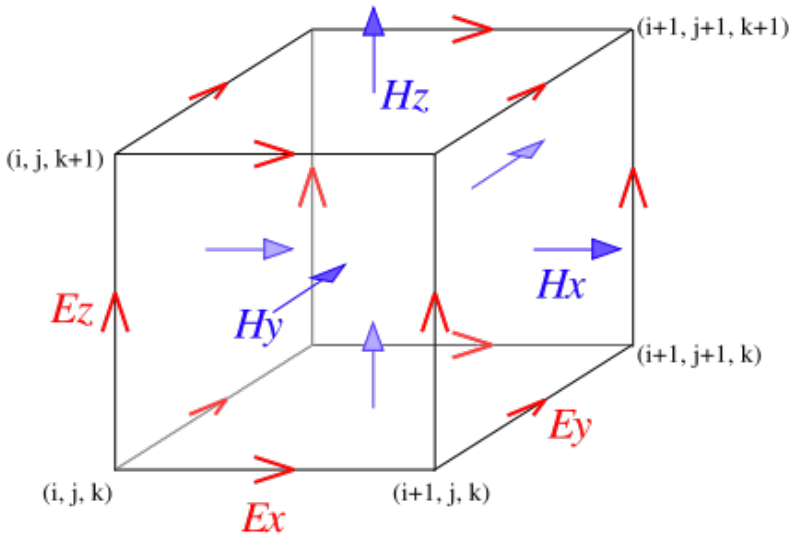


Figure A-1. The Yee unit cell. All electromagnetic field component are evaluated at separate staggered positions.

Stability analysis of the FDTD method has revealed that time steps $\Delta t$ of the FDTD model must be kept smaller than the Courant-Friedrichs-Lewy (CFL) stability limit:

$$\Delta t \leq \frac{1}{c\sqrt{\frac{1}{\Delta x^2}+\frac{1}{\Delta y^2}+\frac{1}{\Delta z^2}}}, \qquad (3)$$

where $\Delta x$ ,$\Delta y$ and, $\Delta z$ are the spatial step size and c is the maximum velocity in the computational domain. Time steps larger than the CFL stability limit will result in numerical dispersion. The quandary presented by stability limit is that as one decreases the spatial increment to increase model accuracy for irregular or small features the number of time steps must increase significantly. To overcome this problem alternative discritization techniques such as the Crank-Nicholson scheme can be used.

The Crank-Nicholson scheme of finite-difference modeling is commonly used in diffusion equations. The Crank-Nicholson scheme takes advantage of the fact that a forward-time stepping FDTD and backward-time stepping FDTD both suffer from numerical dispersion, but with the key difference that the two have opposing dispersion. The great insight of the Crank-Nicholson scheme is that if one averages together both the forward in time centered in space approximation and the backward in time centered in space approximation, the two opposite dispersion terms cancel each other out making the resulting discritization unconditionally stable. However, in practice the Crank-Nicholson scheme for FDTD is too computationally expensive. Implementation of this scheme requires the inversion of very large and spars matrices. The ADI-FDTD method also overcomes problems of numerical dispersion, but with significant computational savings.

The ADI-FDTD algorithm was introduced simultaneously by Namiki, (1999) and Zheng and Zhang, (1999). The ADI-FDTD scheme combines a forward in time centered in space approximation with a backward in time centered in space approximation, which cancels the opposite numerical dispersion effects, resulting in a discritization that is unconditionally stable. However, the ADI-FDTD technique can allow for significant

decreases in computation time compared to the FDTD. The ADI-FDTD method breaks the implicit equations into two substeps in time that alternate in the spatial direction of update. This difference changes the problem of solving the implicit equations from the expensive task of inverting a large spare matrix to the trivial task of inverting a tridiagonal matrix. While the ADI-FDTD has obvious advantages, it has limitations in accuracy for simulations run at time steps significantly greater than the CFL.

Staker et al., 2003, demonstrated that the traditional FDTD method is actually more accurate than the ADI-FDTD method when both are run at the CFL limit. However, Staker et al., 2003, identified a class of problems that the ADI-FDTD method provides a means to decrease simulation execution time while maintaining accuracy. They identified that the ADI-FDTD method is best suited for problems that either require a refined grid or an irregular grid. In geophysics one is often presented the task of simulating a highly heterogeneous subsurface at fine scales that requires refined or irregular grids. Thus, the ADI-FDTD method is well suited for geophysical modeling.

## THE ADI-FDTD ALGORITHM

The ADI-FDTD algorithm was introduced by Namiki, (1999) and Zheng and Zhang, (1999). As in the traditional 3D-FDTD technique, the Ampere and Faraday equations (equations 1 and 2) are decomposed into six scalar equations in Cartesians coordinates and then discritized using Yee's method (Equations 5-10). The ADI technique breaks the time-step into two sub-steps. In the first step the electric field (**E**) is calculated for a nonphysical half-time step *(n to n+1/2)* (Equations 5-7). An electric field component depends on two orthogonal magnetic field components, one that is based on time *(n)* where the field is already known and the other that is based on the unknown time *(n+1/2)*.

$$Ex^{n+1/2}_{(i+1/2,j,k)} = Ca_{(i+1/2,j,k)} \cdot Ex^{n}_{(i+1/2,j,k)} + Cb_{(i+1/2,j,k)} \cdot [\{Hz^{n}_{(i+1/2,j+1/2,k)} - Hz^{n}_{(i+1/2,j-1/2,k)}\}/\Delta y(i) - \{Hy^{n+1/2}_{(i+1/2,j,k+1/2)} - Hy^{n+1/2}_{(i+1/2,j,k-1/2)}\}/\Delta z(k)] \quad (5)$$

$$Ey^{n+1/2}_{(i,j+1/2,k)} = Ca_{(i,j+1/2,k)} \cdot Ey^{n}_{(i,j+1/2,k)} + Cb_{(i,j+1/2,k)} \cdot [\{Hx^{n}_{(i,j+1/2,k+1/2)} - Hx^{n}_{(i,j+1/2,k-1/2)}\}/\Delta z(k) - \{Hz^{n+1/2}_{(i+1/2,j+1/2,k)} - Hz^{n+1/2}_{(i-1/2,j+1/2,k)}\}/\Delta x(i)] \quad (6)$$

$$Ez^{n+1/2}_{(i,j,k+1/2)} = Ca_{(i,j,k+1/2)} \cdot Ez^{n}_{(i,j,k+1/2)} + Cb_{(i,j,k+1/2)} \cdot [\{Hy^{n}_{(i+1/2,j,k+1/2)} - Hy^{n}_{(i-1/2,j,k+1/2)}\}/\Delta x(i) - \{Hx^{n+1/2}_{(i,j+1/2,k+1/2)} - Hx^{n+1/2}_{(i,j-1/2,k+1/2)}\}/\Delta y(j)] \quad (7)$$

$$Hx^{n+1/2}_{(i,j+1/2,k+1/2)} = Hx^{n}_{(i,j+1/2,k+1/2)} + Db_{(i,j+1/2,k+1/2)} \cdot [\{Ey^{n}_{(i,j+1/2,k+1)} - Ey^{n}_{(i,j+1/2,k)}\}/\Delta z(k) - \{Ez^{n+1/2}_{(i,j+1,k+1/2)} - Ez^{n+1/2}_{(i,j,k+1/2)}\}/\Delta y(j)] \quad (8)$$

$$Hy^{n+1/2}_{(i+1/2,j,k+1/2)} = Hy^{n}_{(i+1/2,j,k+1/2)} + Db_{(i+1/2,j,k+1/2)} \cdot [\{Ez^{n}_{(i+1,j,k+1/2)} - Ez^{n}_{(i,j,k+1/2)}\}/\Delta x(i) - \{Ex^{n+1/2}_{(i+1/2,j,k+1)} - Ex^{n+1/2}_{(i+1/2,j,k)}\}/\Delta z(k)] \quad (9)$$

$$Hz^{n+1/2}_{(i+1/2,j+1/2,k)} = Hz^{n}_{(i+1/2,j+1/2,k)} + Db_{(i+1/2,j+1/2,k)} \cdot [\{Ex^{n}_{(i+1/2,j+1,k)} - Ex^{n}_{(i+1/2,j,k)}\}/\Delta y(j) - \{Ey^{n+1/2}_{(i+1,j+1/2,k)} - Ey^{n+1/2}_{(i,j+1/2,k)}\}/\Delta x(i)] \quad (10)$$

Substitutions are made to remove the unknown terms from the right hand side and the equation is rearranged to isolate the unknown electric field component terms on the left hand side (e.g. 10 into 5). This set of implicit equations (e.g. the Ey component in equation 11) can be efficiently solved using tri-diagonal solvers that update the field along one spatial axis that is orthogonal to the field component being updated (e.g. z-axis). After solving for all three **E** field components for the non-physical half step (*n+1/2*), the **H** fields at the half step (*n+1/2*) can be calculated explicitly (Equations 8-10).

$$\begin{aligned} &-\alpha 2 Ey^{n+1/2}_{(i-1,j+1/2,k)} + \beta 2 Ey^{n+1/2}_{(i,j+1/2,k)} - \gamma 2 Ey^{n+1/2}_{(i+1,j+1/2,k)} = \\ &p2 \cdot Ey^{n}_{(i,j+1/2,k)} + \{Hx^{n}_{(i,j+1/2,k+1/2)} - Hx^{n}_{(i,j+1/2,k-1/2)}\}/\Delta z(k) \\ &-(Hz^{n}_{(i+1/2,j+1/2,k)} - Hz^{n}_{(i-1/2,j+1/2,k)})/\Delta x(i) \\ &-r2 \cdot [\{Ex^{n}_{(i+1/2,j+1,k)} - Ex^{n}_{(i+1/2,j,k)}\}/\Delta y(j)\Delta x(i) \\ &+q2 \cdot [\{Ex^{n}_{(i-1/2,j+1,k)} - Ex^{n}_{(i-1/2,j,k)}\}/\Delta y(j)\Delta x(i) \end{aligned} \quad (11)$$

where,

$$\alpha 2 = Db_{(i-1/2,\, j+1/2,\, k)} / \Delta x^2(i)$$
$$\beta 2 = 1/Cb_{(i,\, j+1/2,\, k)} + \alpha 2 + \gamma 2$$
$$\gamma 2 = Db_{(i+1/2,\, j+1/2,\, k)} / \Delta x^2(i)$$
$$p2 = Ca / Cb_{(i,\, j+1/2,\, k)}$$
$$q2 = Db_{(i-1/2,\, j+1/2,\, k)}$$
$$r2 = Db_{(i+1/2,\, j+1/2,\, k)}$$

$$Ca_{(i,j,k)} = \frac{4\varepsilon(i,\, j,\, k) - \sigma(i,\, j,\, k)\Delta t}{4\varepsilon(i,\, j,\, k) + \sigma(i,\, j,\, k)\Delta t}$$

$$Cb_{(i,j,k)} = \frac{2\Delta t}{4\varepsilon(i,\, j,\, k) + \sigma(i,\, j,\, k)\Delta t}$$

$$Db_{(i,j,k)} = \frac{\Delta t}{2\mu(i,\, j,\, k)}$$

The second sub-step *(n+1/2 to n+1)* is nearly identical with a few important differences. The second sub-step utilizes the already calculated half-step components to complete the time-step. It is important to point out that the in the second half step, the unknown magnetic field component on the right hand side is now the component that was previously treated as a known in equations (5 through 10). Again, substitutions are made to remove the unknown terms from the right hand side and the equation is rearranged to isolate the unknown electric field component terms on the left hand side. These equations are solved implicitly, but in the alternate direction (e.g. equation 11 would be solved in x-direction). After solving for all the **E** field components, the **H** field can be calculated explicitly. The newly updated components are saved into memory and treated as previously known values *(n)* in the next iteration. While each full time step iteration is approximately two times longer than the traditional FDTD technique, the saving made by using larger time steps can decrease computation time significantly. In Namiki's (2000) original paper on the 3-D ADI-FDTD scheme for one example, it was reported that computation time is 24% of the traditional FDTD method while retaining accuracy.

**Boundary conditions**

The ADI-FDTD scheme updates Maxwell's equations accurately through an open homogenous computational domain and for changes in electromagnetic properties within the domain, when boundaries fall along the model grid. However, for boundaries that do not conform to the model grid, such as curved or dipping surfaces, one must ensure continuity of the tangential electric and magnetic field components (Yeh, 1993) and minimize the problems of a staircase boundaries (Holland, 1993). Also, special attention must be paid to terminating the model space to prevent reflections from the boundaries of the model space, and to minimize the size of the computational space by using absorbing boundary conditions (ABC).

Currently, the most accurate method of terminating model boundaries for the ADI-FDTD method are based on the perfectly matched layer (PML) technique of (Berenger 1994 and 1996). This method splits the magnetic and electric fields in a layer near the boundary into two nonphysical fields that provide the freedom to perfectly match the impedance of any field within the normal computational domain. It also allows for arbitrary assignment of electric and magnetic conductivity within the PML to attenuate the incident fields while not producing any reflections. This method was adapted to the ADI-FDTD simultaneously by Liu and Gedney, (2000), and Chen et al., (2000). Unfortunately, the split field requires a doubling of the sets of implicit equations need to solve for the PML conditions within the ADI scheme. Older, less accurate, but more time efficient methods are preferred when ultimate accuracy is not the main concern. To terminate the boundaries of the simulation domain I used 1$^{st}$ order Mur absorbing boundary condition (Mur, 1981), which has been adapted to allow implementation in the implicit update equations,

$$Ey^{n+1/2}_{(i-1,\,j+1/2,\,k)} - \frac{c\Delta t - 2\Delta x}{c\Delta t + 2\Delta x} Ey^{n+1/2}_{(i,\,j+1/2,\,k)} = Ey^{n}_{(i,\,j+1/2,\,k)} - \frac{c\Delta t - 2\Delta x}{c\Delta t + 2\Delta x} Ey^{n}_{(i-1,\,j+1/2,\,k)} \qquad (12)$$

where, *c* is the velocity of the media at the boundary. The Mur ABC is a discrete version of the 1-D plane wave solution to the Helmholtz equation for electromagnetics. It is most accurate for waves approaching at normal incidence. The Mur ABC is used in this model because of the computational simplicity. Field components that not tangential with a computational boundary are terminated with perfect electric conductors (PEC) or perfect magnetic conductors (PMC), where the field on the other side of the boundary goes to zero.

For dealing with curved or dipping interfaces that do not conform to a regular grid several steps can be taken to minimize staircase inaccuracies. One method of ensuring continuity across nonconforming boundaries is an average of the electromagnetic properties from either side of the boundary (Dey and Mittra, 1999). Thus, instead of having update equations with a step, or discontinuity, in electromagnetic properties within the update equations, the averaged properties provide a continuous ramp between the two sides. While this does not explicitly account for the boundary conditions derived from Maxwell's equations (e.g. Yeh, 1993), it has been shown to be an accurate approximation (Dey and Mittra, 1999; Christ, et al., 2006). In this implementation of the ADI-FDTD code, the conformal mesh technique of Dey and Mittra, (1999) is used.

**The source**

One of the many advantages of the FDTD method is the ease of implementing the current source. Simple half-wavelength dipole GPR antennas, such as those used in the PulseEkko 100 system, can be adequately represented by an infinitesimal dipole source (Demarest, 1998). The finite difference equivalent of an infinitesimal source is the excitation of a single discrete cell volume. More sophisticated source geometries may be modeled by using a finite source to excite models of more complicated GPR antennas (e.g. Lampe and Holliger, 2003, Lampe et al., 2005, and Roberts and Daniels,

1997). In this model the excitation of a single discrete cell is used to represent the GPR antenna.

The source excitation function *Js(t)* used in this model is the second time derivative of the Gaussian function, or Ricker Wavelet,

$$Js(t) = \frac{(t-1/f)}{\sigma^3\sqrt{2\pi}}\left(1-\frac{(t-1/f)^2}{2\sigma^2}\right)e^{-\frac{(t-1/f)^2}{2\sigma^2}}, \quad (13),$$
$$\sigma = \frac{1}{2\pi f}$$

where t is time and *f* is the center frequency of the source. This wavelet is a good approximation of the actual GPR source wavelet of the PulseEkko 100 system used in this dissertation. This is a bandlimited source and only requires that the time steps be small enough to properly sample the highest significant frequency of the wavelet.

The source function is implemented in the ADI-FDTD update equations using the symmetric source procedure of Donderici and Teixeira (2005). In the traditional FDTD source implementation the source $J_s$ is added to the field component, explicitly, after executing the update equation. In the ADI-FDTD scheme, this leads in an asymmetric implementation of the source (Donderici and Teixeira, 2005). In the symmetric source implementation the source $J_s$ is included within the right hand side of the tridiagonal set of the simultaneous equations,

$$\begin{aligned}
&-\alpha 2Ey^{n+1/2}_{(i-1,j+1/2,k)} + \beta 2Ey^{n+1/2}_{(i,j+1/2,k)} - \gamma 2Ey^{n+1/2}_{(i+1,j+1/2,k)} = \\
&p2\cdot Ey^{n}_{(i,j+1/2,k)} + \{Hx^{n}_{(i,j+1/2,k+1/2)} - Hx^{n}_{(i,j+1/2,k-1/2)}\}/\Delta z(k) \\
&-(Hz^{n}_{(i+1/2,j+1/2,k)} - Hz^{n}_{(i-1/2,j+1/2,k)})/\Delta x(i) \qquad (14) \\
&-r2\cdot[\{Ex^{n}_{(i+1/2,j+1,k)} - Ex^{n}_{(i+1/2,j,k)}\}/\Delta y(j)\Delta x(i) \\
&+q2\cdot[\{Ex^{n}_{(i-1/2,j+1,k)} - Ex^{n}_{(i-1/2,j,k)}\}/\Delta y(j)\Delta x(i) + Js^{n+p1}_{(i,j+1/2,k)}
\end{aligned}$$

where the superscript *p1* for the source *Js* represents the time index of the source. Considering the evaluation time of a centered difference scheme, the time index *p1* for both substeps of the alternating implicit scheme is ½ to preserve the symmetry in the

field values. Therefore the same source value is used in both substeps.

## MODEL VALIDATION

To validate the accuracy of the ADI-FDTD code, I compared the analytical solution of an infinitesimal dipole in a vacuum with simulation results. Since many geophysical applications probe in the regions that involve both the far field and the near field, I used the full analytic solution of the Hertzian dipole in a whole space (see Demarest, 1998). The error between the analytic solution and the ADI-FDTD solution for an infinitesimal dipole in a vacuum at one wavelength from the source as a function of angle in the x-z plane is 1.68%+-1.61% (Figure A-2).

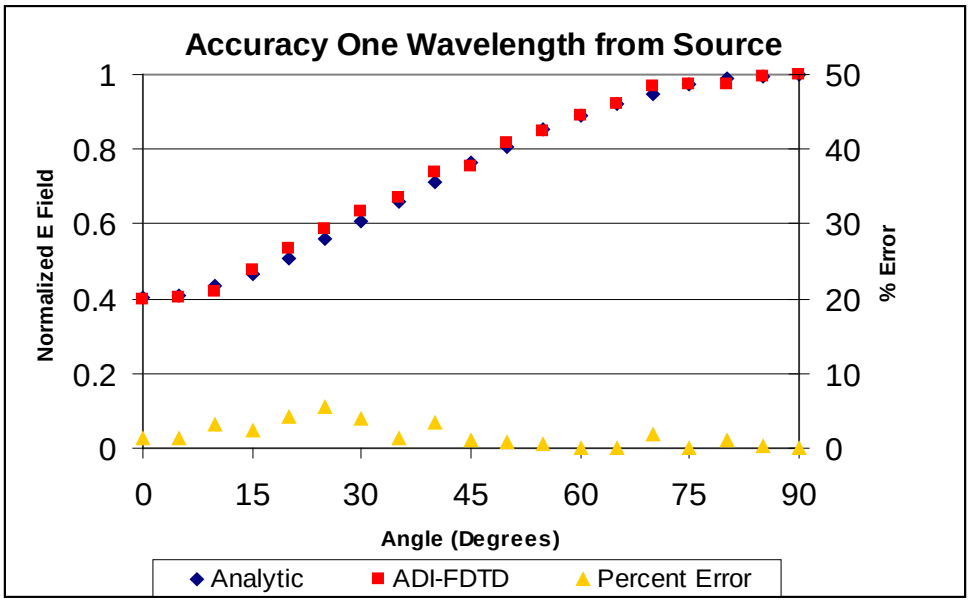


Figure A-2. A comparison of the analytic solution and the ADI-FDTD for an infinitesimal dipole in a vacuum at one wavelength from the source as a function of angle in the x-z plane. The simulation was run at twice the Courant stability limit with a grid spacing of 0.035 m.

## EXAMPLE SIMULATIONS

To demonstrate the ADI-FDTD model, several models were constructed for visualizing a snapshot of the electromagnetic waves as they propagate away from a GPR antenna situated at the interface between the air and ground. In the first example (Figure A-1) the simple case of an pulse-excited GPR antenna over a homogenous half space is demonstrated. One can see the main body wave propagating through the ground, the air wave propagating through free space and the refracted wave.

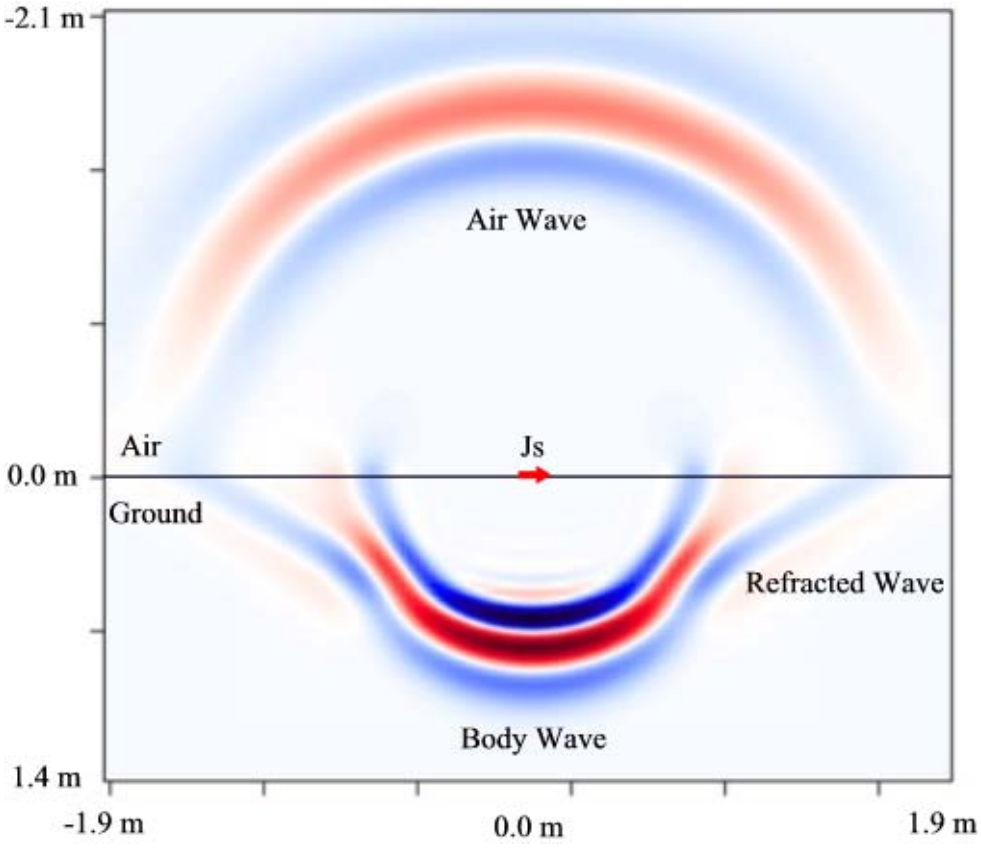


Figure A-3. This snapshot is of the Ex component in the x-z plane at 9 ns from a Ricker source (Js) with a 300 MHz center frequency. The ground space has relative dielectric constant of 4 and a conductivity of 0.00001 S/m. The simulation was run at twice the Courant stability limit with a even grid mesh of 0.035 m.

In the second example (Figure A-4) the previous model is changed to include a small air filled cavity within the ground. In this simulation one can see the reflected wave propagating back towards the GPR antenna, as well as the refraction of the body wave from passing through the cavity.

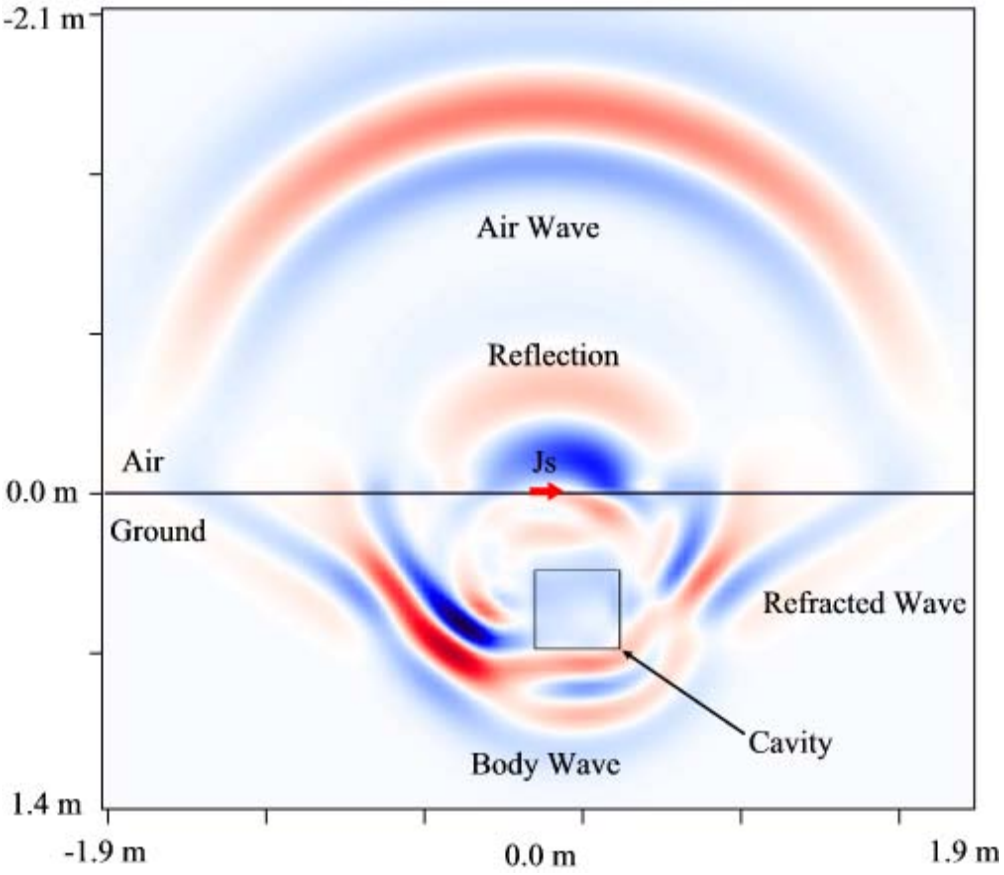


Figure A-4. This snapshot is of the Ex component in the x-z plane at 9 ns from a Ricker source (Js) with a 300 MHz center frequency. The variables are the same as in Figure A-3 except a 0.3 m cubic cavity has been introduced at a depth of 0.3 m.

The final example (Figure A-5) is a 3D vector visualization of the electromagnetic field for the previous model. While the previous scalar representations of the electric field are convenient to visualize, the electromagnetic field is actually vector in nature. This

vector representation provides some insight into the complexity of the GPR signal that is often ignored when acquiring single component GPR data.

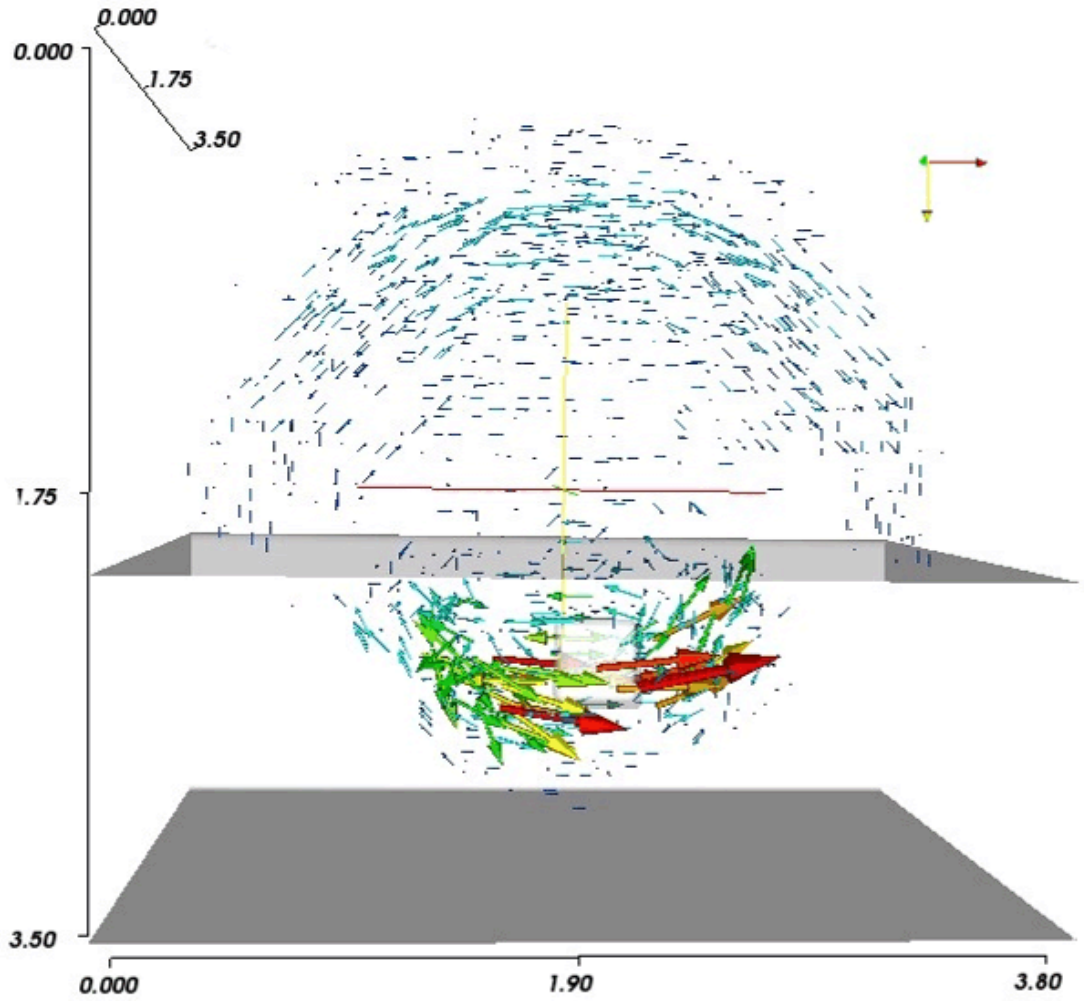


Figure A-5. This is vector plot of the electric field intensity for the same simulation as Figure A-4. Larger arrows indicate greater magnitude.

## CONCLUSIONS

The ADI-FDTD technique provides a tool for solving complicated subsurface propagation and scattering problems in much less computation time than traditional

FDTD. This makes it an ideal tool for geophysical applications where small scale heterogeneities strongly influence the response. The ADI-FDTD algorithm presented here is designed primarily for speed, with the intention of using it in inverse modeling where large numbers of successive forward models must be run.

## REFERENCES

Berenger, J-P., 1994, A perfectly matched layer for the absorption of electromagnetic waves: Journal of Computational Physics, **144**, 185-200.

Berenger, J-P., 1996, Three-dimensional perfectly matched layer for the absorption of electromagnetic waves: Journal of Computation Physics, **127**, 363-379.

Chen, C. C-P, T-W. Lee, N. Murugesan, S.C., and Hagness, 2000, Generalized FDTD-ADI: An unconditionally stable full-wave Maxwell's equations solver of VLSI Interconnect Modeling: IEEE, 156-163.

Christ, A., S. Benkler, J. Frohlich, and N. Kuster, 2006, Analysis of the accuracy of the numerical reflection coefficient of the finite-difference time-domain method at planar material interfaces: IEEE Trans. on Electromagnetic Compatibility, **48**, no. 2, 264-272.

Demarest, K.R., 1998, Engineering electromagnetics: Prentice Hall, Upper Saddle River, New Jersey.

Dey, S., and R. Mittra, 1999, A conformal finite-difference time-domain techniques for modeling cylindrical dielectric resonators: IEEE Trans. on Microwave Theory and Techniques, **47**, no 9, 1737-1739.

Donderici, B. and F.L. Teixeira, 2005, Symmetric source implementation for the ADI-FDTD method: IEEE Trans on Antennas and Propagation, **53**, no.4, p1562-1565.

Holland, R., 1993, Pitfalls of staircase meshing: IEEE Trans on Electromagnetic Compatibility, **35**, 434-439.

Lampe, B., and K. Holliger, 2005, Resistively loaded antennas for ground-penetrating radar: A modeling approach: Geophysics, **70**, K23-K32.

Lampe, B., K. Holliger, and A.G. Green, 2003, A finite-difference time-domain simulation tool for ground-penetrating radar antennas: Geophysics, **68**, 971-987.

Liu, G., and S.D. Gedney, 2000, Perfectly matched layer media for an unconditionally stable three-dimensional ADI-FDTD method: IEEE Microwave and Guided Wave Letters, **10**, 261-263.

Namiki, T., 1999, A new FDTD algorithm based on alternating-direction implicit method: IEEE Trans on Microwave Theory and Techniques, **47**, 2003-2007.

Namiki, T., 2000, 3-D ADI-FDTD Method – Unconditionally stable time-domain algorithm for solving full vector Maxwell's equations: IEEE Trans on Microwave Theory and Techniques, **48**.

Roberts, R.L., and J.J. Daniels, 1997, Modeling near-field GPR in three dimensions using the FDTD method: Geophysics, **62**, 1114-1126.

Staker, S.W., C.L. Holloway, A.U. Bhobe, and M. Piket-May, 2003, Alternating-direction implicit (ADI) formulation of the finite-difference time-domain method: algorithm and material dispersion implementation: IEEE Trans on Electromagnetic Compatibility, **45**, 156-166.

Wang, T., and A-C. Tripp, 1996, FDTD simulation of EM wave propagation in 3-D media: Geophysics, **61**, 110-120.

Yeh, C., 1993, Boundary conditions in electromagnetic: Physical Review E, **48**, 1426-1427.

Zheng, F., Z. Chen, and J. Zhang, 1999, A finite-difference time-domain method without the Courant stability conditions: IEEE Microwave and Guide Wave Letters, **9**, 441-443.

# VITA

Douglas Spencer Sassen received his B.S. degree in Geology from The University of Texas at Austin in 2000. He entered the environmental and engineering geology program at Texas A&M University in January 2001 and received his Master of Science degree in December 2003. His research interests include GPR acquisition, data processing and interpretation, time series analysis, numerical modeling and neural networks for geophysical application.

Douglas Sassen may be reached at Lawrence Berkeley National Laboratory, 1 Cyclotron Road Mail Stop 90-1116, Berkeley, CA 94720, and email at dssassen@lbl.gov. He is currently employed at Lawrence Berkeley National Laboratory as a post-doctoral fellow.